

**COMPUTATIONAL STUDY OF HYDROGEN ADSORPTION ON
LANTHANUM FERRITE (LaFeO₃) (0 1 0) SURFACE**

**A thesis submitted to the Department of Chemistry, College of Science, Kwame
Nkrumah University of Science and Technology, Kumasi**

in partial fulfilment of the requirements for the award of the degree

MASTER OF PHILOSOPHY

in Physical Chemistry

By:

Isaac Wiafe Boateng, BSc. (Hons)

April, 2016

DEDICATION

This piece of work is dedicated to my parents, friends and well-wishers.

ACKNOWLEDGEMENT

First of all, I would like to express my profound gratitude and thanks to the Sovereign Lord for His Grace, Mercies, Goodness, Compassion, Guidance, Protection and Strength He has shown me through this period of study and research.

My sincere thanks go to my internal supervisors, Professor Evans Adei and Dr. Richard Tia for their guidance, encouragements, direction, assistance, mentorship, training, and fatherly love in my academic and research pursuits. Thanks to Professor Nora De Leeuw and Professor Charles Richard Arthur Catlow, who are my external supervisors. Much appreciation also to Dr. Nelson Yaw Dzade, now at the University of Utrecht and Mr. Alexander O'Malley of the University College London (UCL) - London, for their enormous contributions.

Thanks to other members of the lab, Mr. Albert Aniagyei, Mr. Fred Joseph Komla Adzabe, Mr. Elliot Sarpong Menkah, Mr. Joel Baffour Awuah, Miss. Caroline Rosemyya Kwawu for their encouragement, constructive criticisms and support especially during group presentations.

I am very much grateful to the Royal Society, UK for financial assistance under the Leverhulme - Royal Society Africa Award which enabled a collaborative research between our University and the University College London (UCL) - London, UK.

My greatest appreciation goes to my family, friends and well-wishers for their constant support, prayers and love during the entire duration of the programme. I am forever grateful and may the Good Lord bless them according to His riches in glory.

ABSTRACT

The electrochemical hydrogen storage mechanism of LaFeO_3 , a functional material widely studied as potential negative electrode material in nickel-metal hydride batteries, still remains unsettled, and requires more simulation studies to provide molecular-level insight into how the hydrogen adsorbs on the LaFeO_3 perovskite oxide surface. Spin-polarized density functional theory calculations with the PBE exchange-correlation functional within the GGA and GGA+U using the plane-wave pseudopotential PWscf code in the Quantum-ESPRESSO package have been used to investigate the bulk structures and electronic properties, as well as the adsorption of H_2 on lanthanum ferrite (LaFeO_3). Adsorption energy calculations predict that for the use of LaFeO_3 as anodic material in Ni-MH batteries, the most preferred adsorption site for H_2 is the *Fe-O bridge* site where the O coordinates to another Fe atom and a La atom, and the Fe in the bridge coordinates to two other O atoms and two La atoms. When one molecule of the H_2 is adsorbed at H-H molecular, dihydrogen and dihydride bond distances on this *Fe-O bridge* site of the LaFeO_3 (0 1 0) surface, $-\text{Fe}(\mu\text{OH})\text{La}$ and $-\text{FeH}$ are formed with adsorption energy in the range -0.455 to -0.456 eV. Similar adsorption sites do not necessarily give the same products on addition of H_2 . Even though some *Fe-O bridge* sites give $-\text{Fe}(\mu\text{OH})\text{La}$ and $-\text{FeH}$ others give LaOH and FeH . At the O top end-on sites, while some give LaOH and FeH , others give H_2O or FeOH depending on the H-H distances. All the O-top sites with the exception of that which coordinates to only La at the terminal position form H_2O in at least one of the forms of H_2 in an end-on attachment to O atom, leaving the surface to create an oxygen vacancy. Nonetheless, it is only at the O site which connects just two La atoms and in the dihydride H-H bond distance end-on configuration that involves

dislodgement of H₂O from the surface and vacancy hopping oxygen transport. Molecular hydrogen on the LaFeO₃ (0 1 0) surface can only form H₂O at the O top end-on site where the O coordinates to two Fe atoms and a La atom. Fe and La dihydrogen and dihydride bonds do not form on LaFeO₃ (0 1 0) surface and also no hydrogen is adsorbed on the La atom. O atom facilitates the addition of hydrogen on the surface. Adsorbing another H₂ molecule on LaFeO₃ (0 1 0)/H₂ system for a more realistic adsorption reveals that the adsorption at *Fe-O bridge** site where the second H₂ is at a dihydride bond distance leads to the formation of H₂O through an unstable and unfavourable adsorption process. Fe changes oxidation state from +3 to +2 when one and two molecules of H₂ are adsorbed. These results improve our understanding of the electrochemical hydrogen storage mechanism of LaFeO₃.

TABLE OF CONTENTS

DECLARATION	i
DEDICATION.....	ii
ACKNOWLEDGEMENT.....	iii
ABSTRACT	iv
TABLE OF CONTENTS	vi
LIST OF FIGURES	ix
LIST OF TABLES	x
LIST OF ABBREVIATIONS.....	xi
CHAPTER ONE	1
1. INTRODUCTION.....	1
1.1 General Introduction	1
1.2 Problem Statement	6
1.3 Objectives of Research.....	7
1.3.1 Main Objective.....	7
1.3.2 Specific Objectives.....	7
1.4 Justification.....	8
CHAPTER TWO	9
2. LITERATURE REVIEW	9
2.1 Hydrogen as an Energy Carrier	9
2.2 The Hydrogen Economy	10
2.3 Hydrogen Properties	11
2.4 General Requirements for Hydrogen Storage Systems.....	13
2.5 Nickel Metal Hydride (Ni-MH) Battery.....	17
2.5.1 Principles of Ni-MH batteries.....	19
2.6 Ideal Perovskite Structure	21
2.6.1 Distorted Perovskite Structure - Tolerance Factor.....	24
2.7 Lanthanum Ferrite (LaFeO ₃)	25
2.7.1 Structure of LaFeO ₃	26
2.7.2 Crystal Data of LaFeO ₃	28

2.8 Relaxation and Reconstruction of Surfaces.....	28
2.9 Hydrogen Adsorption on Surfaces.....	28
CHAPTER THREE	30
3. COMPUTATIONAL METHODOLOGY.....	30
3.1 Computational Procedures of the Quantum-ESPRESSO Code	30
3.2 The Plane-wave self-consistent field method.....	30
3.3 Important Input Parameters	31
3.4 Input File for a Simple PWscf Calculation	32
3.5 Computational Details.....	34
CHAPTER FOUR	37
4. RESULTS AND DISCUSSION.....	37
4.1 Input Parameters for Lanthanum Ferrite (LaFeO ₃).....	37
4.1.1 Convergence Tests for Kinetic Energy Cut-off, E _{cut} and K-points	37
4.1.2 Effective Hubbard U, U _{eff} for LaFeO ₃	38
4.2 Bulk Structures (Properties) and Some Electronic Properties of LaFeO ₃	40
4.2.1 Bulk Properties of LaFeO ₃	40
4.2.2 Electronic Properties of Bulk LaFeO ₃	44
4.3 Adsorption of Hydrogen on (0 1 0) Surface of LaFeO ₃	46
4.3.1 Bond Length of Molecular Hydrogen	47
4.3.2 Why Optimal Hubbard U term was not included in Surface Calculations.....	48
4.3.3 Choice of the (0 1 0) Miller Index.....	49
4.3.4 Clean LaFeO ₃ (0 1 0) Surface	50
4.3.5 Relaxation and Reconstruction of Clean LaFeO ₃ (0 1 0) Surface	52
4.3.6 The Adsorption Mechanism of one H ₂ on LaFeO ₃ (0 1 0) Surface	54
4.3.7 Analysis of the Projected and Total Density of States Plots for H ₂ adsorption on LaFeO ₃ (0 1 0) Surface	69
4.3.8 Analysis of the Löwdin Charge Population on LaFeO ₃ (0 1 0)/H ₂ System: <i>Fe3-</i> <i>O19 bridge</i> Site	73
4.3.9 Investigations into Lanthanum Hydride formation on LaFeO ₃ (0 1 0) Surface ..	76
4.3.10 The Adsorption Mechanism of another H ₂ Molecule on LaFeO ₃ (0 1 0)/H ₂	77

4.3.11 The Potential of H ₂ O as a Good Leaving Group on LaFeO ₃ (0 1 0)/2H ₂ at <i>Fe-O bridge*</i> Site	83
4.3.12 Analysis of PDOS and TDOS Plots for two H ₂ adsorption on LaFeO ₃ (0 1 0) Surface	86
4.3.13 Analysis of the Löwdin Charge Population on LaFeO ₃ (0 1 0)/2H ₂ System: <i>Fe-top end-on</i> Adsorption Site	92
CHAPTER FIVE	94
5. SUMMARY AND CONCLUSIONS.....	94
REFERENCES	96
APPENDIX	100

LIST OF FIGURES

Figure 1.1 World fuel energy consumption	2
Figure 2.1 Potential energy curve for hydrogen which is chemically and physically adsorbed on the surface of an adsorbent versus how far it is from the surface.....	15
Figure 2.2 Schematic diagram of the electrochemical reaction process of a Ni-MH battery .	21
Figure 2.3 Schematic representation of the ideal perovskite structure .	22
Figure 2.4 The crystal structure of LaFeO ₃	27
Figure 4.1 Convergence test for plane wave cut off energy, E _{cut} and Monkhorst-Pack k-points grid.....	38
Figure 4.2 Electronic band gap, E _g for LaFeO ₃ plotted against different U _{eff} values.....	40
Figure 4.3 Converged/ Optimized structures of LaFeO ₃ without and with Hubbard U parameter.....	42
Figure 4.4 Total density of states (DOS) and projected density of states (PDOS) of orthorhombic LaFeO ₃ (a) Without Hubbard U and (b) With Hubbard U = 4.64 eV	46
Figure 4.5 Molecular hydrogen in a 10 Å x 10 Å x 10 Å box.....	48
Figure 4.6 Side view of the optimized five-layer slab model of the ideal LaFeO ₃ (0 1 0) surface with La-O-Fe termination	51
Figure 4.7 Side views of the initial and optimized structures of all the different kind of products that form at selected favourable adsorption sites	59
Figure 4.8 Side view of initial and optimized structures at <i>Fe3-O19 bridge</i> site.....	69
Figure 4.9 PDOS and TDOS on <i>Fe3-O19 bridge</i> site at molecular hydrogen bond distance (a) before adsorption and (b) after adsorption.....	73
Figure 4.10 Geometries towards investigation into -LaH formation on LaFeO ₃ (0 1 0) surface	77
Figure 4.11 Side views of the initial and optimized structures of the possible adsorption sites on an already adsorbed <i>Fe-O bridge</i> site	82
Figure 4.12 Geometries towards the potential of H ₂ O as a good leaving group in LaFeO ₃ (0 1 0)/2H ₂ at <i>Fe-O bridge*</i> site.....	85
Figure 4.13 Side view of initial and optimized structures at <i>Fe-top end-on</i> site.....	86
Figure 4.14 PDOS and TDOS for two H ₂ molecule adsorption (a) before adsorption and (b) after adsorption on <i>Fe-top end-on</i> site.....	92

LIST OF TABLES

Table 2.1 Properties of hydrogen.....	11
Table 2.2 Safety properties of different fuels in air	12
Table 2.3 Ionic radii (Å) of some elements common in the perovskite structures	24
Table 4.1 Electronic state of LaFeO ₃ bulk	40
Table 4.2 Calculated and experimental lattice constants (a, b, c), axial and equatorial Fe-O bond lengths (r_z and r_{xy} , respectively), axial and equatorial Fe-O-Fe bond angles (α_z and α_{xy} , respectively), eigenvalue gap (E_g), Fe magnetic moment (μ_{Fe}) and cell volume for orthorhombic LaFeO ₃	43
Table 4.3 Surface energies of the various low miller indices.....	50
Table 4.4 Atoms (and their IDs) of the ideal LaFeO ₃ (0 1 0) surface within the QE input file showing the layers they occupy and the layer's termination.....	52
Table 4.5 Surface relaxation of the unreconstructed clean surface of LaFeO ₃	53
Table 4.6 Calculated E_{ads} and product(s) at the favourable adsorption sites.....	61
Table 4.7 Calculated E_{ads} and product(s) at the other adsorption sites	62
Table 4.8 Calculated structural parameters at the favourable adsorption sites when hydrogen atoms are at a molecular distance apart.....	63
Table 4.9 Calculated structural parameters at the favourable adsorption sites when hydrogen atoms are at a dihydrogen distance apart.....	65
Table 4.10 Calculated structural parameters at the favourable adsorption sites when hydrogen atoms are at a dihydride distance apart	67
Table 4.11 Löwdin Charge Population results for LaFeO ₃ (0 1 0) surface before and after H ₂ adsorption: <i>Fe3-O19 bridge</i> Site.....	75
Table 4.12 Calculated structural parameters and energies of the possible adsorption sites on an already adsorbed <i>Fe-O bridge</i> site (most stable adsorption configuration when one H ₂ molecule was adsorbed).....	83
Table 4.13 Löwdin charge population results for LaFeO ₃ (0 1 0) surface before and after two H ₂ molecule adsorption	93

LIST OF ABBREVIATIONS

➤ E_{ads}	Adsorption Energy
➤ Cd-Ni	Cadmium-Nickel
➤ P_c	Critical Pressure
➤ T_c	Critical Temperature
➤ DFT	Density Functional Theory
➤ DOS	Density of States
➤ DOE	Department of Energy
➤ E_{dist}	Distortion Energy
➤ U_{eff}	Effective Hubbard U parameter
➤ EVs	Electric Vehicles
➤ E_g	Electronic Band Gap
➤ XC	Exchange – Correlation energy functional
➤ E_F	Fermi Energy Level
➤ GdFeO_3	Gadolinium Orthoferrite
➤ GPL	General Public License
➤ GGA	Generalized Gradient Approximation
➤ GNU	GNU's Not Unix
➤ HEVs	Hybrid Electric Vehicles
➤ IPCC	Intergovernmental Panel of Climate Change
➤ E_{cut}	Kinetic Energy Cutoff
➤ V_{KS}	Kohn-Sham Potential
➤ LaFeO_3	Lanthanum Orthoferrite
➤ MH	Metal Hydride
➤ M	Metals/Alloys/Intermetallics
➤ METADISE Dislocations,	Minimum Energy Technique Applied to

Interfaces and Surfaces Energies

- Ni-MH Nickel-Metal Hydride
- PBE Perdew – Burke – Ernzerhof exchange-correlation
- PWscf Plane-Wave Self-Consistent Field
- PHEVs Plug-in Hybrid Electric Vehicles
- PDOS Projected Density of States
- QE Quantum-ESPRESSO
- TPD Temperature Programmed Desorption
- UHF Unrestricted Hartree – Fock
- XCrySDen (X-Window) Crystalline Structures and Densities

CHAPTER ONE

1. INTRODUCTION

1.1 General Introduction

A direct relationship exists between the world's populace and economic growth, and energy demand. As the world's population and economic growth increases, energy demand also increases. A wide range of activities which include the production of consumer goods, transportation and house heating relates to the energy consumption. With the growth in global population densities, worldwide energy reserves in the form of fossil fuels are diminishing. Statistics on the world's energy consumption in 2011 (Figure 1.1) indicate that 86.5 % is related to fossil fuel's natural gas, coal and oil. The well-known recoverable national reserves of natural gas, coal and oil is estimated to last for only few years following the recent consumption and production techniques of energy. This appalling short term estimate compels humankind to come out with alternate sources and carriers of energy that are renewable, and can at the same time be extensively applied to withstand improved standards of living. Aside the limitations and demand of fossil fuel, environmental pollution is another most important problem that relates our energy supply. The Intergovernmental Panel on Climate Change (IPCC), among several organizations in the United Nations has now shown that the effects of global warming are mostly caused by the anthropogenic CO₂ emissions to the atmosphere. This global warming has the potential to cause polar ice to melt, sea level to rise, permafrost to defrost, and surge extreme weather phenomena such as heavy rains, hurricanes and tornadoes.

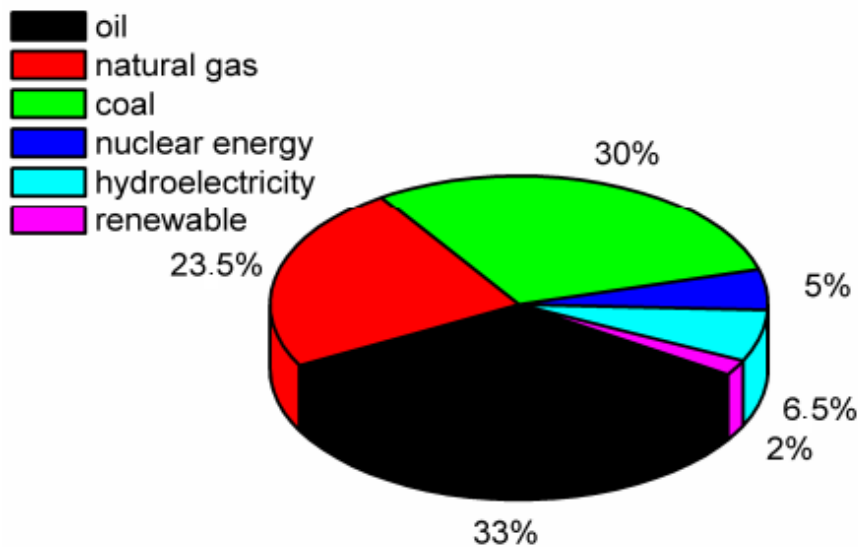


Figure 1.1 World fuel energy consumption (BP statistical review of world energy, 2012)

Alternate energy development to fossil fuels that existing transportation greatly rely on is vital as a result of the calamitous climate change and increased future energy security concerns. A number of alternate energy sources exist. They include geothermal, nuclear, solar, wind, and hydrogen. However, it has been recognised in recent years that hydrogen is a promising future energy resource, hence the need for a hydrogen-based economy.

Hydrogen (H₂) is a perfect clean energy vector with both strategic and environmental benefits since it is both pollution- and carbon- free, and burns to produce water. The combustion of fossil fuels on the other hand generates CO₂ and a variety of pollutants. Hydrogen (H₂) constitutes normal matter in mass by 75 %, making it one of the most abundant elements in the universe (Xia et al., 2013). In comparison to the extensively used gasoline and coal, hydrogen has much energy content per unit mass. Governments and research communities all over the world in the past decade have increasingly recommended the potential of hydrogen economy (Armaroli and Balzani, 2011; Eberle and von Helmholt, 2010; Momirlan and Veziroglu, 2005) where the use of hydrogen is in the future widely expected to replace fossil

fuels. Nonetheless, for hydrogen economy to be realised, important technical hurdles like its generation, storage and applicability in fuel cells has to be tackled. Among these, achieving efficient, economical and safe on-board hydrogen storage is a massive task.

Usually, hydrogen is stored in compressed gas cylinders or as liquid hydrogen via liquefaction, or solid state storage in chemical hydrides. It is also adsorbed on porous materials such as carbons, zeolites, porous polymers, metal organic framework materials, or covalent organic framework materials. There are however limitations associated with each storage method. Liquefaction presents high energy cost; compressed gases have safety concerns because of its operation at high pressures; chemisorption of metal hydrides and chemical hydrides have slow kinetics, high thermodynamics and poor reversibilities; and physisorption of hydrogen in porous materials have reasonable hydrogen uptake only at cryogenic temperature (David, 2011). The efficient hydrogen storage in proper media that have high capacities therefore remains an important technological bottleneck for everyday use.

For portable electrical devices and transport vehicles such as electric vehicles (EVs), hybrid electric vehicles (HEVs), and plug-in hybrid electric vehicles (PHEVs), rechargeable batteries are regarded as one of the simplest, efficient, and reliable systems (Palacin, 2009), meeting the criteria set by the U. S. Department of Energy (2011) for commercial use of hydrogen storage systems. To date, most research works emphasize on developing advanced Li-ion and Ni-MH batteries as high energy density and good environment compatibility power sources. Generally, Ni-MH batteries are regarded as the favourite choice intended for practical applications due to their properties such as long stable periods, fast charge and discharge capabilities, high capacities, and environment-friendly characteristics (Cuscuetta et al., 2010). They also have a number of advantages such as harmlessness, reasonable price,

interchangeability with Cd-Ni batteries, and high charge/recharge rate over other small-sized rechargeable batteries such as the Li-ion.

Electrode materials that are the media for storing energy in the batteries are vital to improving their performance. To develop durable and highly efficient Ni-MH batteries, hydrogen storage alloys which are mostly used as the negative electrode material have mainly concentrated on their properties of reversible hydrogen storage, which have improved electrochemical properties. At present, the rare earth AB₅-type and Ti- and Zr-based AB₂-type alloys have been developed as two types of commercial electrode materials for Ni-MH batteries. Whereas AB₅-type is not fully satisfactory with the challenge for vehicles application due to their high cost and restricted capacity (theoretical ~ 372 mAh/g), there is poor activation of AB₂-type alloys. Other rare earth-Mg-Ni-based superlattice alloys, Mg-based amorphous and nanocrystalline alloys, and Ti-V-based multicomponent multiphase alloys have been more or less promoted to improve the performance of Ni-MH batteries (Bliznakov et al., 2005; Kadir et al., 2000). Nonetheless, their high cost and limited cycle life caused by alloy corroding in the alkali solution electrolyte still blocks their better performance in commercial application (Liu et al., 2005).

The single CaCu₅-type hexagonal structure of the AB₅-type alloys which have wide application in devices such as portable electric devices, hand tools and vehicles, makes it exhibit its limited capacity, making it difficult for it to be increased dramatically in order to meet the increasing requirements set by the U. S Department of Energy. Therefore, it is indispensable to reduce the cost and increase the capacity of Ni-MH batteries by developing novel negative electrode materials.

Perovskite ABO₃ has attracted a lot of attention as potential negative electrode materials (Zhang et al., 2007; Samara, 2003) in recent years. They are mixed-metal oxides that are

attracting much scientific and application interest because of their adaptability, thermal stability, and low price, which often depend on their surface and bulk features. These ABO₃ perovskite oxides, unlike traditional hydrogen storage alloys were usually concentrated on their ion-exchange ability for electrolyte application, until the doped perovskite oxide SrCe_{0.95}Yb_{0.05}O_{3-δ} was reported as novel electrode material for Ni-MH batteries (Esaka et al., 2004). In recent works by Deng et al., (2010) and Gang et al., (2009), the rare-earth transition metal oxide, LaFeO₃ excitingly exhibited much considerable electrochemistry capacity from 51.8 to 443.2 mAh/g at temperature range of 25 to 80 °C, and sustainable stability without any crystal structure change in twenty cycles. Subsequent studies revealed that LaFeO₃ could easily absorb the proton primarily dissociated from gas water (Wang et al., 2013). In comparison to hydrogen storage alloys, there is no need to activate this type of electrode material during discharging. Electrochemistry capacity rose dramatically as working temperatures went up, demonstrating an outstanding cycle life, which was indicative that perovskite oxide LaFeO₃ has a better corrosion resistance at elevated temperatures than traditional hydrogen storage alloys (Wang et al., 2013).

In view of the high capacity and abundance of La, LaFeO₃ has been widely studied as potential negative electrode materials for Ni-MH batteries. Chen et al. (2014) have investigated from first principles the hydrogen adsorption on LaFeO₃ (1 1 0) surface in the framework of non-spin-polarized density functional theory (DFT) with the PBE exchange-correlation functional within the GGA based on the ultrasoft plane-wave pseudopotential. From the adsorption sites, adsorption energies, and electronic structures, they found that one H atom can be adsorbed on O atom to form -OH with the O atom, which is the most stable structure. One H atom can be adsorbed on one Fe atom making the Fe change valence state from +3 to +2. Two H atoms can form H₂O molecule with O atom, which suggested that it was possible to form oxygen vacancy on the surface. However, the electrochemical hydrogen

storage mechanism of the LaFeO_3 still remains unsettled, and thus requires more investigation to know how the H atoms combine with the perovskite oxide.

1.2 Problem Statement

The alarming short term forecast of the known easily recoverable national reserves of oil, natural gas, and coal is forcing mankind to come out with alternate renewable energy sources and carriers that can commercially be applied to sustain improved living standards. Apart from the fossil fuel limitations and demand, the second important issue related to our energy supply is environmental pollution. Hydrogen, an alternative energy carrier has been recognised in recent years as a promising future energy resource, hence the need for a hydrogen based economy.

Hydrogen has a very high energy content by weight (about 3 times gasoline) but has a very low energy content by volume (liquid hydrogen is about 4 times less than gasoline). This makes hydrogen a challenge to store, particularly within the size and weight constraints of a vehicle. The ability to achieve efficient, economical and safe on-board hydrogen storage is the main issue that has to be addressed for the successful implementation of fuel cell technology in the transport sector, and that is a major materials science challenge.

None of the storage methods presently under consideration completely satisfy all the criteria for the amount of hydrogen that can be supplied from a given weight or volume of tank for transport purposes (Thomas, 2007). Hence, the efficient hydrogen storage in a proper media that has high capacities still remains as a key technological bottleneck for practical applications.

Electrode materials that are the media for storing energy in batteries are key to improving their performance. To develop durable and highly efficient Ni-MH batteries, research on

AB₅-type hydrogen storage alloy which has wide application in devices such as portable electric devices, hand tools and vehicles, have mainly concentrated on their properties of reversible hydrogen storage as a means to improved electrochemical properties. However, they are not fully satisfactory with the challenge for vehicular application due to their high cost and restricted capacity (theoretical ~ 372 mAh/g). It is therefore indispensable to reduce the cost and increase the capacity of Ni-MH batteries by developing novel negative electrode materials.

The rare-earth transition metal oxide, LaFeO₃ has been widely studied as potential negative electrode material for Ni-MH batteries due to their safe and efficient hydrogen adsorption requirement for future fuel cell vehicles. However, their electrochemical hydrogen storage mechanism still remains unsettled, and thus require more simulation studies to know how the hydrogen adsorbs on the LaFeO₃ perovskite oxide.

1.3 Objectives of Research

1.3.1 Main Objective

Investigate hydrogen adsorption on (0 1 0) surface of LaFeO₃

1.3.2 Specific Objectives

- (i) Investigate bulk structures and electronic properties of LaFeO₃ which is one of the suitable functional materials for storage devices
- (ii) Investigate adsorption mechanism of one and two molecules of hydrogen on LaFeO₃ (0 1 0) surface
- (iii) Investigate the potential of H₂O as a good leaving group on LaFeO₃ (0 1 0) surface when two H₂ molecules are adsorbed
- (iv) Analyse the net charge transfer between hydrogen and LaFeO₃ (0 1 0) surface after adsorption

- (v) Analyse changes of electronic state before and after adsorption of hydrogen on LaFeO_3 (0 1 0) surface

1.4 Justification

Adsorption studies of hydrogen on LaFeO_3 (0 1 0) surface will help to clarify the electrochemical hydrogen storage mechanism of the perovskite in nickel-metal hydride battery applications. Understanding the mechanism will enable control of the pathway of the reaction leading to desired products. By investigating into the LaFeO_3 slab character and hydrogen adsorption on the slab with the aim of explaining the adsorption mechanism of reaction, theoretical guidance for correlative experiment will be provided.

CHAPTER TWO

2. LITERATURE REVIEW

2.1 Hydrogen as an Energy Carrier

Hydrogen is considered the main energy carrier for the future because of important merits that relates to its essential properties. It is the lightest and highly abundant element on the surface of the earth, and is a constituent element in most compounds (for example; hydrocarbons, water and biomass). It is nontoxic, odourless, tasteless, and colourless under standard conditions. Molecular hydrogen is easily formed from numerous sources. At present, steam reforming of methane or natural gas is the most popular means of producing hydrogen. The method, however generates undesirable CO₂. Another way of producing the hydrogen is from dissociation of water in the course of electrolysis. Hydrogen production from this sustainable energy source is a “clean” way and the process is completely reversible. Currently, about fifty percent of the total amount of hydrogen produced is used for ammonia synthesis which is subsequently used mainly for the manufacture of fertilizers, whilst a greater part is used in the oil refineries. Countless intermediate chemical products are also synthesized using hydrogen. The light mass of hydrogen gives it a very large energy density per mass (~ 39 kWh kg⁻¹) which is three-fold higher than gasoline. A car with combustion engine can be driven through a 400 km distance using about 8 kg of hydrogen to occupy a volume of around 100 cubic meters at room temperature and atmospheric pressure (Schlapbach and Zuttel, 2001). Thus, for practical and reasonable applications, the low hydrogen density which is in the gas phase has to be increased by temperature decrease and compression, or alternate high storage methods ought to be considered.

Hydrogen has to contend with other fuels in its usage as an energy carrier. It could outperform electric batteries that are somewhat heavy and bulky in electric vehicles

(Zumerchik, 2001). Using hydrogen and fuel cells to run an electric vehicle instead of batteries have a number of advantages according to General Motors. For instance, there would be cost reduction as well as attaining higher energy densities (von Helmholt and Eberle, 2007).

2.2 The Hydrogen Economy

The first research on hydrogen was done by Henry Cavendish and Antoine Lavoisier in the mid-18th century. Cavendish discovered it in 1766 and Lavoisier gave it its name in 1783 (Weber, 1991). In spite of the recent focus on hydrogen as an energy carrier, the whole idea is not first-hand. In actual fact, coal gas and syngas found extensive use for illumination, heating, and engines since around 1800, and for more than 150 years, until being replaced by natural gas (Weber, 1991; Zumerchik, 2001). Syngas is however still in use in the present day especially in places where natural gas is costly or unavailable (Zumerchik, 2001). Jules Verne, the science-fiction and novelist had in 1874 made-up an energy system in his “The Mysterious Island” novel based on electrolyzed hydrogen.

Not until 1972, “hydrogen economy” as a terminology was not introduced (Bockris, 2002). Great public attention was paid to the concept of hydrogen economy as a result of the oil crises in the 1970s, and the nuclear disasters of Chernobyl and Fukushima in 1986 and 2011 respectively. Producing hydrogen from sources that are renewable, transporting them over hefty distances, storing them in large quantities and using them to generate heat, electricity and propulsion for consumers is the whole idea of the hydrogen economy (Bockris, 2002). Production of hydrogen could be done locally as well as centrally. They can also be produced from a number of sources including wave, wind, solar, water and biomass. To distribute hydrogen, it could be made to coexist with conventional electricity network so as to provide energy to the industry, households, and vehicles. A pipeline network which is similar to what

the natural gas system currently employs could be used to distribute the hydrogen provided materials are found to be well-matched (Zumerchik, 2001).

2.3 Hydrogen Properties

Among all elements, hydrogen is the lightest. In the universe, it is the most abundant (Zumerchik, 2001; Patnaik, 2002). However, on earth it is ranked as the 15th element, and has a very low concentration of about 0.5 ppm in the atmosphere (Patnaik, 2002; King, 1994). Nonetheless, a lot of chemical compounds are formed from it with water as the most abundant (Patnaik, 2002). It forms the dihydrogen diatomic molecule in its gaseous state with an H-H bond length of 0.8 – 1.0 Å for true H₂ complex and 1.0 – 1.3 Å for an elongated H₂ complex. When the H-H bond distance is 1.3 – 1.6 Å, it is a compressed dihydride whilst when it is greater than 1.6 Å, it is a dihydride. It is essentially hydrogen atoms when it is at the dihydride H-H bond distance. Hydrogen gas is nontoxic, odourless, and transparent.

Table 2.1 below presents some of its basic properties. As shown it exists as a solid under 13.85 K as well as a liquid only in small temperature ranges of up to 20.25 K. Beyond its critical point, it is a supercritical fluid.

Table 2.1 Properties of hydrogen

Atomic weight	1.0079	gmol ⁻¹
Covalent radius	31	pm
Van der Waals radius	120	pm
Density at 273 K and 0.1 MPa	0.0899	g l ⁻¹
ΔH (H ₂ → 2H)	436	kJmol ⁻¹
Liquid density (20.25 K)	70.8	g l ⁻¹
Boiling point	20.25	K
Critical temperature	32.97	K
Critical pressure	1.276	MPa
Flammability limit in air	4.1 – 74.2	Vol. %
Self-ignition temperature	747	K
Explosive limits in air	18.3 – 59	Vol. %
Diffusion coefficient in air	0.634	cm ² s ⁻¹

An invisible flame forms when hydrogen burns. In addition, the combustion occurs over a vast concentration range in air. Because of these, safety concerns over hydrogen come into play. In the event of an accidental hydrogen release, a strong buoyancy and a fast atmospheric volatilization is caused due to its weight which is about 14 times less than air and its high coefficient of diffusion. Gasoline, on the other hand, does not quickly diffuse and forms toxic, nonbuoyant fumes. Table 2.2 compares the safety properties hydrogen with other fuels. Regardless of the broad flammability range of hydrogen, its lower flammable limit is considerably greater than that of most fuels. Its autoignition temperature falls within that of other fuels. A report on behalf of Ford Motor Company says that the safety of a hydrogen fuel cell vehicle would be potentially superior to a propane or gasoline vehicle (Zumerchik, 2001; Thomas, 1997).

Table 2.2 Safety properties of different fuels in air (Zumerchik, 2001; Thomas, 1997; Tzimas et al., 2003; Dean, 1999).

Fuel	Explosive limits Vol. %	Flammable limits Vol. %	Buoyant velocity ms ⁻¹	Autoignition temp. K	Ignition energy ^a mJ
Hydrogen	18.3 - 59.0	4.1 - 74.2	1.2 - 9.0	673 - 858	10
Methane	6.3 - 13.5	5.3 - 15.0	0.8 - 6.0	923	20
Ethane	-	3.0 - 12.5	- ^b	788	-
Propane	3.1 - 7.0	2.3 - 9.5	- ^b	723	-
Butane	-	1.9 - 8.5	- ^b	678	-
Gasoline	1.1 - 3.3	1.4 - 7.6	- ^b	553 - 729	-
Methanol	-	6.0 - 36.5	- ^b	743	-
Ethanol	-	3.3 - 19.0	- ^b	696	-

^a Ignition energy at a lower flammability limit. It is significantly low for stoichiometric mixtures (e.g., 0.02 mJ for hydrogen).

^b Nonbuoyant, due to higher density than air (1.2 kg m⁻³) under standard conditions.

Hydrogen is considered an ideal secondary energy carrier as a result of its high conversion efficiency and zero emission to greenhouse gases or toxic pollutants. Renewable energy and water can be used to produce hydrogen. This hydrogen when stored can be reversed back into

energy and water in another space and time. No contamination is formed in the course of the conversions.

The major impediments to a hydrogen economy today are its production and storage. This calls for inexpensive methods for its mass production. At the same time economic, efficient, and storage technologies that are safe ought to be developed so that it can contend with less costly fossil fuels (Zumerchik, 2001).

2.4 General Requirements for Hydrogen Storage Systems

It has been established that the methods used for commercial hydrogen storage applications are supposed to be compact, safe, long lasting, light and pollution free. In 2011, the U.S. Department of Energy (DOE) established additional requirements that are specific to large scale hydrogen storage application systems.

- The gravimetric capacity must be high. Relatively light containers are expected to be used in storing hydrogen so as to achieve a large wt% of hydrogen in the entire system, with a target of 5.5 wt % by 2017.
- Volumetric capacity should be high so that excessive volume of the system can be avoided. The goal is to reach 0.040 kg L^{-1} by 2017.
- Loading and unloading in the storage system should be made possible many times (the preferred being 1500 cycles) without any significant changes or losses in the system.
- In 3 minutes, the system is expected to be reloadable with 5 kg of hydrogen so that the time that consumers will have to wait will be reduced. Likewise, the unloading time is expected to be sufficiently fast so that a fuel cell or an engine can be supplied with the preferred pressure or gas flow.

- The conditions of operation should be near to ambient conditions. The temperature of operation must range from - 40 °C to 60 °C. Likewise, the delivery pressure should be high (100 bars).
- Less costly, abundant and environmental friendly materials should be used to manufacture the hydrogen storage systems. The method of storage should have high energy efficiency and also prolonged lifetime so that the materials used can be recyclable.
- A safe system should be designed so that the possibility of leakage, explosion, pollution or radiation can be completely avoided. This part is very crucial as it connects to societal acceptance establishment.

Intensive research has been carried out in the last few decades on prospective hydrogen storage methods. Nonetheless, none of the currently available materials that are used entirely satisfy all the criteria set by the U. S. DOE.

These materials often chemically or physically sorb H₂ within the solid substrate. The potential energy diagram in Figure 2.1 portrays this interaction. From the diagram, two energy minima curve with varying depths show how the H₂ approaches the solid surface. The curve at smaller distance from the adsorbent (substrate) corresponds to the equilibrium distance for chemisorption of H₂ whilst the other at greater distance corresponds to the distance for physisorption of H₂.

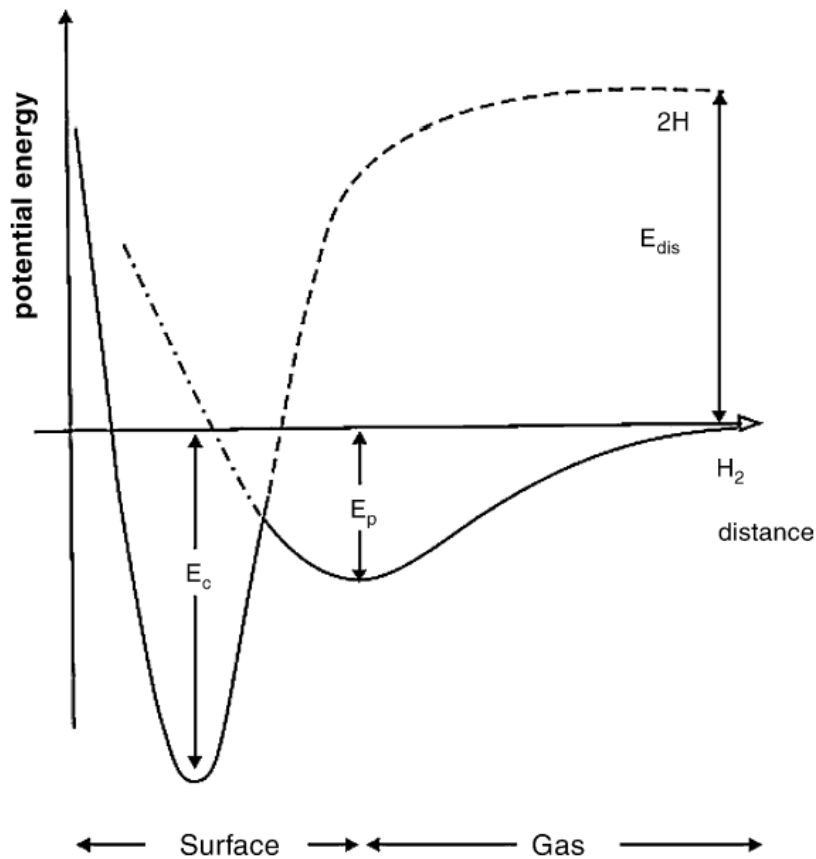


Figure 2.1 Potential energy curve for hydrogen which is chemically and physically adsorbed on the surface of an adsorbent versus how far it is from the surface.

Compounds that contain hydrogen (e.g. chemical hydrides, metal hydrides, nitrides and complex hydrides) are used in the chemisorption approach, out of which the hydrogen can be liberated at specific conditions (typically high temperature heating). On this basis, chemisorption is essentially a process of activation where by supplementary energy is used in the breaking of the chemical bond connecting hydrogen and the other elements. This makes hydrogen recovery from those materials inefficient in energy, as well as pose challenges to the recycling of such hydrides. For instance, magnesium hydride (a cheap naturally abundant and most researched compound) has been found to contain high hydrogen storage capacity of up to 7.6 %. However, the hydrogen is only released after heating to 300 °C (Dornheim et al., 2007). Out of this storage capacity, 2.4 wt% is used to feed the high endothermic reaction

leaving the remaining 5.2 wt% available for use. Magnesium hydride's slow kinetics, high thermodynamics and poor cyclabilities therefore prevent it from being adopted widely for practical applications. Nonetheless, the hydrides have recently been found to have improved cyclabilities, increased kinetics and a decreased hydrogen release temperature making them ideal hydrogen storage contenders (David, 2011).

The physisorption approach on the other hand occurs on a majority of porous materials. Here, the hydrogen gets adsorbed as a monolayer at a temperature which is higher than its boiling point. Weak interaction forces (dispersive, long-range attractive, short-range repulsive and van der Waals) between the hydrogen and the surface of the adsorbent is what causes the physisorption. A shallow minimum which is about one molecular radius away from the surface of the solid as depicted in Figure 2.1 is as a result of a blend of these interactive forces. The formation of an adsorbate monolayer leads to the interaction between the gaseous molecule and the solid adsorbate. As such, the energy of adsorption of the adsorbates on the second layer is comparable to the adsorbate's latent heat of vaporization. Adsorption at a temperature that is higher than the adsorbate's boiling point and a specific pressure subsequently results in a monolayer adsorption with an interaction energy which lies between 1 and 10 kJmol⁻¹ (Yang et al., 2007; Nishihara et al., 2009). Hydrogen is adsorbed in its molecular form since its adsorption enthalpy is very small to cause its H - H bond to break. Due to this small adsorption enthalpy associated with physical adsorption, low temperatures are needed to ensure high storage capacities. Likewise, the absence of an activation energy barrier in physisorption typically makes it to occur with fast kinetics.

2.5 Nickel Metal Hydride (Ni-MH) Battery

The Ni-MH battery is a form of green rechargeable battery that consists of an electro-negative (anode) and an electro-positive electrode (cathode). Amidst these two electrodes is a separator and the liquid electrolyte KOH (Nagarajan and Zee, 1998). A nickel hydroxide and a hydrogen storage alloy are respectively used as the cathode and anode. Due to the use of KOH as an electrolyte, it is classed as an alkaline storage secondary battery. Studies into rechargeable Ni-MH batteries started around 1950. However, the breakthrough for large-scale applications was achieved in the 1980s due to cobalt-aluminium modified LaNi_5 hydrogen alloys' development (Beek et al., 1985). Ovonic Battery Company, Sanyo, and Matsushita independently realized its commercialization in 1989 with AB_2 and AB_5 metal hydride (MH) alloys.

The Ni-MH and lithium-ion batteries were concurrently introduced into the market in 1991. It is based on a proton intercalation reaction. Developments on the positive electrode have mainly been geared towards its fundamental aspects. They include the elucidation of the crystal structure of the nickel oxy-hydroxide (NiOOH) phase. A lot of attention has on the other hand been focussed on the use of intermetallic compounds as materials for the negative electrode (Cuevas et al., 2001). Rare-earth mixtures with composition similar to that of ores ("Mishmetal") are preferred for use in commercial cells on the grounds of cost. Investigations have been conducted on different families of alloys that contain an early transition or rare-earth metal (A) and a late transition metal (B) in formulations such as AB, AB_2 and AB_5 . A has a stronger affinity for hydrogen whilst B has a weaker affinity for hydrogen. Much success has been attained with the AB_5 -type alloys. Advances in this area has greatly improved the performance (power and energy) of Ni-MH cells which are widely used in HEV. AB_5 -type alloys started progressing from being used in small cylindrical cells (0.7 – 5 Ah) for portable electronic devices to 100 Ah prismatic cells for applications in electric

vehicles. General Motors in 1999 were the first to produce modern age electric vehicles (EV1) that were commercially available. A 26.4 kWh Ni-MH battery pack was used in powering it. Ever since, over 5 million hybrid electric vehicles produced by Honda, Toyota, and other automobile companies have been powered by Ni-MH batteries, showing how robust and long-living the batteries are.

In the use of Ni-MH batteries for applications in small portable batteries, a yearly global commercial production in excess of 1 billion cells has been attained. Ni-MH batteries have found wide usage and have rapidly substituted the Ni-Cd batteries in portable electronic applications due to technical and environmental reasons. Their cycle life is long, energy density and rate capacity are high, tolerance to overcharge/overdischarge is superior, and at the same time are environmentally friendly (Wang et al., 2013; Conte et al., 2004). The performance merits of Ni-MH batteries over Ni-Cd ones in terms of energy is the fuelling of the rapidly growing portable electronic devices and substitution of primary alkaline batteries that are used in products like digital cameras (Ovshinsky et al., 2000). Today, it has turned into the leading advanced battery technology used in electric vehicles (EV) and hybrid electric vehicles (HEV) due to its unsurpassed overall performance in the wide range of requirements set by automobile companies.

The features below together with the vital performance targets of power, energy, operating temperature and cycle life have made the Ni-MH battery technology to dominate (Linden and Reddy, 2002).

- Operation at high voltage is safe
- Cell sizes are flexible mostly between 30 mAh and 250 Ah
- Vehicular packaging is flexible

- Application to series and series/parallel strings is easy
- Volumetric power and energy are excellent
- Charge and discharge are safe, as well as abusive overcharge and overdischarge are tolerated
- Cylindrical or prismatic cells are chosen
- Maintenance is free
- Regenerative braking energy is capable of being used
- Charging and electronic control circuits are simple and less costly
- Thermal properties are excellent
- Materials used are environmentally friendly as well as recyclable

Although Li-ion batteries exhibit several features, such as high voltage and high energy density, for most applications, Ni-MH batteries may be preferred to lithium batteries as the latter are more expensive.

2.5.1 Principles of Ni-MH batteries

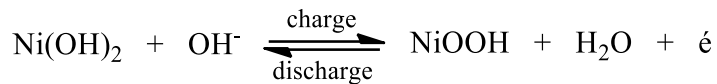
In the course of charging/discharging, electrochemical hydrogenation/dehydrogenation of some metals/alloys/intermetallics (M) are possible through the reaction below (Schlaphach, 1988; Sakintuna et al., 2007; Wronski, 2001).



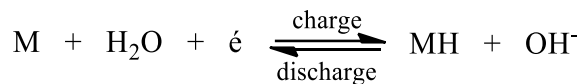
The “M” here is not just an electrochemical catalyst. It is also a hydrogen storage medium. A nickel hydroxide positive electrode combined with a hydrogen storage alloy electrode makes

a Ni-MH battery. From the scheme in Figure 2.2, the electrochemical reactions that occur in a Ni-MH battery can be shown as follows (Feng et al., 2001; Kleperis et al., 2001; Cuevas et al., 2001):

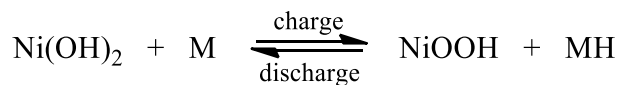
on the positive electrode:



on the negative electrode:



the overall reaction:



M (hydrogen storage alloy) and water react to form metal hydride and hydroxyl ions at the anode whereas Ni(OH)₂ is oxidized to NiOOH at the cathode upon charging. On discharging, the reactions occur in the opposite direction. The prominent features of the principle underlying a Ni-MH battery is that in the course of charging, hydrogen moves from the positive electrode to the negative electrode whilst during discharging it moves otherwise, with the electrolyte not partaking in the overall reaction (the “rocking-chair” mechanism). The hydride formation/ decomposition experiences a series of chemical reactions including interface reaction and mass transport. For application purposes of M in Ni-MH batteries, M must possess a high hydrogen capacity and moderate hydride stability.

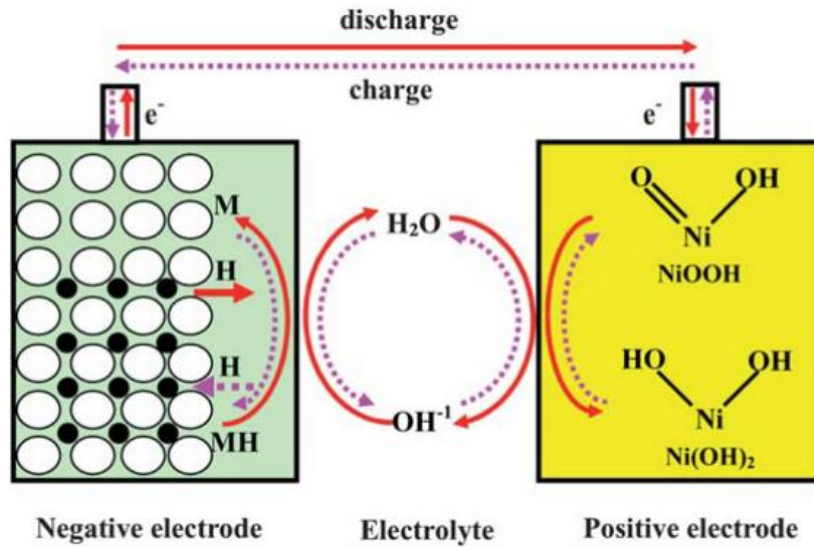


Figure 2.2 Schematic diagram of the electrochemical reaction process of a Ni-MH battery (Kleperis et al., 2001; Feng et al., 2001; Cuevas et al., 2001).

2.6 Ideal Perovskite Structure

The term perovskite generally defines a certain structural family in addition to being the name for a particular mineral with the formula CaTiO_3 (Bhalla et al., 2000). The ABO_3 perovskite oxides comprise of a rare-earth metal on A sites with twelve-fold oxygen coordination as well as a transition metal on B sites with six-fold oxygen coordination. They have been found to show a rich variety of unusual and interesting magnetic, electronic, and structural properties (Dogra et al., 2001), and in solid-state materials research they have gained much technological prominence. The ideal perovskite structure crystallizes in the $\text{Pm}\bar{3}\text{m}$ space group and can be viewed as a cubic closed packed (fcc) array formed by the O^{2-} anions and the large cation A, with the small B cation sited in the centre of the cube surrounded by the oxygen octahedra. An equivalent representation can be obtained through a displacement of the origin by $(1/2, 1/2, 1/2)$. In this representation the A cation is located in the centre of the cube surrounded by an oxygen octahedron, whereas the B cation is sited in the corners of the cube. These two structure representations are depicted in Figure 2.3. The

system can chemically be characterized by a wide range of cations that can occupy the A and B sites in the perovskite structure (e.g., SrTiO₃ at room temperature).

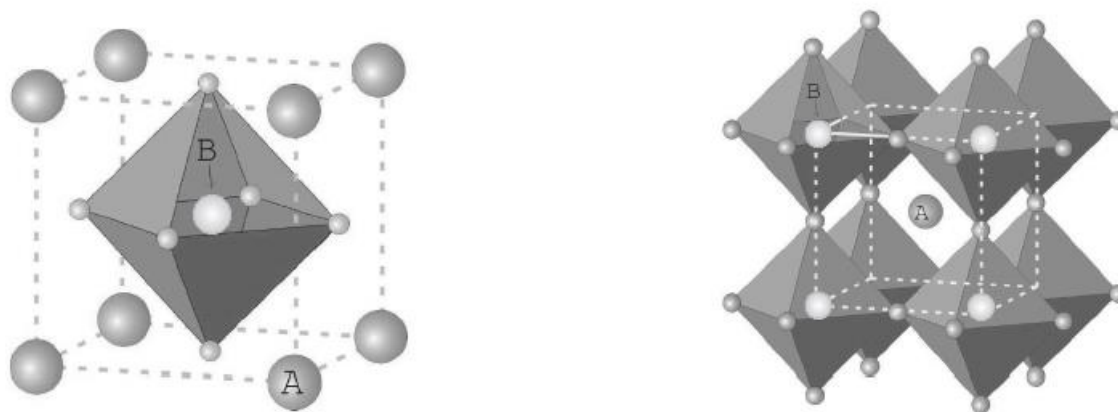


Figure 2.3 Schematic representation of the ideal perovskite structure. Left side, representation with the B cation sited in the centre of the structure surrounded by the O₆ octahedron. Right side, equivalent representation but with the A cation in the centre surrounded by twelve oxygen

The principal feature of all perovskite structures is the backbone that octahedral units of BO₆ form by sharing each of its vertices with another unit of BO₆. The A cations fill interstitial sites among the octahedra inside this framework. The B-site cations are generally 3d, 4d or 5d transition metal ions which can be active catalytically, whilst the A-site cations can be big alkali, rare-earth, alkaline-earth or other metal ions which are large. There are various potential options of A and B cations. Dissimilar ions can notwithstanding be combined to constitute a solid solution like AA'BB'O₃ yet maintaining the perovskite structure. In addition, the octahedron-formed backbone is likewise extremely versatile since there can be distortion of the regular octahedron in cubic Pm $\bar{3}$ m perovskite. There is thus the formation of huge and diverse oxide family with such diversity giving them many interesting attributes.

Glazer in 1972 developed a notation system to depict the octahedral tilting in perovskites. It is now called the “Glazer notation” and is denoted;

$$x^\alpha y^\beta z^\zeta \quad (1)$$

where $(x, y, z) = (a, b, c)$ and $(\alpha, \beta, \zeta) = (0, +, -)$

The tilting or distortion is accounted for in this notation by assigning the octahedral rotations around each of the Cartesian axes (x, y, z), and this rotation around each axis is described by two constituents which are the magnitude and direction. The rotation’s magnitude is articulated in a relative way. The rotation angles are equal around all axes (x, y and z) in a $a^+a^+a^+$ system for instance whilst the rotation angles are equal around x- and y-axis but differ around the z-axis in a $a^+a^+c^+$ system. The second constituent, the superscript, shows a description of whether the rotations of two neighbouring octahedral on the tilt axis are in a similar direction or not. The rotations of neighbouring octahedra along a specific axis which are opposite to each other is represented by a negative sign whilst those rotations in alike direction are represented by a positive sign. A zero superscript indicates the occurrence of no rotation about that axis (Woodward, 1997). Hence, in the notation by Glazer, the ideal non-distorted cubic perovskite with $Pm\bar{3}m$ symmetry has the description $a^0a^0a^0$, whilst the distorted orthorhombic structure with $Pbnm$ symmetry has $a^-a^-c^+$.

The charge on the cations in a perovskite-oxide system (ABO_3) should invariably sum up to 6 and the structure stabilization depends essentially on the A and B ionic radius, r_A and r_B . For an ideal cubic closed packed structure to be stabilized the ionic radius must conform to the relation:

$$\sqrt{2}(r_A + r_O) = 2(r_B + r_O) \quad (2)$$

where r_O is the ionic radii of oxygen.

The ideal cubic structure is usually distorted by cation size mismatch.

Because a lot of dissimilar metal ions function as A and B ions, it is practicable to come up with a way of rapidly guessing the stability of this combinations as well as the potential structure of the corresponding ABO_3 crystal. The tolerance factor can roughly be used as an estimation of the relative stability of the lattice structure of a perovskite-oxide (Goldschmidt, 1926).

2.6.1 Distorted Perovskite Structure - Tolerance Factor

The distorted cubic perovskite structures are frequently orthorhombic though other symmetries such as rhombohedral or tetragonal can be stabilized. The symmetry of distorted perovskites is reduced, which is necessary for their magnetic and electric attributes. The perovskite systems can accommodate considerably different cation sizes. Divalent cations which can occupy the A site include strontium, barium, calcium and lead; trivalent cations include praseodymium, lanthanum, neodymium, etc. Besides manganese, other 3d element such as cobalt, iron or nickel can be located on the B sites.

Table 2.3 Ionic radii (\AA) of some elements common in the perovskite structures

O^{2-}	Mn^{3+}	Mn^{4+}			
1.40	0.645	0.530			
Ba^{2+}	Sr^{2+}	Ca^{2+}	Cd^{2+}		
1.61	1.44	1.34	1.31		
La^{3+}	Pr^{3+}	Nd^{3+}	Sm^{3+}	Eu^{3+}	Tb^{3+}
1.36	1.30	1.27	1.24	1.23	1.20

Table 2.3 above presents the ionic radii of some elements that can be accommodated in the perovskite structure. The deformation of the ideal cubic cell to accommodate the different cation sizes can be quantified by the tolerance factor, t introduced by Goldschmidt.

$$t = \frac{r_A + r_O}{\sqrt{2}(r_B + r_O)} \quad (3)$$

This factor, which is one for the ideal cubic structure, can also be expressed using the interatomic distances between the oxygen and the ions at A and B sites (d_{A-O} and d_{B-O} respectively)

$$t = \frac{d_{A-O}}{\sqrt{2}d_{B-O}} \quad (4)$$

As the value of t departs from one, internal stresses increases and the cubic lattice becomes unstable. In a particular case of $t < 1$ the perovskite B-O bonds are under tension whereas A-O bonds are under compression and thus one observes a cooperative rotation of the BO_6 octahedra and a corresponding reduction of the B-O-B bond angle from $\varphi = 180^\circ$. The possible structure of the perovskite is shown by the tolerance factor, t value. The rhombohedral structure is often seen when t is close to one. This structure matches up to a small rotation of the oxygen octahedra around a $[1\ 1\ 1]$ axis of Figure 2.3. As the tolerance factor further deviates from one the cation misfit is accommodated by a collective buckling of the oxygen octahedra which corresponds to a rotation about the $[1\ 1\ 0]$ axis.

2.7 Lanthanum Ferrite ($LaFeO_3$)

ABO_3 perovskite compounds have been the subject of many researches for their various physical and chemical properties (Wang and Kang, 1998). Ferrites are technologically important materials. They have been extensively investigated to extend their domain of applications in electronics. In general, ferrite materials are receiving much attention in high frequency applications such as inductors, waveguides, isolators, circulators, and phase shifters. Lanthanum ferrite is however of great interest as one of the most common perovskite-type oxides, with an orthorhombic perovskite structure, space group $Pbnm$ (most common for perovskite oxides (Avdeev et al., 2007), No. 62), where the distortion from the

ideal cubic structure occurs to form the tilting of the FeO_6 octahedra. It is a parent compound for solid solutions widely applied as materials for fuel cell cathodes (Hung et al., 2007), potential negative electrode materials in nickel-metal hydride batteries (Deng et al., 2010), mixed conducting oxygen permeable membranes, chemical sensors for the detection of humidity and alcohol (Berenov et al., 2008) and catalyst material for complete hydrocarbon oxidation (Ciambelli et al., 2001). These technological applications are due to the unique structural characteristics of perovskites which are largely influenced by processing conditions.

LaFeO_3 is a distorted perovskite and show temperature-dependent structural and magnetic phase transitions. At ambient temperature this compound has a distorted perovskite structure (Geller and Racah, 1970) which is orthorhombic and of the type GdFeO_3 (space group Pbnm) and transform to rhombohedral structure (spacegroup $\text{R}\bar{3}\text{c}$) at high temperature (~ 1200 K for LaFeO_3) followed by large volume shrinkage with the involvement of absorption of heat (Hashimoto et al., 1998). This phase transition should be first order from group theory and has been affirmed by experiment (Fossdal et al., 2004; Howard and Stokes, 1998). Moreover, at elevated temperatures (> 1800 K), another phase transition which is from rhombohedral to cubic structure has been observed (Geller and Racah, 1970).

2.7.1 Structure of LaFeO_3

Lanthanum ferrite (or orthoferrite) is the least distorted of the rare earth orthoferrite series. These ferrites have perovskite structures which are orthorhombic. In Figure 2.4, LaFeO_3 structure is depicted. The iron sublattice is nearly cubic and the iron ions are octahedrally surrounded by the oxygen ions. The Fe-O-Fe bond angle ($\theta \approx 156^\circ$) of LaFeO_3 is the largest in the orthoferrite series (Boekema et al., 1979).

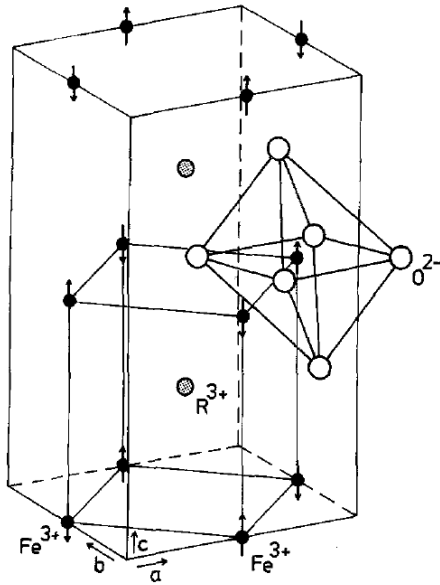


Figure 2.4 The crystal structure of LaFeO_3

The magnetic structure is determined by the antiferromagnetic superexchange between the Fe ions. LaFeO_3 is an antiferromagnetic insulator with $T_N = 747 \text{ K}$ (Boekema et al., 1979). It is essential to apply a correction (absorption, Lorentz and polarization) since the twinning in LaFeO_3 is so prevailing (Marezio and Dernier, 1971).

Fe^{3+} in the B site of perovskites have computationally been predicted to be low spin at high pressures (Hsu et al., 2011; Li et al., 2005; Stackhouse et al., 2007). Experimental studies on the other hand have indicated that Fe^{3+} undergoes a transition from high spin to low spin in the B site of the Pbnm perovskite phases of LaFeO_3 and PrFeO_3 at 30 – 50 GPa (Xu et al., 2001), and MgSiO_3 perovskite at 0 – 55 GPa (Catalli et al., 2010).

2.7.2 Crystal Data of LaFeO₃

Melting LaFeO₃ powder in an iridium crucible in air and cooling it slowly can lead to the preparation of LaFeO₃ crystals. LaFeO₃ exists in the space group Pbnm and has four formula weights per unit cell. The four lanthanum atoms and the four iron atoms are in the 4(c) (x, y, 1/4) and 4(b) (0, 1/2, 0) special positions respectively. Four of the twelve oxygen atoms are in the 4(c) (x, y, 1/4) special positions whilst eight are in the general positions. A Norelco camera of diameter 114.6 cm and radiation CrK α in 1971 was used to take a powder film at room temperature out of which the lattice parameters, $a = 5.553 \pm 0.002 \text{ \AA}$, $b = 5.563 \pm 0.002 \text{ \AA}$ and $c = 7.867 \pm 0.003 \text{ \AA}$ were determined (Marezio and Dernier, 1971).

2.8 Relaxation and Reconstruction of Surfaces

The phenomena of relaxation and reconstruction involve rearrangements of surface (and near surface) atoms, a process being driven by the energetics of the system i.e. the desire to reduce the surface free energy. As with all processes, there may be kinetic limitations which prevent or hinder these rearrangements at low temperatures. Both processes may occur with clean surfaces in ultrahigh vacuum, but it must be remembered that adsorption of species onto the surface may enhance, alter or even reverse the process. Unlike relaxation, the phenomenon of reconstruction involves a change in the periodicity of the surface structure and in some cases also a change in surface symmetry.

2.9 Hydrogen Adsorption on Surfaces

The stable form of elemental hydrogen under normal conditions is the dihydrogen, and in the adsorption process hydrogen will associate with a material's surface either as hydrogen molecule (H₂) or hydrogen atoms. La, Fe, and O dihydrogen and dihydride bonds have also been found to exist in some metal complexes. The interaction of H₂ with transition metal

complexes during oxidative addition is usually thought to proceed through a dihydrogen complex, followed by scission of the H – H bond to give a dihydride complex (Deutsch and Eisenberg, 1988; Kubas, 2001). This reaction is central to catalytic hydrogenation. Kubas and co-workers in 1984 first discovered the formation of transition metal dihydrogen complexes. Fe dihydrogen bonds have since been found to form in zeolites notably by the binding of H₂ to the extra framework iron in Fe - ZSM5 at 110 K (Mojet et al., 2001). Iron dihydride, FeH₂ was first identified in the reaction of Fe atoms with hydrogen in low temperature matrices (Ozin and McCaffrey, 1984). All the rare-earth metals also form dihydrides (except for europium and ytterbium) that have the fluorite type structure and easily take up additional hydrogen to form trihydrides (Mueller, 1968). La is known to have an excellent affinity for hydrogen, and often form a hydride. Owing to rare-earth metals' affinity to hydrogen, the rare-earth metals are widely used as constituent elements of hydrogen storage materials.

CHAPTER THREE

3. COMPUTATIONAL METHODOLOGY

3.1 Computational Procedures of the Quantum-ESPRESSO Code

Quantum-ESPRESSO (QE), an open-source code, is used to perform all the first-principles calculations presented in this thesis. QE is an integrated suite of computer codes for electronic structure calculations and materials modelling based on density-functional theory, plane-wave basis sets and pseudopotentials to represent electron-ion interactions (Giannozzi et al., 2009). It is free software distributed under the terms of the GNU General Public License (GPL). The computational procedure of the QE code includes an iterative solution of the Kohn-Sham equations and optimized charge-density mixing routines. This includes the calculation of the Hellmann-Feynman forces acting on the atoms and the stresses on the unit cell. The total energy is optimized with respect to the positions of the atoms within a unit cell.

3.2 The Plane-wave self-consistent field method

The set of Kohn-Sham equations is strongly non-linear and has to be solved through an iterative method.

The plane-wave self-consistent field (PWscf) method implements an iterative approach to reach self-consistency, using at each step iterative diagonalization technique in the framework of the plane wave pseudopotential method. The procedure followed to do the self-consistent calculation is: one first makes a trial guess for the wave functions of all electrons and calculate its effective Kohn-Sham potential, V_{KS} . With this effective potential, the Kohn-Sham equation is solved to get a new wave function. From these, a new V_{KS} is calculated, and so on. The procedure is terminated when the charge density does not vary much anymore. At this point self-consistency is reached, meaning that the wave function and the

effective potential are self-consistent with each other, i.e. the wave functions correspond to those that one would get from solving the Schrodinger equations using that potential. Both norm-conserving (NC) and ultrasoft (US) pseudopotentials are implemented in the PWscf method.

3.3 Important Input Parameters

There are few input parameters that are optimized to find a compromise between expediting the computational procedure to find the ground state energy, but with an appropriate accuracy (Lee, 2012).

The wave functions of a system depend on the electronic configurations of the constituent atom(s). The pseudopotential simplifies these wave functions to expedite the computational procedure. Generally, valence electrons participate in chemical reactions, bond formation, electronic structure, and thermodynamic properties of materials. Therefore, the pseudopotential approach freezes the nucleus and core electrons into an approximated potential. The wave functions of the valence electrons are only considered, and using the pseudopotential approach further simplifies these wave functions (Lee, 2012).

K-points are unique points used to solve the Kohn-Sham equations within the irreducible Brillouin zone. Systems with high symmetry utilize less k-points, thereby expediting the computation procedure; likewise, systems with low symmetry require more k-points, which increase the computational time. The k-point is a system-dependent term, and is optimized not only to expedite the computational procedure, but to provide acceptable accurate results too (Lee, 2012).

Kinetic energy cut-off (E_{cut}) is a system-dependent term, which is included to restrict the wave function expansion to a finite value. The E_{cut} term is optimized not to only expedite the computational procedure, but to provide acceptable accurate results as well (Lee, 2012).

Generally, the supercell approach is applied when a “non-periodic entity” such as a defect is included into the system (Lee, 2012). The size of the supercell is optimized to avoid any unphysical interaction between the defect and corresponding images (Lee, 2012).

3.4 Input File for a Simple PWscf Calculation

The input file for PWscf is constructed in a number of NAMELISTS and INPUT_CARDS. The use of NAMELISTS allows specifying the value of an input variable only when it is needed and to define default values for most variable that need not be specified. They are read in specific order and are ignored if not required. Three NAMELISTS are mandatory in PWscf. The first is &CONTROL which consists of the input variable that control the flux of the calculation and the amount of input/output on disk and on the screen. Input variables specifying the system under consideration are listed in &SYSTEM. The third mandatory NAMELIST is &ELECTRONS, which contains the input variables that control the algorithms used to reach the self-consistent solution of the Kohn-Sham equations for the electrons.

INPUT_CARDS on the other hand are used to provide input data that are always needed and would be boring to specify with the `variable_name = variable_value` syntax used by NAMELISTS. Similarly, there are three mandatory INPUT_CARDS. The name, mass, and pseudopotential used for each atomic species present in the system are specified in ATOMIC_SPECIES. ATOMIC_POSITIONS is where the type and coordinates of each atom in the unit cell are specified. K_POINTS is the last mandatory INPUT_CARD that contains

the coordinates and weights of the k-points used for the Brillouin zone integration. A typical input file for a self-consistent field, scf calculation is shown below.

```

&CONTROL
  title = 'Lanthanum iron trioxide' ,
  calculation = 'scf' ,
  restart_mode = 'from_scratch' ,
  outdir = './tmp' ,
  pseudo_dir = '/home/mmc6/Isaac/Database/pseudo' ,
  prefix = 'LaFeO3'
  tstress = .true. ,
  tprnfor = .true. ,
/
&SYSTEM
  ibrav = 0,
  celldm(1) = 1.88972599,
  nat = 20,
  ntyp = 4,
  ecutwfc = 30,
  ecutrho = 180,
  occupations='smearing',
  smearing='fermi-dirac',
  degauss=0.003,
  nbnd=100
  nspin=2,
  starting_magnetization(1)=0.5,
  starting_magnetization(2)=-0.5,
/
&ELECTRONS
  conv_thr = 1.0D-6
  mixing_beta = 0.2,
  electron_maxstep = 10000,
/
ATOMIC_SPECIES
Fe1 55.845 Fe.pbe-sp-van.UPF
Fe2 55.845 Fe.pbe-sp-van.UPF
La 138.90547 La.pbe-nsp-van.UPF
O 15.9994 O.pbe-van_ak.UPF
ATOMIC_POSITIONS (alat)
Fe1 2.809553535 -0.010598654 0.028501161
Fe2 0.043244081 2.807755707 0.028222496
Fe1 0.043360310 2.807576896 3.966950747
Fe2 2.809470235 -0.010860505 3.966772896
La 5.517610199 0.238890644 1.996466303
La 2.750932864 2.558758552 5.937076507
La 0.102092648 5.376887026 5.937106740
La 2.863769221 3.057538723 1.996421825
O 0.530287897 2.671692955 1.997369735
O 3.969272892 1.633025927 0.396225007
O 1.204890243 1.160389081 7.538712891
O 3.294280396 0.123272202 5.937091527
O 1.204253941 1.159627600 4.335530039
O 3.968705350 1.632679744 3.596679170
O 5.085498417 2.940965815 5.937161881
O 1.646750197 3.981103801 7.537998927
O 2.322913776 -0.148088039 1.997351290
O 4.412182879 4.452828867 0.395999186

```

```

O          4.412802272    4.452593173    3.597040820
O          1.647528646    3.980360487    4.336220851
K_POINTS automatic
  4 4 3    0 0 0
CELL_PARAMETERS
  5.528690010    0.000137965   -0.000001443
 -0.000043924    5.638002659    0.000042934
  0.000002739   -0.000058790    7.878646078

```

3.5 Computational Details

The structures and total free energies were determined using the density functional theory (DFT) method with plane wave basis and the ultra-soft (Vanderbilt) pseudopotentials within the Quantum-ESPRESSO package. Perdew-Burke-Ernzerhof exchange-correlation (PBE) functional was used within the Generalized Gradient Approximation (GGA) and Generalized Gradient Approximation plus U (GGA+U) for electronic interactions. Ultrasoft pseudopotentials were used, where 5s, 5p, 5d, 6s, and 6p states are considered for La with 11 electrons, 3s, 3p, 3d, 4s, and 4p states for Fe with 16 electrons, 2s and 2p states for O with 6 electrons and 1s state for H with 1 electron. The integrations over the Brillouin zone was performed through the point sampling technique of Monkhorst and Pack (Monkhorst and Pack, 1976) with k-points in the relevant irreducible wedge (Perdew et al., 1996). Spin-polarization was considered for all calculations.

The Fermi surface effects were treated by the smearing technique of Fermi-Dirac, using a smearing parameter of 0.003 Ry. An energy threshold defining self-consistency of the electron density was set to 10^{-6} eV and a mixing beta defining mixing factor for self-consistency was also set to 0.2. Using convergence tests, the Kohn-Sham wave functions were expressed with plane wave basis set cut-off energy of 30 Ry and a charge density cut-off of 180 Ry. Also, from convergence tests, a Monkhorst-Pack k-point grid of (4 x 4 x 3) was used for the bulk material and (4 x 4 x 1) for the slab (because of vacuum introduction)

Brillion zone sampling. Visualization of structures were done using the XCrySDen programme (Kokalj and Causa, 2000; Kokalj, 1999).

The surface was treated as polar (due to the prevalent twinning in it) and described with the slab model, where periodic boundary conditions are applied to the central super-cell and reproduced periodically throughout space. The surface (miller index) was created from the optimized bulk using the METADISE code (Watson et al., 1996), which does not only consider periodicity in the plane direction but also provides the different atomic layer stacking resulting in a zero dipole moment perpendicular to the surface plane, as is required for reliable and realistic surface calculations. A vacuum of 12 Å was introduced to the surfaces high enough to avoid any spurious interaction between repeated cell units in the z-direction. The (0 1 0) slab was modelled to a thickness of one in the z-direction, i.e. p (1 x 1) with five atomic layers in a La-O-Fe surface termination to reduce computational cost since the surface already contained four LaFeO₃ formula units (20 atoms). The Hubbard U term was not included in all surface calculations as the GGA has been found to reproduce the structural properties of any system adequately, and as such give quite good total energy.

In all the calculations, the atomic positions of the surface layers were allowed to relax. This avoids the formation of artificial dipoles and makes it necessary to include a relatively large number of layers. It also serves as a test of whether we have included a sufficient number of layers in the slab models: If this is the case, the middle layers are expected to be very close to the bulk geometry after relaxation. (Hadidi, 2012).

The atomic positions of the adsorbate (hydrogen) were also allowed to relax. The calculated bond length (structural parameter) for gas-phase H₂ molecule was obtained by putting a molecule of hydrogen in a 10 Å × 10 Å × 10 Å cubic crystal. The possible adsorption configurations investigated for one H₂ adsorption at a molecular, dihydrogen and dihydride

bond distance were: *O17-top end-on* and *side-on*, *O18-top end-on* and *side-on*, *O19-top end-on* and *side-on*, *O20-top end-on* and *side-on*, *Fe3-top end-on* and *side-on*, *Fe4-top end-on* and *side-on*, *La7-top end-on* and *side-on*, *La8-top end-on* and *side-on*, *Fe3-O19 bridging*, *Fe3-O20 bridging*, *Fe4-O19 bridging*, *La8-O19 bridging*, *La8-Fe4 bridging*, *La7-O17 bridging*, *La7-O20 bridging*, *La7-Fe3 bridging*, *La8-O17 bridging*, *La8-O18 bridging*, *La8-Fe3 bridging* and *La8-La7 bridging*, where *end-on* and *side-on* refer to horizontal and vertical configurations respectively. The amount of charge gained by the H₂ from the LaFeO₃ (0 1 0) surface was calculated using the Löwdin scheme.

The potential for La hydride formation on LaFeO₃ (0 1 0) surface was also investigated. For a more realistic adsorption system, an additional H₂ molecule was adsorbed on an already adsorbed *Fe3-O19 bridge* site (which was the most stable adsorption site when one H₂ was adsorbed) at the *O-top end-on*, *Fe-top end-on*, *Fe-top side-on*, *La-top side-on*, *Fe-O bridge* and *Fe-O bridge** adsorption configurations (where *Fe-O bridge** is the adsorption site when H-H bond length is a typical dihydride one) to simulate the new H₂ adsorption on the LaFeO₃ (0 1 0)/H₂ surface. The potential of H₂O as a good leaving group in LaFeO₃ (0 1 0)/2H₂ at the *Fe-O bridge** site was also investigated with the help of constrained optimization/ dynamics.

CHAPTER FOUR

4. RESULTS AND DISCUSSION

4.1 Input Parameters for Lanthanum Ferrite (LaFeO_3)

Certain input_cards like kinetic energy cut-off, E_{cut} , k-points and effective Hubbard U must first be calculated to get a true representation of the system under study.

4.1.1 Convergence Tests for Kinetic Energy Cut-off, E_{cut} and K-points

Convergence test for kinetic energy cut-off, E_{cut} which is used for total electronic energies convergence using a plane wave basis was performed and the outcome is shown in Figure 4.1. This E_{cut} is the only parameter in theory which controls the accuracy of description of a system and is a property of the pseudopotential used. From the test, 30 Ry was chosen and used for the smooth part of the electronic wave functions. This was used throughout all calculations, both in the bulk and slab models. This was chosen as it is the least converged point on the curve which will make the calculations computationally less expensive.

Similarly, convergence test for the k-points which are unique points used to solve the Kohn-Sham equations within the first irreducible Brillouin zone was determined. K-points are inversely proportional to the lattice parameters. The larger the cell size in a given direction the smaller the k-points required to sample in that direction and vice-versa. From the test

(Figure 4.1), k-point grid of $4 \times 4 \times 4$ was chosen. However, because of the orthorhombic nature of LaFeO_3 with lattice parameters $a = 5.6266$, $b = 5.6083$ and $c = 7.9401$ (Selbach et al., 2012), the k-points in the c direction was reduced. $4 \times 4 \times 3$ and $4 \times 4 \times 1$ Monkhorst-Pack (Monkhorst and Pack, 1976) k-point meshes were therefore used for all the bulk and surface calculations respectively in conformity with works of Javaid and Akhtar (2014), Ritzmann et al. (2013), and Liu et al. (2009).

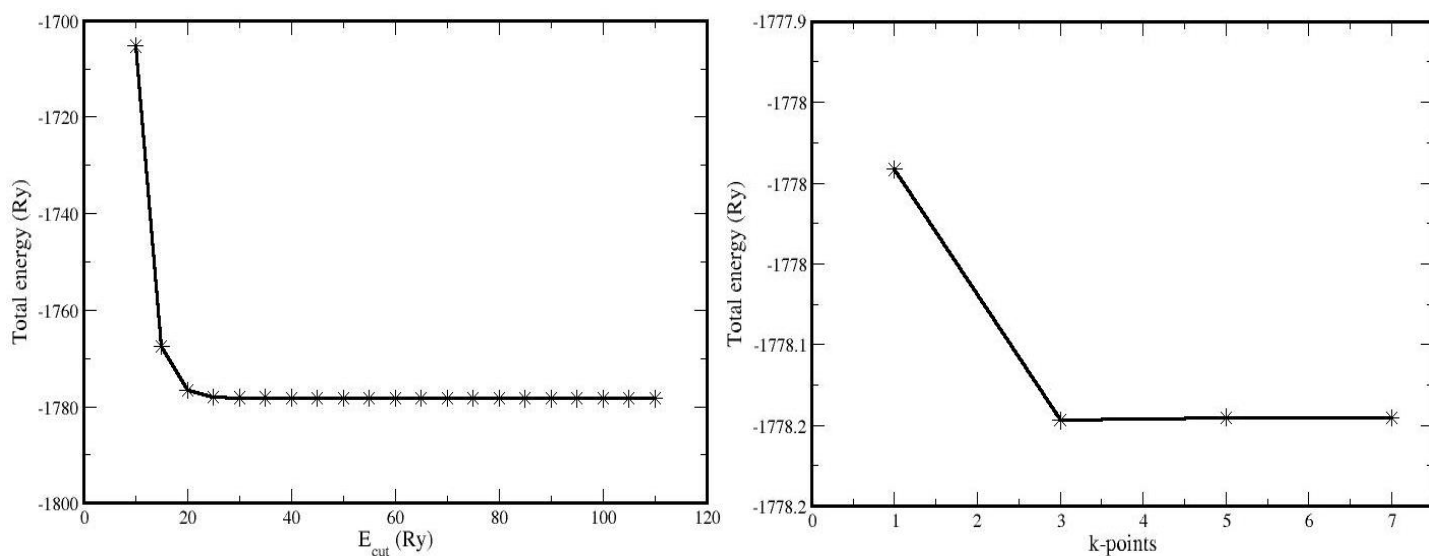


Figure 4.1 Convergence test for plane wave cut off energy, E_{cut} and Monkhorst-Pack k-points grid

4.1.2 Effective Hubbard U , U_{eff} for LaFeO_3

In a lot of DFT+ U works, the U parameter used is obtained by considering the value reported by other authors, or by varying the Hubbard U term and taking the larger value capable of accurately reproducing a physical property taken as a control parameter. An important limitation of the former approach is the fact that the value of U is usually related to the pseudopotential formulation used throughout the calculation. On the other hand, the latter approach suffers from the fact that though a value of U can accurately describe one property, the same value will generally lead to large discrepancies for other properties of the same material. In this work, the U parameter is expected to be consistent within the framework of

first-principle calculations, and to accurately reproduce not only the band gap and magnetic moment, but also the geometry (lattice vectors) of the LaFeO₃ material.

The effective Hubbard U parameter (U_{eff}) which corresponds to the difference between Coulomb (U) and exchange (J) energy, i.e., $U_{\text{eff}} = U - J$, for LaFeO₃ was determined by plotting the electronic band gap, E_g (difference between highest occupied and lowest unoccupied eigenvalues at the different k-point paths and at the spin up spin-polarization) against different U_{eff} values as depicted in Figure 4.2 below. From this figure the theoretically determined value is 4.64 eV which was obtained by extrapolating the experimental band gap of 2.46 eV (Venkaiah et al., 2013; Liu et al., 2015) to the U_{eff} axis. This effective Hubbard U is however 4.0 according to Wang et al., 2006 for Fe²⁺ when oxidation energies of FeO was plotted as a function of U, and 4.3 eV according to Mosey et al., (2008) for Fe³⁺ when Unrestricted Hartree-Fock (UHF) calculations were performed on electrostatically embedded Fe₂O₃ clusters. U is hereafter used to represent U_{eff} .

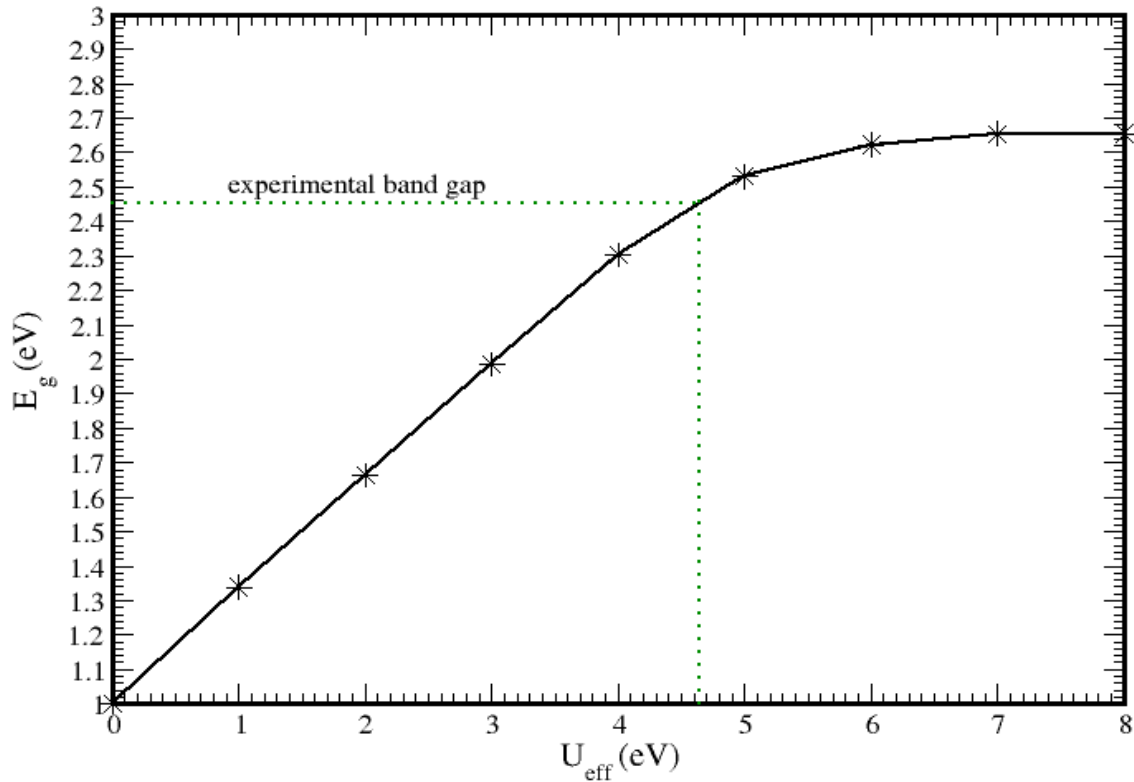


Figure 4.2 Electronic band gap, E_g for LaFeO_3 plotted against different U_{eff} values

4.2 Bulk Structures (Properties) and Some Electronic Properties of LaFeO_3

4.2.1 Bulk Properties of LaFeO_3

The spin density distribution of any material should adequately be described by the calculation method used. Fe has a magnetic moment and as such its spin orientation in LaFeO_3 becomes very necessary. From Table 4.1 below, the most stable spin polarization configuration among the antiferromagnetic states which describes its magnetic ordering is the (1 2 1 2) with energy - 24196.279878652 eV, where 1 and 2 represent spin-up and spin-down respectively.

Table 4.1 Electronic state of LaFeO_3 bulk

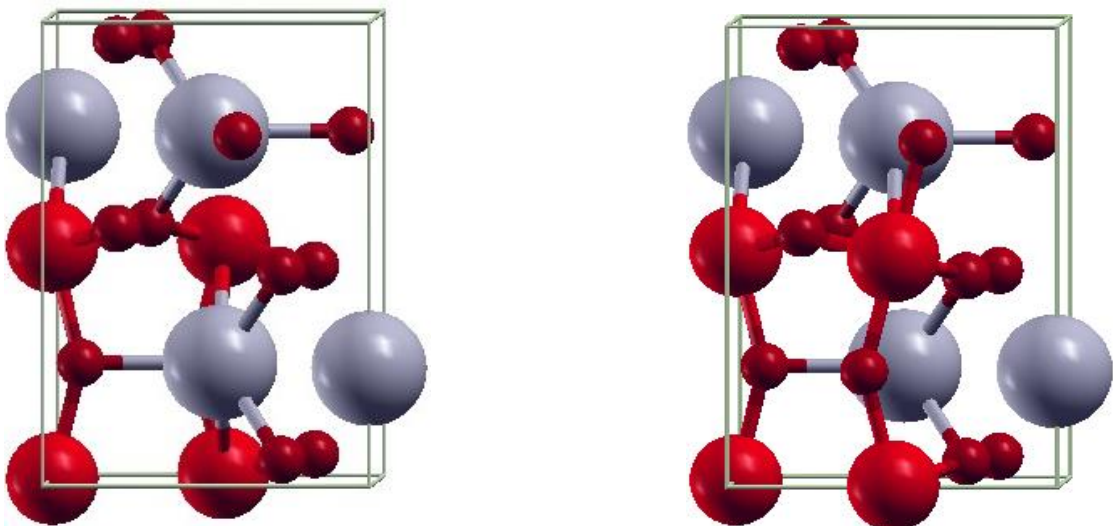
Configuration	Energy / eV	Spin polarization
1 1 1 1	-24196.020312913	Ferromagnetism

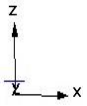
1 2 1 2	-24196.279878652	Antiferromagnetism
1 1 2 2	-24195.723688911	Antiferromagnetism
2 1 2 1	-24196.279878650	Antiferromagnetism
2 2 1 1	-24195.723689046	Antiferromagnetism

where 1 and 2 represent spin-up and spin-down respectively.

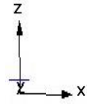
Comparing this energy with that of the ferromagnetic state (1 1 1 1), the Generalized Gradient Approximation (GGA) for the exchange-correlation (XC) energy functional indicated that the most energetically favourable ground electronic state of the LaFeO_3 bulk is a G-type antiferromagnetic insulator in agreement with experiments (Solovyev et al., 1996), with Fe spin polarization in a configuration (1 2 1 2) and a local magnetic moment of $4.1 \mu_B$ at each Fe atom (Table 4.2).

To determine the most appropriate electronic structure method for treating LaFeO_3 which has an orthorhombic unit cell, the cell parameters and interatomic bond distance and angles were characterized by performing full geometry optimization calculations from its initial crystal structure parameters of $a = 5.6266 \text{ \AA}$, $b = 5.6083 \text{ \AA}$ and $c = 7.9401 \text{ \AA}$ that came from Selbach et al., (2012). The optimized structure(s) and structural parameters are respectively shown in Figure 4.3 below and Table 4.2.





a) Without Hubbard U



b) With Hubbard U = 4.64 eV

Figure 4.3 Converged/ Optimized structures of LaFeO_3 without and with Hubbard U parameter

Table 4.2 Calculated and experimental lattice constants (a, b, c), axial and equatorial Fe-O bond lengths (r_z and r_{xy} , respectively), axial and equatorial Fe-O-Fe bond angles (α_z and α_{xy} , respectively), eigenvalue gap (E_g), Fe magnetic moment (μ_{Fe}) and cell volume for orthorhombic LaFeO₃

Property	This work			Literature		
	GGA	GGA+U U=4.3eV	GGA+U U=4.64eV	Expt	GGA	GGA+U U=4.3eV
a/ Å	5.529	5.565	5.562	5.553 ^a	5.556 ^b	5.572 ^b
b/ Å	5.638	5.664	5.673	5.563 ^a	5.653 ^b	5.627 ^b
c/ Å	7.879	7.934	7.934	7.862 ^a	7.885 ^b	7.901 ^b
r_z / Å	2.033	2.054	2.033	2.009 ^a	2.025 ^b	2.028 ^b
r_{xy} / Å	2.035	2.046	2.044	2.007 ^a	2.046 ^b	2.035 ^b
α_z / °	151.20	149.97	151.30	156.32 ^a	153.54 ^b	153.80 ^b
α_{xy} / °	152.06	151.36	152.54	157.22 ^a	153.72 ^b	154.69 ^b
E_g / eV	1.00	2.38	2.43	2.46 ^d	0.75 ^b	2.53 ^b
μ_{Fe}/μ_B	4.1	4.3	4.4	4.6±0.2 ^c	3.7 ^b	4.2 ^b
Cell vol./ Å ³	245.583	250.073	250.340	242.868 ^a	247.653 ^b	247.73 ^b

^a Marezio and Dernier, 1971; ^b Ritzmann et al., 2013; ^c Koehler and Wollan, 1957; ^d Liu et al., 2015

Table 4.2 shows a comparison between structural, electronic, and magnetic properties for antiferromagnetic LaFeO₃ calculated with GGA and GGA+U functionals. Both pure GGA and GGA+U predict a gap for LaFeO₃. However, pure GGA significantly underestimates the eigenvalue gap (1.00 eV in this study, and 0.75 eV in Ritzmann et al., (2013)) and Fe magnetic moments (4.1 μ_B in this study and 3.7 μ_B in Ritzmann et al., (2013)). These errors likely arise from the self-interaction inherent in pure density functionals for strongly correlated systems that can be ameliorated with the DFT+U approach, which accounts for the on-site Coulomb interaction in the relevant d orbitals. This is seen from the more accurate gaps and magnetic moments that the GGA+U give from the table. GGA+U theory thus provides a more satisfactory description of LaFeO₃.

Compared to GGA, GGA+U results give better lattice vectors (a, b, c) and Fe-O-Fe bond angles (axial and equatorial) but weak Fe-O (axial and equatorial) bond lengths. The GGA+U calculated and experimental lattice vectors and Fe-O-Fe bond angles are within ~ 1 % and ~ 3 % percentage error margin, indicating that there is good agreement between measured and calculated structural data. The weak Fe-O bond lengths in this LaFeO₃ model could be attributed to the distortions in the orthorhombic crystal system which had refined lattice parameters for the Pbnm space group at T = 1218 K in the work by Selbach et al., (2012).

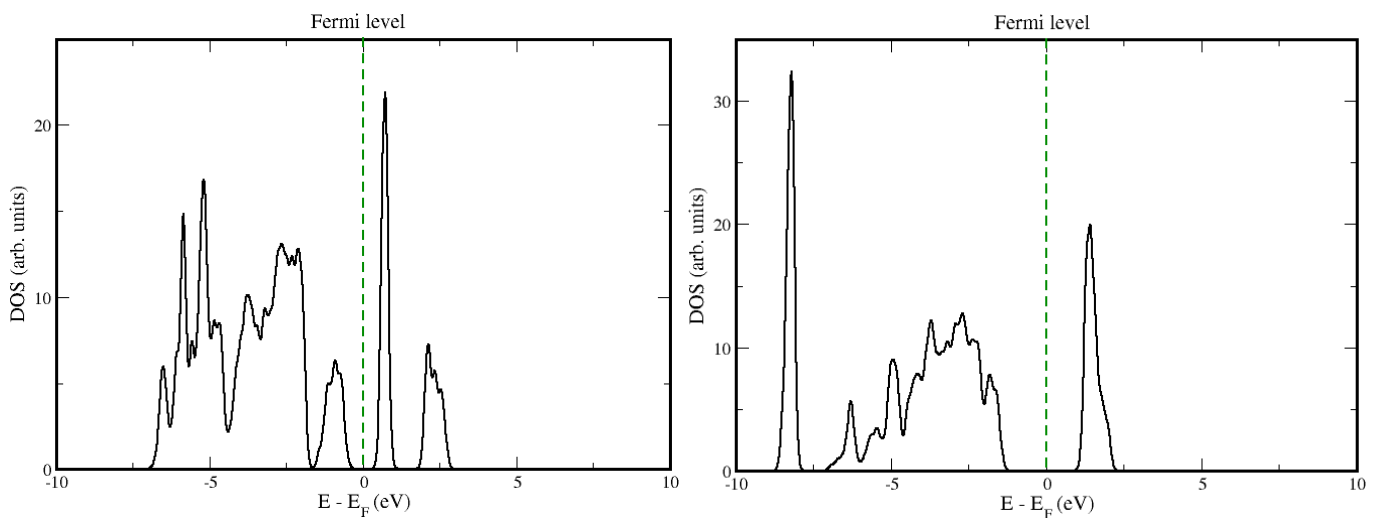
On the basis of the good correlation between theory and experiment in lattice vectors, Fe-O-Fe bond angles, eigenvalue gap and Fe magnetic moments, it is concluded that the GGA+U calculations provide the best model for LaFeO₃, and thus this level of theory is used for the rest of the bulk calculations. By comparing results obtained from the effective Hubbard U, U_{eff} value obtained in this work (4.64 eV) and that obtained by Mosey et al., (2008) (4.3 eV), it is observed that the U_{eff} = 4.3 eV underestimate the eigenvalue gap and Fe magnetic moments, hence the U_{eff} = 4.64 eV is used throughout for calculations involving GGA+U.

4.2.2 Electronic Properties of Bulk LaFeO₃

The DOS shows the number of states per interval of energy as a function of energy, while the PDOS shows the projection of total DOS onto different angular momentum components. More specifically, from the PDOS, the contribution of specific atomic orbitals to the electronic bands and the interaction between different atomic orbitals is revealed. Total density of states (DOS) and projected density of states (PDOS) of orthorhombic LaFeO₃ as shown in Figure 4.4 implies that LaFeO₃ is an insulating material due to the energy difference (eigenvalue gap) between the unoccupied band (conduction band) and the occupied band (valance band) at the Fermi energy level, E_F.

The eigenvalue/band gap is 2.43 eV and 1.00 eV (Table 4.2) respectively for DOS/ PDOS with and without Hubbard $U = 4.64$ eV. Here, the band gap, E_g was determined from the difference between highest occupied and lowest unoccupied eigenvalues at the various k-point paths and the spin up spin-polarization within the scf calculation output file. However, by reading from the Gamma point ($k = 0.0000\ 0.0000\ 0.0000$ (4585 PWs) bands) alone, the E_g was 3.032 eV and 1.624 eV respectively for DOS/ PDOS with and without Hubbard U . Nonetheless, by looking at the DOS and PDOS plots, it is observed that the E_g were 2.206 eV and 0.005 eV from the DOS plot and 2.132 eV and 0.029 eV from the PDOS plot, respectively for calculations with and without Hubbard U (4.64 eV). By comparing the E_g value from the scf output file and the DOS and PDOS plots (which only give a clue to the actual E_g of a material), it is observed that the E_g values determined from the scf output file at the various k-point paths gave values that were close to that obtained from the plots.

The GGA-PBE calculations significantly underestimated the band gap (E_g), which is 2.46 eV from experiment (Liu et al., 2015). This consistency with known experimental results validate the model and input parameters employed in this study.



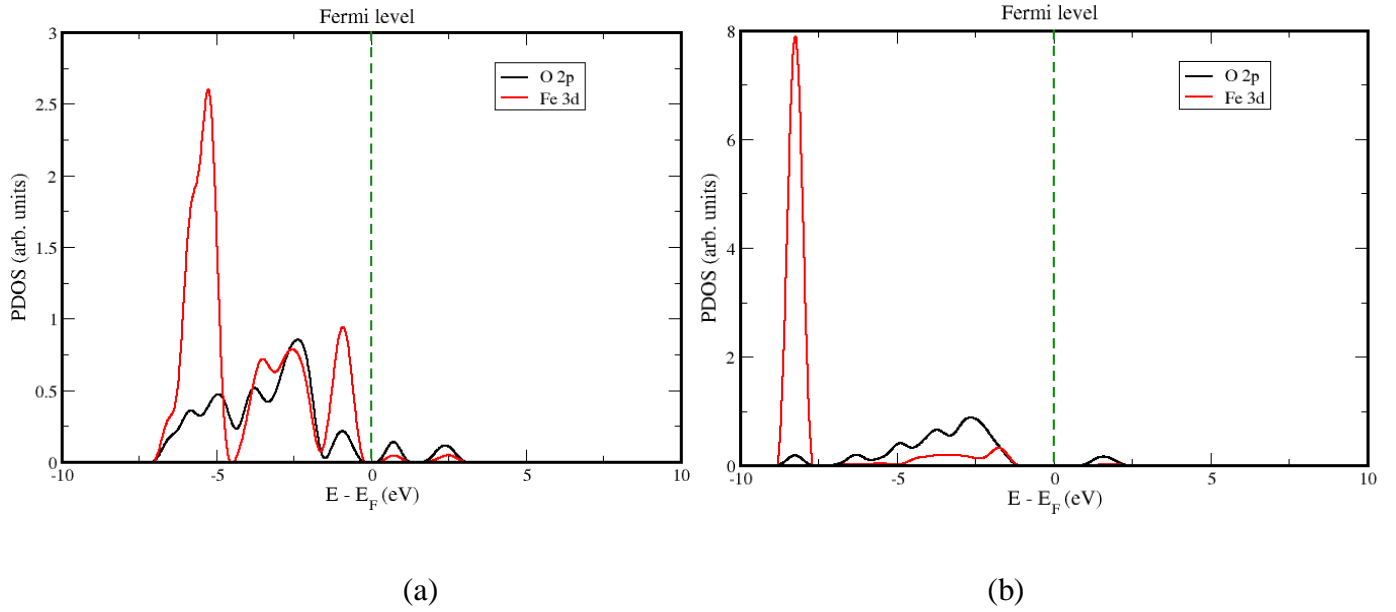


Figure 4.4 Total density of states (DOS) and projected density of states (PDOS) of orthorhombic LaFeO₃ (a) Without Hubbard U and (b) With Hubbard U = 4.64 eV

4.3 Adsorption of Hydrogen on (0 1 0) Surface of LaFeO₃

Adsorption processes involve the interaction of one or more molecules with a surface, and one of the fundamental characteristics of the process is the adsorption energy which can be measured by calorimetric techniques or can be estimated from TPD (temperature programmed desorption) measurements (McCash, 2002). To evaluate the interaction between one and two molecules of H₂ and the LaFeO₃ (0 1 0) surface in this study, their adsorption energies, E_{ads} defined below are calculated and the results are presented in Tables 4.6, 4.7 and 4.12. The adsorption energy is a criterion to determine the stability of the adsorption.

$$E_{\text{ads}} = E_{\text{substrate-adsorbate}} - (E_{\text{substrate}} + E_{\text{adsorbate}}) \quad (5)$$

where $E_{\text{substrate-adsorbate}}$ is the total/calculated electronic energy of the substrate-adsorbate system in the equilibrium state, $E_{\text{substrate}}$ and $E_{\text{adsorbate}}$ are the total electronic energies of substrate (clean surface) and adsorbate (free molecule), respectively. The $E_{\text{adsorbate}}$ (adsorbate

being H_2) is the triplet ground state energy of H_2 . By this definition, a negative value, corresponding to an exothermic process, indicates a stable adsorption and the bigger the E_{ads} is, the more stable the structure will be.

The distortion energy, E_{dist} in this studies, which represents the energy of geometry distortion of the free molecule (adsorbate) becoming distorted after adsorption on the surface/substrate is also calculated from;

$$E_{dist} = E_{\text{distorted adsorbate}} - E_{\text{adsorbate}} \quad (6)$$

where $E_{\text{distorted adsorbate}}$ and $E_{\text{adsorbate}}$ are the total electronic energies of the distorted adsorbate and adsorbate respectively. $E_{\text{adsorbate}}$ is the energy of free molecule (or atomic species in the gas phase for H atoms) whilst $E_{\text{distorted adsorbate}}$ is the energy of free adsorbate with the distorted geometry fixed to that for the adsorbed state on the surface. The results are summarized in Table 4.6.

The net charge-transfer (Q) between the H_2 molecule and the $LaFeO_3$ (0 1 0) surface is calculated using the Löwdin scheme and reported in Tables 4.11 and 4.13.

4.3.1 Bond Length of Molecular Hydrogen

The calculated bond length (structural parameter) for the gas-phase H_2 is 0.752 Å, which was obtained by putting a molecule of hydrogen in a 10 Å × 10 Å × 10 Å cubic crystal (Figure 4.5). When the model is set up, twenty-eight adsorption sites are taken in calculation when one H_2 is adsorbed at a molecular, dihydrogen and dihydride bond distance, whilst seven adsorption sites are taken in calculation when two molecules of H_2 (which approach from the gas phase) are adsorbed, as shown in Figures 4.7, 4.8, 4.11 and 4.13. H_2 molecule is put on all the sites separately parallel to the crystal surface.



Figure 4.5 Molecular hydrogen in a 10 Å x 10 Å x 10 Å box

The corresponding experimental value is 0.74 (Benson, 1965). Comparison of these two values gives a percentage change in bond length, % Δr ;

$$\% \Delta r = \left| \frac{r_{\text{exp}} - r_{\text{calc}}}{r_{\text{exp}}} \right| \times 100 \% \quad (7)$$

$$\% \Delta r = \left| \frac{0.74 - 0.752}{0.74} \right| \times 100 \% = 1.62 \%$$

According to the calculations shown above, the calculated bond length in the GGA-PBE exchange correlation functional is 1.62 % longer than the experimental bond length. This percentage change is insignificant and within the limits of hydrogen-hydrogen bond distance.

4.3.2 Why Optimal Hubbard U term was not included in Surface Calculations

Even though the inclusion of an effective Hubbard U term ($U_{\text{eff}} = 4.64$ eV in this study) is now well known to be a computational technique that corrects the significant band gap and magnetic moment of a material in local-density approximation and generalized gradient approximation calculations, as well as the inaccuracies of the most commonly used DFT functionals for strongly localized and correlated electronic ground states, yielding reasonable agreement with experimental results, in this subsequent surface calculations (hydrogen

adsorption on LaFeO₃ (0 1 0) surface), only the GGA parameterization set was used, ignoring the Hubbard U term. This is because Hamada et al., (2011) verified that electronic structures with GGA+U are qualitatively the same as those in GGA calculations. Again, in a study on LaFeO₃ by Kizaki and Kusakabe in 2012, the validity of PBE-GGA was reported. By reproducing the crystal structure of LaFeO₃ in the space group of V_h¹⁶ (Pbnm), the lowest energy solution became an insulating state with a G-type anti-ferromagnetic spin density.

4.3.3 Choice of the (0 1 0) Miller Index

In order to investigate the interaction of H₂ with the (0 1 0) LaFeO₃ surface under vacuum conditions, three of the low miller indices were chosen, i.e. (0 1 0), (1 1 0), and (1 1 1). Their surface energies were calculated and the surface with the most stable energy was chosen and used for subsequent calculations. The surface energy was calculated from the equation;

$$\gamma = \frac{E_{\text{surf}} - nE_{\text{bulk}}}{2A} \quad (8)$$

where γ represents surface energy, E_{surf} represents energy of surface created, E_{bulk} represents the energy of the bulk material, n represents thickness or more specifically a factor for number of bulk units in the surface and A represents surface area of the surface.

From the results of the surface energy as shown in Table 4.3, the following trend in stability is observed, (0 1 0) > (1 1 0) > (1 1 1).

Table 4.3 Surface energies of the various low miller indices

Surface	$E_{\text{surf}} - nE_{\text{bulk}}/\text{J}$	$2A/\text{m}^2$	Surface energy $/\text{Jm}^{-2}$
(0 1 0)	$8.68701627 \times 10^{-19}$	$1.0009009 \times 10^{-19}$	8.68
(1 1 0)	$1.10665668 \times 10^{-18}$	$1.0008940 \times 10^{-19}$	11.06
(1 1 1)	$1.31228421 \times 10^{-18}$	$1.0008997 \times 10^{-19}$	13.11

4.3.4 Clean LaFeO₃ (0 1 0) Surface

The slab model for a clean LaFeO₃ (0 1 0) surface was cleaved from the optimized bulk with GGA lattice constants, and the optimized structure is shown in Figure 4.6. It was fully relaxed under the restriction of fixed cell parameters. The (0 1 0) slab was modelled to a thickness of one in the z-direction, i.e. p (1 x 1) since the surface already contained four LaFeO₃ formula units (20 atoms) with five atomic layers in a LaOFe-O₂-FeO-LaO-LaO pattern within a vacuum region of 12 Å, so that the La-O-Fe (0 1 0) surface appeared. The atoms (and their IDs) that make up each atomic layer and termination of the ideal LaFeO₃ (0 1 0) surface is shown in Table 4.4. The surface was treated as polar and described with the slab model, where periodic boundary conditions are applied to the central super-cell and reproduced periodically throughout space. After optimization no reconstruction of the LaFeO₃ (0 1 0) surface was found though there were some lateral displacements in the x and y axis.

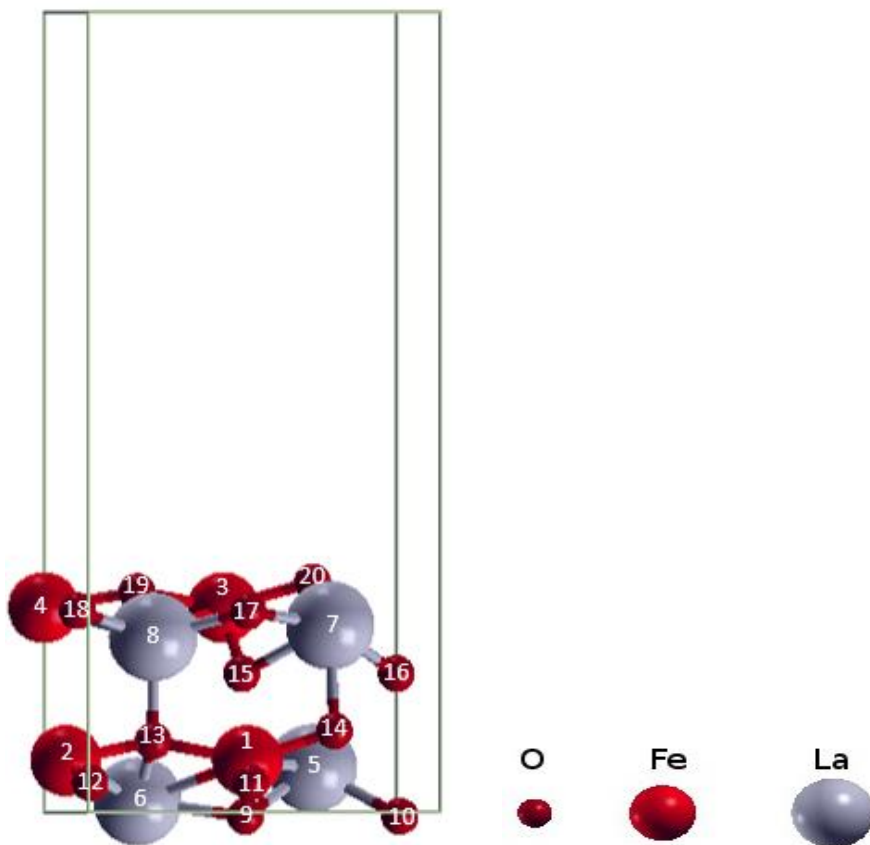


Figure 4.6 Side view of the optimized five-layer slab model of the ideal LaFeO_3 (0 1 0) surface with La-O-Fe termination

Table 4.4 Atoms (and their IDs) of the ideal LaFeO_3 (0 1 0) surface within the QE input file showing the layers they occupy and the layer's termination

Termination	Layer	Atom	ID
La-O-Fe	First	Fe	3
		Fe	4
		La	7
		La	8
		O	17
		O	18
		O	19
		O	20
O-O	Second	O	15
		O	16
Fe-O	Third	Fe	1
		Fe	2
		O	13
		O	14
La-O	Fourth	La	5
		O	11
		O	12
La-O	Fifth	La	6
		O	9
		O	10

4.3.5 Relaxation and Reconstruction of Clean LaFeO_3 (0 1 0) Surface

Surface atoms were allowed to move about their bulk position either by relaxation i.e. adjustments in the layer spacing perpendicular to the surface (movement in the z coordinate direction) or by reconstruction in the x, y coordinates. Percentage (%) relaxation is the change in interlayer spacing from the bare surfaces, where (+) indicates expansion and (-) indicates compression. Percentage (%) reconstruction is the lateral displacement of layers with a change in surface topology or surface structure periodicity, where (+) indicates displacement in the + x and + y direction and (-) indicates displacement in - x and - y directions.

$$\% \text{ Relaxation} = \frac{\text{interlayer spacing (surface)} - \text{interlayer spacing (bulk)}}{\text{interlayer spacing (bulk)}} \times 100\%$$

(9)

$$\% \text{ Reconstruction} = \frac{\text{position of surface atom} - \text{position of bulk atom}}{\text{position of bulk atom}} \times 100\%$$

(10)

For the bare LaFeO₃ (0 1 0) surface, there was no reconstruction (change in surface structure periodicity/topology), consistent with literature (Liu et al., 2009), though there were some lateral displacement, as reported in Table 4.5 below. All, except the second interlayer spacing, d₂₃ were displaced in the + x direction whilst both the second and third interlayer spacing, d₂₃ and d₃₄ were displaced in the – y direction with d₁₂ and d₄₅ (first and fourth interlayer spacing) displaced otherwise.

There was also relaxation, as shown in Table 4.5 below. Surface first and third interatomic layer spacing, d₁₂ and d₃₄ contracted towards the bulk material increasing bonding with the lower atoms. On the contrary, the second and fourth, d₂₃ and d₄₅ interlayer spacing expanded. These significant changes are in accordance to the polar character of the surface.

Table 4.5 Surface relaxation of the unreconstructed clean surface of LaFeO₃

Surface	Interlayer spacing	Relaxation/ %	Lateral displacement in x/ %	Lateral displacement in y/ %
(0 1 0)	d ₁₂	- 43.28	9.10	19.26
	d ₂₃	16.62	- 33.87	- 67.87
	d ₃₄	- 58.34	7.91	- 35.34
	d ₄₅	57.14	10.37	1.61

4.3.6 The Adsorption Mechanism of one H₂ on LaFeO₃ (0 1 0) Surface

All the possible adsorption configurations on the LaFeO₃ (0 1 0) surface were considered and chosen to simulate one H₂ adsorption at a molecular, dihydrogen and dihydride bond distance. The H₂ was attached at molecular, dihydrogen and dihydride bond distances of 0.740 Å, ~ 0.8 Å and ~ 1.7 Å respectively, in accord with what Kubas, (2007) speculated from neutron diffraction studies for the oxidative addition of H₂ to a metal after the H₂ was structurally isolated in a series of interactions. The configurations of initial and final adsorption are depicted in Figure 4.7 for some of the sites that gave product(s) when hydrogen was adsorbed. These same kind of product(s) were formed at the other sites which also gave product(s). Table 4.6 summarizes the adsorption energies, distortion energies and product(s) at the favourable adsorption sites when hydrogen was adsorbed at molecular, dihydrogen and dihydride bond distances. Their calculated initial and final structural parameters are also given in Tables 4.8, 4.9 and 4.10 respectively for molecular, dihydrogen and dihydride hydrogen bond distances.

All the adsorption studies except that at *La7-Fe3 bridge* site where the hydrogen atoms were at a dihydride bond distance apart (Table 4.7) had negative E_{ads} which correspond to exothermic processes indicating stable, favourable and spontaneous adsorption. Adsorption sites like *O17-top side-on, O18-top side-on, O19-top side-on, O20-top side-on, Fe3-top end-on, Fe3-top side-on, Fe4-top end-on, Fe4-top side-on, La7-top end-on, La7-top side-on, La8-top end-on, La8-top side-on, La7-O17 bridge, La7-O20 bridge, La7-Fe3 bridge, La8-O17 bridge, La8-O18 bridge, La8-Fe3 bridge* and *La8-La7 bridge* did not lead to any product as the H₂ detached from the LaFeO₃ (0 1 0) surface. These sites are non-preferential for H₂ adsorption on LaFeO₃ (0 1 0) surface. This H₂ which evolved from the surface is as a result of the fact that the strength of the M - H bond (M= LaFeO₃ in this study) in the metal hydride, which is crucial to the operation of the Ni-MH battery was too low (less than the

ideal bond enthalpy range of 0.260 - 0.521 eV (Atkins et al., 2010)) making the hydrogen not to react with the LaFeO_3 (0 1 0) surface.

The adsorption product(s) were the same at the various adsorption sites for the case where hydrogen atoms were at molecular and dihydrogen bond distances apart. Their adsorption energies were essentially the same except at the *O19-top end-on* site where H_2O left the surface to create an oxygen vacancy in the crystal lattice of the LaFeO_3 (0 1 0) surface. The adsorption processes yielded $-\text{LaOH}$ and $-\text{FeH}$ at the *O17-top end-on* (molecular and dihydrogen H-H bond distances), *O18-top end-on* (molecular and dihydrogen H-H bond distances) and *Fe3-O20 bridge* (molecular, dihydrogen and dihydride H-H bond distances) sites, H_2O at the *O17-top end-on* (dihydride H-H bond distance), *O19-top end-on* (molecular, dihydrogen and dihydride H-H bond distances) and *O20-top end-on* (dihydride H-H bond distance), $-\text{Fe}(\mu\text{OH})\text{La}$ and $-\text{FeH}$ at the *Fe3-O19 bridge* (molecular, dihydrogen and dihydride H-H bond distances), *Fe4-O19 bridge* (molecular, dihydrogen and dihydride H-H bond distances), *La8-O19 bridge* (dihydride H-H bond distance) and *La8-Fe4 bridge* (dihydride H-H bond distance) sites. Fe and La dihydrogen and dihydride bonds did not form on LaFeO_3 (0 1 0) surface and also no hydrogen was adsorbed on the La atom. Similar adsorption sites do not necessarily give the same products on addition of H_2 . Even though some Fe-O bridge sites give $-\text{Fe}(\mu\text{OH})\text{La}$ and $-\text{FeH}$ others give LaOH and FeH . At the O top end-on sites while some give LaOH and FeH others give H_2O or FeOH depending on the H-H distances.

The LaFeO_3 (0 1 0) surface re-orientates itself after structural optimization (adsorption) as the atoms rearrange themselves not just at the first layer but also beyond. Bonds break and form beyond the top layer with their magnitudes shown in Tables 4.8, 4.9 and 4.10 respectively for molecular, dihydrogen and dihydride hydrogen bond distances. The H_2O which forms when

H₂ attaches to O atom at a molecular, dihydrogen and dihydride bond distance leaves the surface to create an oxygen vacancy at the *O17-top end-on*, *O19-top end-on* and *O20-top end-on* sites. Nonetheless, it is only at the O17 site which has a coordination number of two with the O connecting only two La atoms, and in the dihydride end-on configuration that another O atom attempts to fill-in the gap in a vacancy hopping oxygen transport. The oxygen vacancy which forms when H₂O leaves the surface makes LaFeO₃ a potential catalyst for applications such as methanol production.

At the reaction site of this *O17-top end-on* dihydride configuration, La7-O17 and La8-O17 bonds break and H21-O17-H22 leaves the surface to create a hole in the form of H₂O with an H-O-H bond angle of 105.72 ° which is similar to that in H₂O (109.5 °). This angle was initially 110.26 ° in H21-O17-H22. In the process, Fe3-O20 and La7-Fe3 bonds break and the O20 which was initially 0.308 Å in the x direction reverses (increase to 4.772 Å) to fill the created hole even though it does not bond to the La8. The La5-O10 bond also breaks and the O10 now goes to bridge Fe2 and La6. Fe1-O13 bond breaks and Fe1-O15, La8-O15, La6-O10, Fe2-O10 and La5-O14 bonds also form. The magnitude of bond changes is outlined in Table 4.10.

Adsorption energy calculations predicted that the *Fe3-O20 bridge* site was the most favourable adsorption site for hydrogen adsorption (at molecular, dihydrogen and dihydride hydrogen bond distances apart) on (0 1 0) surface of LaFeO₃ forming -LaOH and -FeH, with E_{ads} in the range -1.322 to -1.324 eV. However, for LaFeO₃ (0 1 0) purpose as an anodic material in Ni-MH batteries, the E_{ads} (bond enthalpy) were too high (more than the ideal bond enthalpy range of 0.260 - 0.521 eV (Atkins et al., 2010)) at the *Fe3-O20 bridge* site and as such will not make the overall reaction in the Ni-MH battery to be reversible. M (LaFeO₃ in this study) is supposed to possess high hydrogen capacity and moderate hydride stability in

Ni-MH battery applications. Hence, the *Fe3-O19 bridge* site was chosen as the favourable site for the hydrogen adsorption studies (hydrogen atoms being at molecular, dihydrogen and dihydride bond distances apart) forming $-\text{Fe}(\mu\text{OH})\text{La}$ and $-\text{FeH}$ with E_{ads} in the range -0.455 to -0.456 eV. At this *Fe3-O19 bridge* site, the Fe coordinates to three O atoms and two La atoms at an average Fe-O bond length of 1.998 \AA , an average La-Fe bond length of 3.248 \AA and an O-Fe-O bond angle of 90.22° and the O also coordinates to 2 Fe atoms at an average Fe-O bond length of 2.081 \AA and an Fe-O-Fe bond angle of 148.73° . Here, the molecular hydrogen configuration (Table 4.6) gave the most stable adsorption energy.

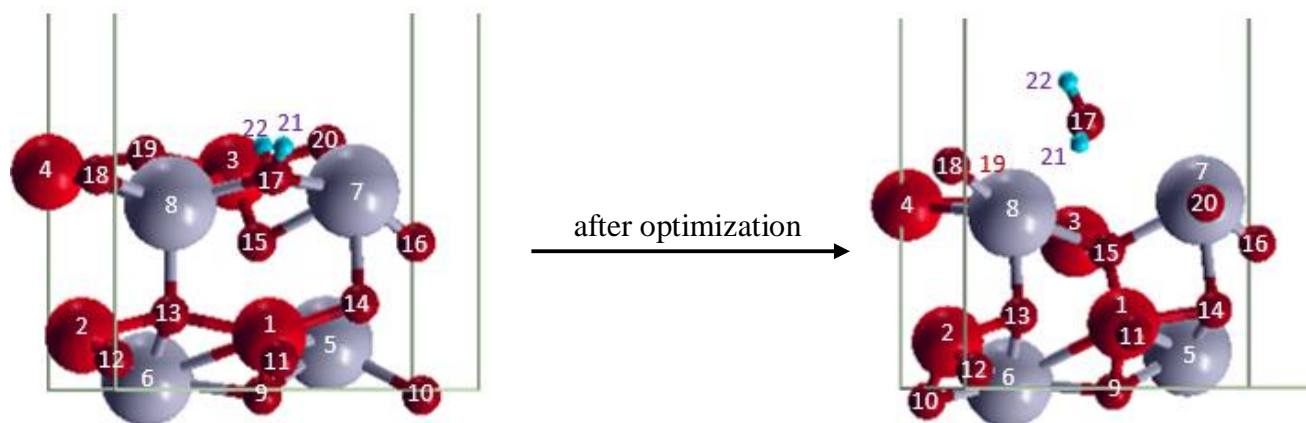
When H_2 is put both *end-on* and *side-on* on surface Fe and La atoms in a molecular, dihydrogen and dihydride bond distance, it is realized that the H atoms do not bond onto those surface atoms after optimization. However, when put *end-on* at a molecular and dihydride bond distance on surface O, the H atoms bond onto the O atom after optimization. This indicates that among the surface atoms, O is the one that has a greater affinity for H_2 . Because of this tendency by surface O atom, in the molecular H_2 adsorption at *Fe3-O19 bridge* site (most preferred site), it can be concluded that it is the O atom that facilitates the breaking of the H-H bond before other surface atoms like Fe can adsorb an atomic hydrogen.

At this *Fe3-O19 bridge* site where hydrogen atoms are at a molecular bond distance apart, La8-Fe4, La8-Fe3, Fe3-O19 and H21-H22 bonds break whilst La8-O15 bond forms leading to the products $-\text{Fe}(\mu\text{O19H21})\text{La8}-$ and $-\text{Fe3H22}$ with the $-\text{O19H21}$ acting as a bridging ligand. Beyond the topmost layer, La5-Fe1 bond breaks whilst La5-O16 bond forms. Overall, La-Fe bonds break at the topmost layer whilst La-O bonds form beyond the topmost layer. The magnitude of bond changes is outlined in Table 4.8.

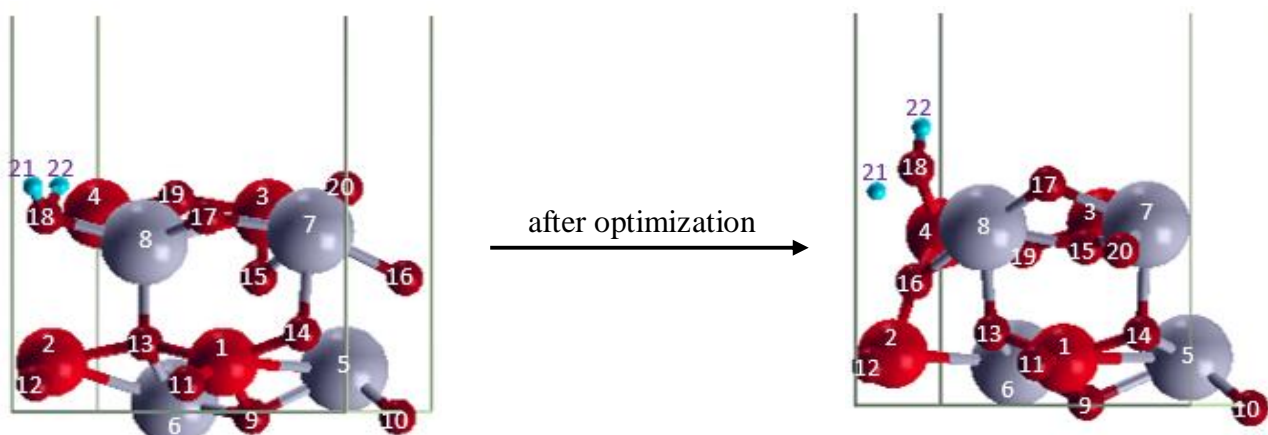
With the question of whether *end-on* or *side-on* adsorption is more preferred thermodynamically at a particular adsorption site, it is observed from the E_{ads} in Table 4.7

that the *end-on* configuration is more stable and thus preferred than the *side-on* at the *O-top*, *Fe3-top* and *La7-top* sites in all three forms of hydrogen, but otherwise at the *Fe4-top* and *La8-top* sites. At the *Fe4-top* site, the *end-on* is preferred in the dihydrogen and dihydride case but otherwise in the molecular case. Again, at the *La8-top* site, the *side-on* is more preferred in the molecular and dihydrogen case, but otherwise in the dihydride case.

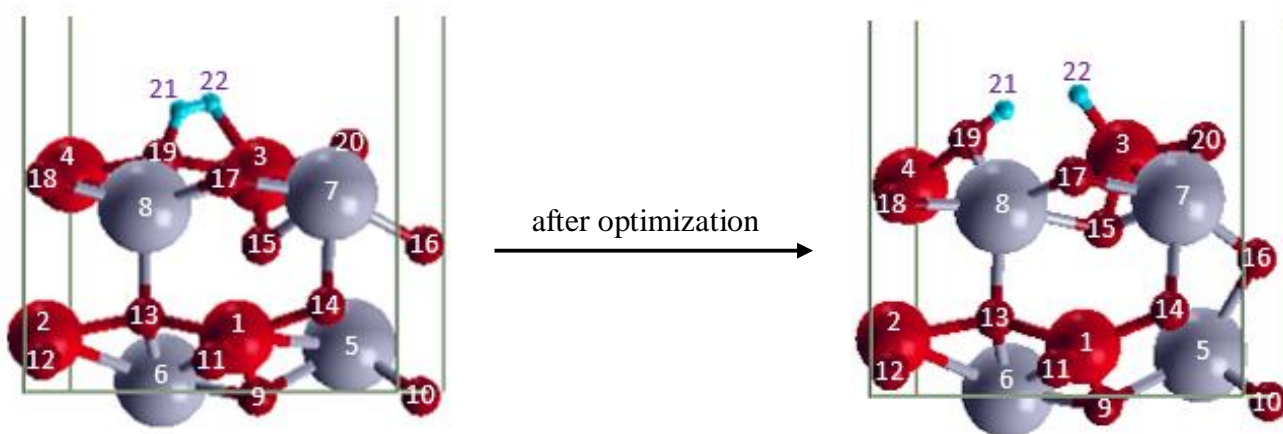
O17-top end-on dihydride



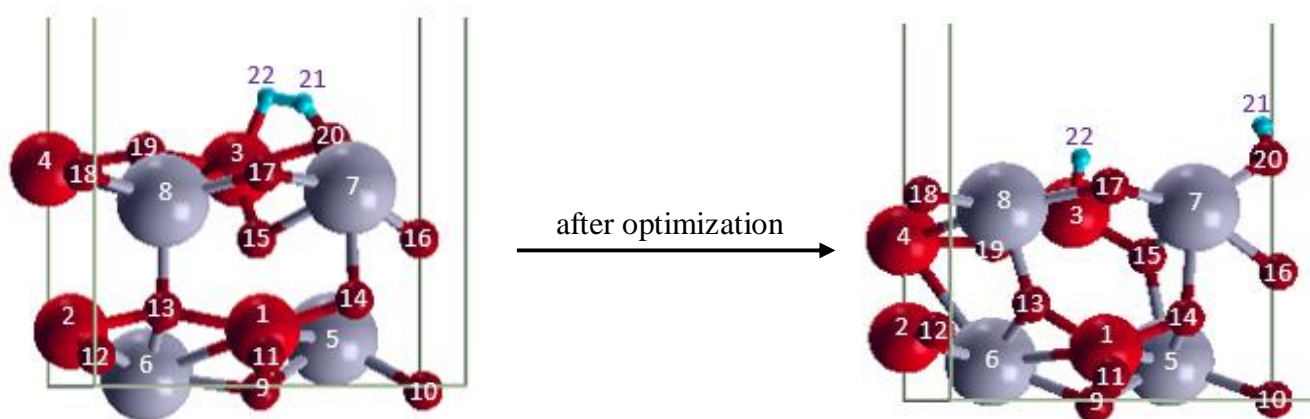
O18-top end-on dihydride



Fe3-O19 bridge molecular



Fe3-O20 bridge dihydrogen



(a) Initial guess structure

(b) Optimized structure



Figure 4.7 Side views of the initial and optimized structures of all the different kind of products that form at selected favourable adsorption sites

Table 4.6 Calculated E_{ads} and product(s) at the favourable adsorption sites

Adsorption site	Molecular			Dihydrogen			Dihydride	
	$E_{\text{ads}} / \text{eV}$	$E_{\text{dist}} / \text{eV}$	Product(s)	$E_{\text{ads}} / \text{eV}$	$E_{\text{dist}} / \text{eV}$	Product(s)	$E_{\text{ads}} / \text{eV}$	Product(s)
<i>O17-top end-on</i>	- 0.232	-0.00017	LaOH and FeH	- 0.236	-0.00016	LaOH and FeH	- 0.509	H ₂ O
<i>O18-top end-on</i>	- 0.235	-0.00018	LaOH and FeH	- 0.238	-0.00016	LaOH and FeH	- 0.487	FeOH
<i>O19-top end-on</i>	- 0.218	-0.00032	H ₂ O	- 0.174	-0.00031	H ₂ O	- 0.331	H ₂ O
<i>O20-top end-on</i>	- 0.053	-	-	- 0.056	-	-	- 0.612	H ₂ O
<i>Fe3-O19 bridge</i>	- 0.456	0.000207	Fe(μ OH)La and FeH	- 0.456	0.000187	Fe(μ OH)La and FeH	- 0.455	Fe(μ OH)La and FeH
<i>Fe3-O20 bridge</i>	- 1.323	1.16E-05	LaOH and FeH	- 1.322	0.000134	LaOH and FeH	- 1.324	LaOH and FeH
<i>Fe4-O19 bridge</i>	- 0.455	0.000214	Fe(μ OH)La and FeH	- 0.455	0.00019	Fe(μ OH)La and FeH	- 0.455	Fe(μ OH)La and FeH
<i>La8-O19 bridge</i>	- 0.039	-	-	- 0.039	-	-	- 0.457	Fe(μ OH)La and FeH
<i>La8-Fe4 bridge</i>	- 0.028	-	-	- 0.025	-	-	- 0.697	Fe(μ OH)La and FeH

Table 4.7 Calculated E_{ads} and product(s) at the other adsorption sites

Adsorption site	Molecular		Dihydrogen		Dihydride	
	$E_{\text{ads}} / \text{eV}$	Product(s)	$E_{\text{ads}} / \text{eV}$	Product(s)	$E_{\text{ads}} / \text{eV}$	Product(s)
<i>O17-top side-on</i>	- 0.026	-	- 0.028	-	- 0.024	-
<i>O18-top side-on</i>	- 0.026	-	- 0.027	-	- 0.026	-
<i>O19-top side-on</i>	- 0.030	-	- 0.030	-	- 0.030	-
<i>O20-top side-on</i>	- 0.034	-	- 0.031	-	- 0.033	-
<i>Fe3-top end-on</i>	- 0.012	-	- 0.011	-	- 0.027	-
<i>Fe3-top side-on</i>	- 0.012	-	- 0.011	-	- 0.015	-
<i>Fe4-top end-on</i>	- 0.012	-	- 0.012	-	- 0.029	-
<i>Fe4-top side-on</i>	- 0.015	-	- 0.011	-	- 0.015	-
<i>La7-top end-on</i>	- 0.059	-	- 0.059	-	- 0.062	-
<i>La7-top side-on</i>	- 0.012	-	- 0.012	-	- 0.062	-
<i>La8-top end-on</i>	- 0.039	-	- 0.039	-	- 0.046	-
<i>La8-top side-on</i>	- 0.046	-	- 0.047	-	- 0.045	-
<i>La7-O17 bridge</i>	- 0.034	-	- 0.034	-	- 0.046	-
<i>La7-O20 bridge</i>	- 0.055	-	- 0.051	-	- 0.052	-
<i>La7-Fe3 bridge</i>	- 0.026	-	- 0.023	-	0.018	-
<i>La8-O17 bridge</i>	- 0.030	-	- 0.031	-	- 0.038	-
<i>La8-O18 bridge</i>	- 0.029	-	- 0.029	-	- 0.037	-
<i>La8-Fe3 bridge</i>	- 0.032	-	- 0.031	-	- 0.021	-
<i>La8-La7 bridge</i>	- 0.029	-	- 0.030	-	- 0.026	-

Table 4.8 Calculated structural parameters at the favourable adsorption sites when hydrogen atoms are at a molecular distance apart

Environment	<i>O17-top end-on</i>		<i>O18-top end-on</i>		<i>O19-top end-on</i>		<i>Fe3-O19 bridge</i>		<i>Fe4-O19 bridge</i>		<i>O20-Fe3 bridge</i>	
	Initial/Å	Final/Å										
H21-H22	0.740	2.443	0.740	2.585	0.740	1.554	0.740	1.634	0.740	1.642	0.740	4.075
O17-H21	1.068	3.210										
O17-H22	1.065	0.982										
O18-H21			1.070	3.335								
O18-H22			1.062	0.981								
O19-H21					1.065	0.978			1.105	0.995		
O19-H22					1.068	0.986						
O20-H21											1.000	0.975
Fe3-H21	4.179	1.665										
Fe3-H22											1.653	1.709
Fe4-H22									1.781	1.674		
Fe1-O14			2.027	3.202								
Fe1-O17			3.387	2.037								
Fe2-O13											2.126	2.879
Fe2-O18	3.389	2.045										
Fe3-O15	1.868	1.844										
Fe3-O17	3.701	3.918										
Fe3-O19	2.080	3.891			2.080	3.256	2.080	3.266				
Fe3-O20	2.047	5.150	2.047	5.309							2.047	4.340
Fe4-O18	3.701	3.894										
Fe4-O19	2.081	1.828	2.081	3.933	2.081	3.564			2.081	3.278		
La5-O14	2.865	3.792									2.865	2.568
La5-O15			2.822	2.233					2.822	2.447	2.822	2.372
La5-O16	2.824	2.240					2.824	2.441				

Table 4.8 Cont'd

Environment	<i>O17-top end-on</i>		<i>O18-top end-on</i>		<i>O19-top end-on</i>		<i>Fe3-O19 bridge</i>		<i>Fe4-O19 bridge</i>		<i>O20-Fe3 bridge</i>	
	Initial/Å	Final/Å										
La7-O17	2.351	3.034										
La8-O15	2.712	2.314					2.712	2.419				
La8-O17	2.330	2.475										
La8-O18	2.329	1.665										
La8-O19					2.280	2.749					2.280	2.707
La5-Fe1			3.224	3.657			3.224	3.328				
La6-Fe4											4.745	3.291
La7-Fe3	3.232	3.383									3.232	3.402
La8-Fe3	3.263	3.709			3.263	3.507	3.263	3.470	3.263	3.520	3.263	3.426
La8-Fe4	3.263	3.530	3.263	3.733	3.263	3.460	3.263	3.529	3.263	3.465		

Results for bond breakage are indicated in bold whereas those for its formation are left not bolded.

Table 4.9 Calculated structural parameters at the favourable adsorption sites when hydrogen atoms are at a dihydrogen distance apart

Environment	<i>O17-top end-on</i>		<i>O18-top end-on</i>		<i>O19-top end-on</i>		<i>Fe3-O19 bridge</i>		<i>Fe4-O19 bridge</i>		<i>Fe3-O20 bridge</i>	
	Initial/Å	Final/Å										
H21-H22	0.795	2.509	0.797	2.499	0.796	1.572	0.796	1.634	0.795	1.651	0.798	4.080
O17-H21	1.075	3.263										
O17-H22	1.078	0.981										
O18-H21			1.078	3.252								
O18-H22			1.075	0.981								
O19-H21					1.109	0.976	1.066	0.995	1.151	0.994		
O19-H22					1.049	0.983						
O20-H21											1.000	0.975
Fe3-H21	4.198	1.662										
Fe3-H22	3.427	3.501					1.797	1.675			1.627	1.706
Fe4-H21			4.206	1.661								
Fe4-H22			3.434	3.496					1.696	1.675		
Fe1-O14			2.027	3.227								
Fe1-O17			3.387	2.043								
Fe2-O13											2.126	2.891
Fe2-O18	3.389	2.041										
Fe3-O19	2.080	3.782			2.080	3.280	2.080	3.267				
Fe3-O20	2.047	5.149	2.047	5.329							2.047	4.342
Fe4-O19			2.081	3.750	2.081	3.264			2.081	3.286		
La5-O14											2.865	2.566
La5-O15			2.822	2.248					2.822	2.453	2.822	2.375
La5-O16	2.824	2.248					2.824	2.443				
La7-O17	2.351	3.001										
La7-O20									2.411	2.606		

Table 4.9 Cont'd

Environment	<i>O17-top end-on</i>		<i>O18-top end-on</i>		<i>O19-top end-on</i>		<i>Fe3-O19 bridge</i>		<i>Fe4-O19 bridge</i>		<i>Fe3-O20 bridge</i>	
	Initial/Å	Final/Å										
La8-O15	2.712	2.318					2.712	2.420				
La8-O19					2.280	2.719					2.280	2.719
La5-Fe1	3.224	3.627	3.224	3.621			3.224	3.327				
La6-Fe4											4.745	3.292
La7-Fe3	3.232	3.413	3.232	3.381							3.232	3.402
La8-Fe3	3.263	3.696	3.263	3.505	3.263	3.469	3.263	3.468	3.263	3.512	3.263	3.426
La8-Fe4	3.263	3.514	3.263	3.690	3.263	3.480	3.263	3.528	3.263	3.458		

Results for bond breakage are indicated in bold whereas those for its formation are left not bolded.

Table 4.10 Calculated structural parameters at the favourable adsorption sites when hydrogen atoms are at a dihydride distance apart

Environment	<i>O17-top end-on</i>		<i>O18-top end-on</i>		<i>O19-top end-on</i>		<i>O20-top end-on</i>		<i>La8-Fe4 bridge</i>		<i>La8-O19 bridge</i>		<i>Fe3-O19 bridge</i>		<i>Fe3-O20 bridge</i>		<i>Fe4-O19 bridge</i>	
	Initial /Å	Final /Å																
H21-H22	1.722	1.595	1.722	3.257	1.721	1.558	1.721	1.563	1.721	2.881	1.722	1.793	1.721	1.636	1.721	4.069	1.721	1.628
O17-H21	1.045	1.025																
O17-H22	1.054	0.975																
O18-H21			1.065	2.688														
O18-H22			1.156	0.976														
O19-H21					1.158	0.988					0.922	0.984	1.012	0.995			1.005	0.995
O19-H22					1.137	0.990			1.490	0.976								
O20-H21							1.150	0.979							1.044	0.975		
O20-H22							1.155	0.975										
Fe3-H22													1.512	1.675	1.501	1.710		
Fe4-H21									1.837	1.648								
Fe4-H22											2.971	1.676					1.520	1.674
La8-H22									2.140	3.108	1.655	2.897						
Fe1-O13	2.126	2.268																
Fe1-O14									2.027	2.969								
Fe1-O15	2.621	2.088																
Fe1-O17									3.387	2.040								
Fe2-O10	7.901	1.860																
Fe2-O13			2.126	2.350											2.126	2.863		
Fe2-O16			8.123	1.959														
Fe3-O19					2.080	3.222							2.080	3.276				
Fe3-O20	2.047	5.406	2.047	5.825			2.047	3.684	2.047	5.328					2.047	4.341		
Fe4-O16			7.889	1.983														
Fe4-O18			3.701	2.178														
Fe4-O19					2.081	3.207			2.081	3.696	2.081	3.401					2.081	3.274

Table 4.10 Cont'd

Environment	<i>O17-top end-on</i>		<i>O18-top end-on</i>		<i>O19-top end-on</i>		<i>O20-top end-on</i>		<i>La8-Fe4 bridge</i>		<i>La8-O19 bridge</i>		<i>Fe3-O19 bridge</i>		<i>Fe3-O20 bridge</i>		<i>Fe4-O19 bridge</i>	
	Initial /Å	Final /Å																
La5-O10	2.393	6.380							2.393	2.677								
La5-O14	2.865	2.438	2.865	2.514					2.865	2.412					2.865	2.566		
La5-O15							2.822	2.578	2.822	2.345	2.822	2.501			2.822	2.374	2.822	2.451
La5-O16							2.824	2.601					2.824	2.451				
La6-O10	5.777	2.414																
La7-O16			2.464	6.136														
La7-O17	2.351	3.394							2.351	2.633								
La7-O20							2.411	2.741			2.411	2.681						
La8-O15	2.712	2.427	2.712	2.354									2.712	2.431				
La8-O16			5.876	2.588														
La8-O18			2.329	2.619														
La8-O19			2.280	3.075	2.280	2.705									2.280	2.695		
La5-Fe1							3.224	3.351	3.224	3.426			3.224	3.319				
La6-Fe1							3.271	3.318	3.271	3.338								
La6-Fe2							3.271	3.317										
La6-Fe4															4.745	3.288		
La7-Fe3	3.232	3.648	3.232	3.645			3.232	3.609	3.232	3.378					3.232	3.399		
La8-Fe3			3.263	3.381	3.263	3.485	3.263	3.343	3.263	3.585	3.263	3.467	3.263	3.457	3.263	3.423	3.263	3.524
La8-Fe4			3.263	3.375	3.263	3.487	3.263	3.325	3.263	3.667	3.263	3.365	3.263	3.523			3.263	3.461

Results for bond breakage are indicated in bold whereas those for its formation are left not bolded.

4.3.7 Analysis of the Projected and Total Density of States Plots for H₂ adsorption on LaFeO₃ (0 1 0) Surface

In order to evaluate the effect of H₂ adsorption on the electronic structures of the LaFeO₃ (0 1 0) surface, the projected density of states (PDOS) of hydrogen, oxygen, iron and lanthanum atoms at the first surface layer, and the total density of states (TDOS) of LaFeO₃ (0 1 0) surface before and after adsorption in the most stable adsorption site (*Fe3-O19 bridge*) is plotted and compared with those of the clean surface and hydrogen molecule in the vacuum region far from the surface. By analysing the change of valance states and energies, the information of interaction between the atoms is obtained. The adsorption structures at the *Fe3-O19 bridge* site is labelled at the first and second surface layers to aid in this analysis, and is shown in Figure 4.8 below.

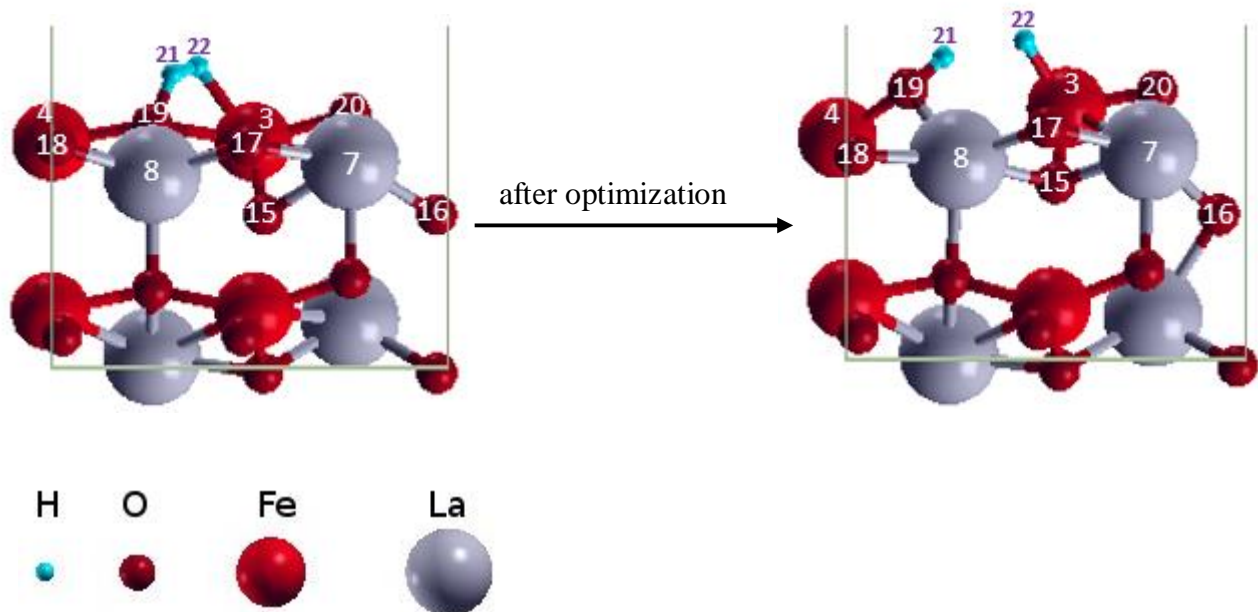


Figure 4.8 Side view of initial and optimized structures at *Fe3-O19 bridge* site

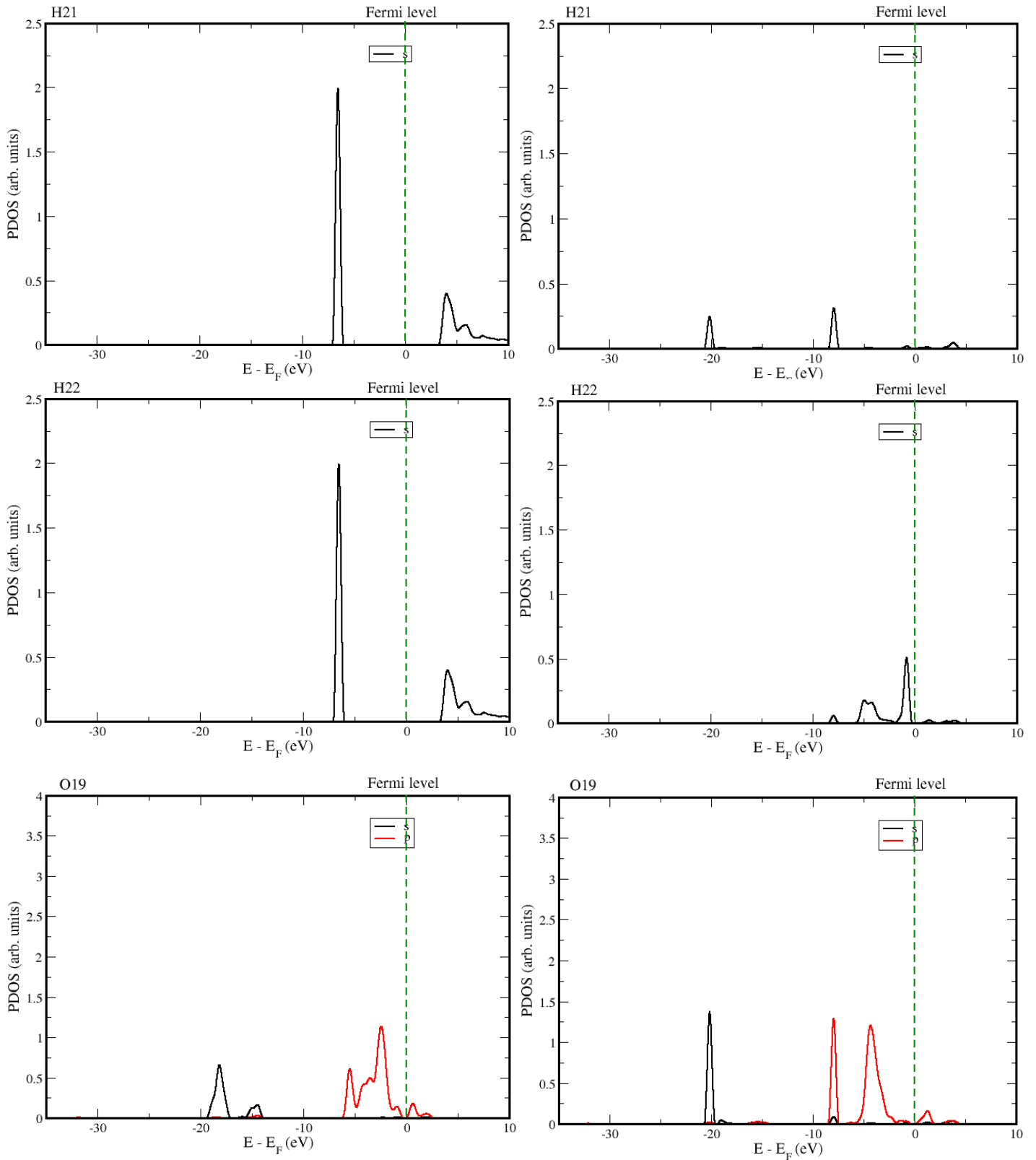
Figure 4.9 presents the PDOS and TDOS of H₂ molecule adsorption on the LaFeO₃ (0 1 0) surface at *Fe3-O19 bridge* adsorption site. These plots help in analysing the changes of electronic state before and after adsorption, respectively on the LaFeO₃ (0 1 0) surface. When

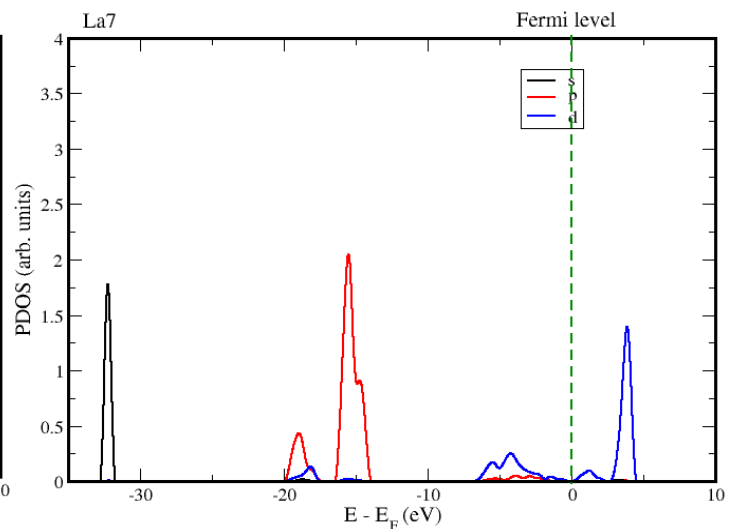
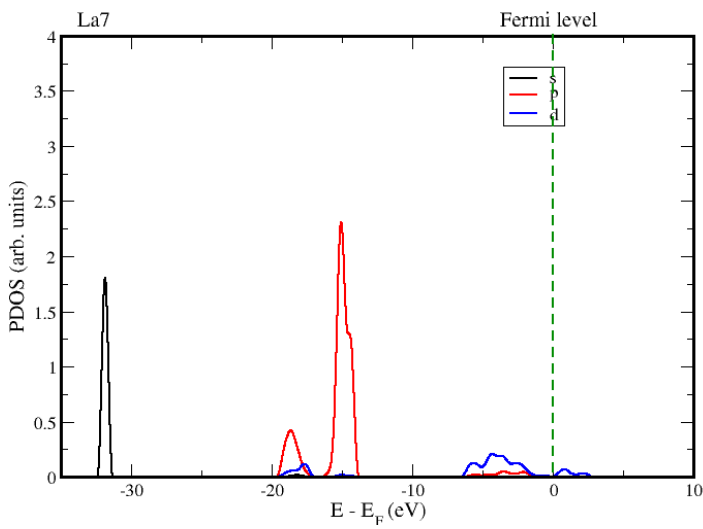
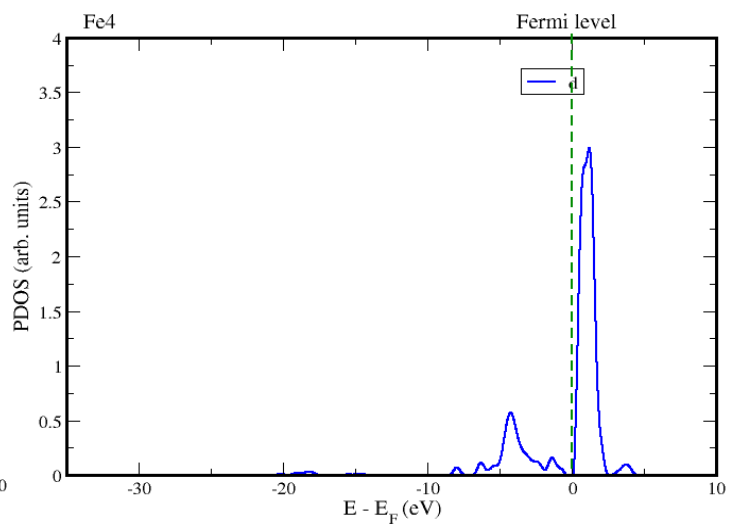
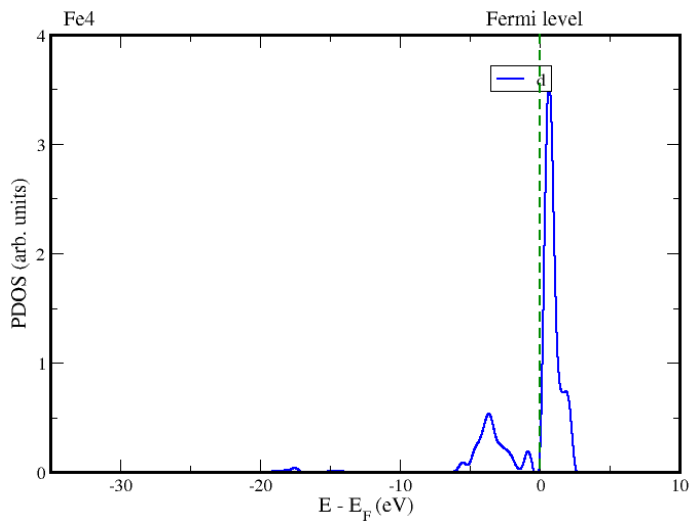
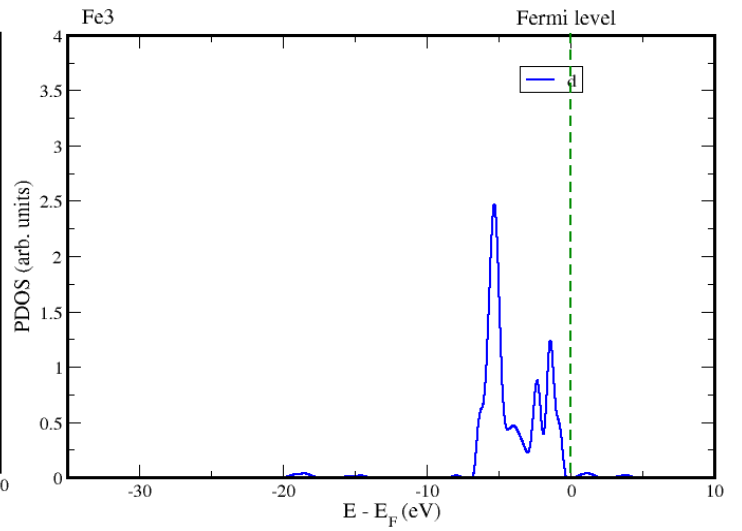
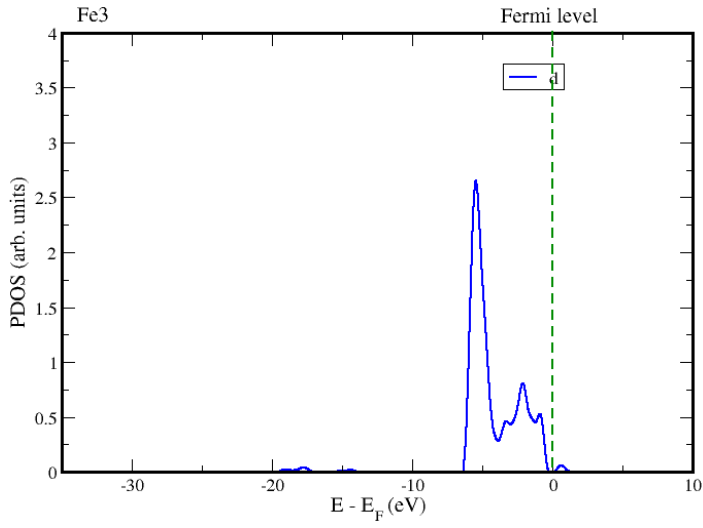
the H₂ molecule (H21 and H22 atoms) is far from LaFeO₃ (0 1 0) surface, there is a sharp and a bit of broad peak attributed to a bonding molecular orbital of H₂ at around - 6 eV and 5 eV. After adsorption and dissociation into H atoms, the s- orbital peaks of H21 and H22 shift down to the conduction band with their peak heights being modified. Some minor peaks were also formed. This is due to hybridization with s and p orbitals of O19, and d orbitals of Fe3 after the adsorption, respectively near the Fermi level. These overlapping of orbitals between the two H atoms (H21 and H22), and O19 and Fe3 is because they form molecular orbitals which implies strong interaction between them.

The peaks of projected density of states of H atoms fall after adsorption, which means the energy of the surface is lower and the structure is more stable after adsorption. After adsorption, the PDOS of H, O, Fe and La atoms changed meaning their charge populations also changed, as seen in Table 4.11. These changes in PDOS profiles helps in understanding the chemical bonding pattern involved in the adsorption process. There were very significant changes in the PDOS profiles of H21, H22, O19, Fe3, La7 and La8 atoms due to the chemical interaction among their atomic orbitals.

From the total density of states (TDOS) profiles of the pure and H₂ adsorbed LaFeO₃ (0 1 0) surfaces, two new peaks were found to appear after the adsorption at around - 20 and - 8 eV. Again, the energy gap between the highest occupied and lowest unoccupied eigenvalues, as well as the magnetic moments of the surface Fe atoms were found to increase from 0.6967 eV to 0.9889 eV, and 4.550 μ_B to 4.605 μ_B respectively after the adsorption. These observational changes were as a result of the chemical interaction between O19-H21 and Fe3-H22 when H₂ was adsorbed on the LaFeO₃ (0 1 0) surface.

In conclusion, the interaction between H₂ molecule and LaFeO₃ (0 1 0) surface at the *Fe3-O19 bridge* adsorption site was mainly due to the overlapping of H 1s, O 2s and O 2p states, Fe 3d state, and La 5p and 5d states.





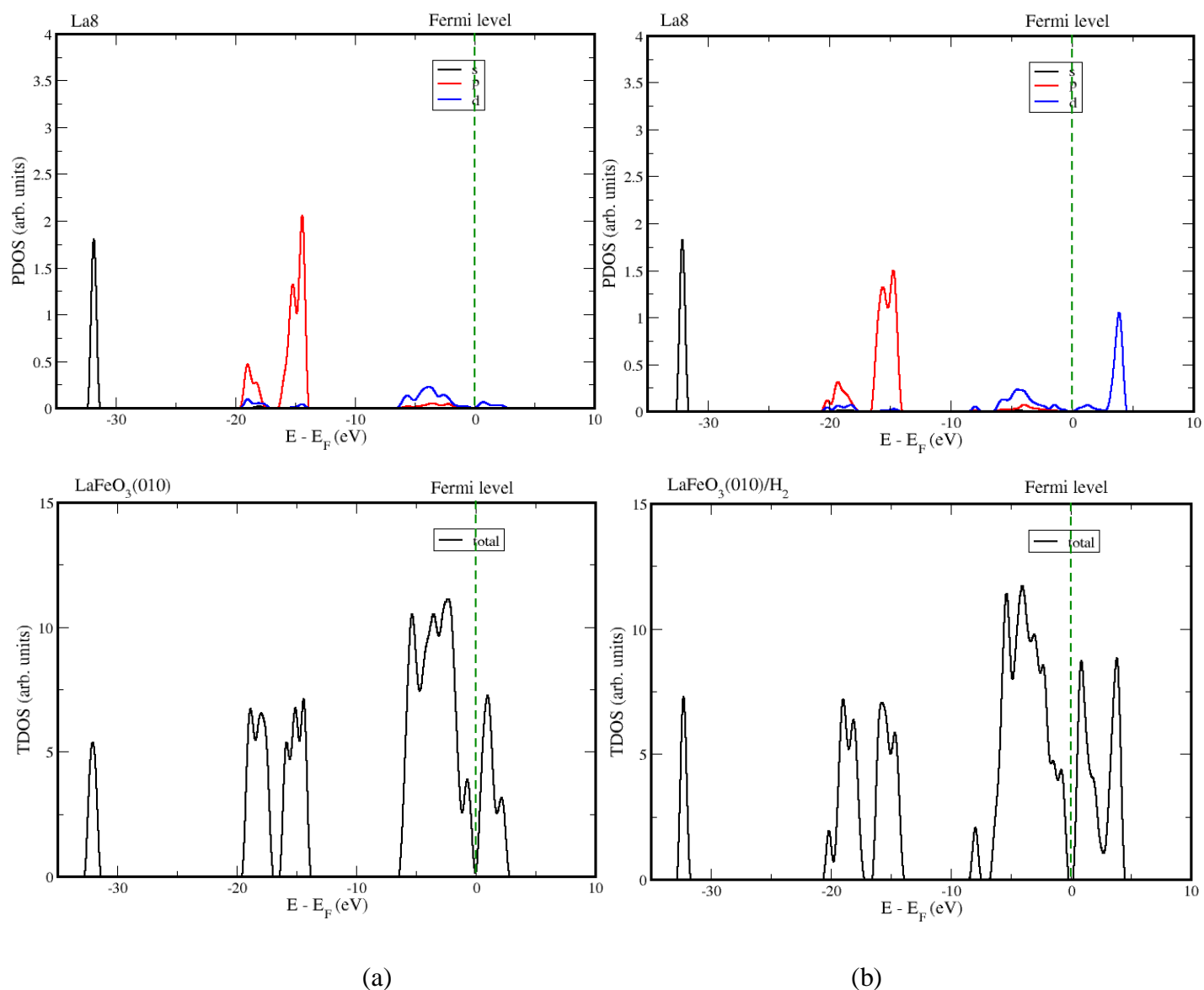


Figure 4.9 PDOS and TDOS on *Fe3-O19* bridge site at molecular hydrogen bond distance (a) before adsorption and (b) after adsorption

4.3.8 Analysis of the Löwdin Charge Population on LaFeO₃ (0 1 0)/H₂ System: *Fe3-O19* bridge Site

In general, the charge transfer chemistry proceeds through electrochemically active species such as H₂. It shows the information of interaction between the H₂ molecule and the crystal surface by analysing the Löwdin charge population. Population analysis is a tool used widely by chemists to rationalize molecular properties by determining the distribution of electrons in

a molecule among each of its constituent atoms. The lowdin charge population analysis was computed by using the technique described by Sanchez-Portal et al., (1995).

Table 4.11 lists the lowdin charge population results at *Fe3-O19 bridge* site before and after H₂ adsorption. The change of charges on the surface takes 90.39 %, 90.18 % and 91.00 % of total change for molecular, dihydrogen and dihydride forms of H₂ respectively indicating that the H₂ molecule mainly interact with the atoms on the first atomic surface layer.

On the whole, molecular, dihydrogen and dihydride H₂ gained charges of -0.1675 e, -0.1770 e and -0.2384 e respectively from the LaFeO₃ (0 1 0) surface whilst the first atomic layer of the (0 1 0) LaFeO₃ lost a charge of 0.1975 e, 0.1975 e and 0.2013 e to H₂ respectively for molecular, dihydrogen and dihydride forms of H₂.

This charge gain by the H₂ molecule resulted in hydrogen-hydrogen bond length elongation from 0.740 Å to 1.634 Å and 0.796 Å to 1.634 Å respectively for the molecular and dihydrogen forms of H₂ making it activated, and a reduction from 1.721 Å to 1.636 Å for the dihydride form of H₂.

There was a charge gain of - 0.2913 e, - 0.2959 e and - 0.3258 e by H21 from O19, as well as a charge loss of 0.3880 e, 0.3835 e and 0.3545 e by H22 onto Fe3 respectively for the molecular, dihydrogen and dihydride forms of H₂. This implies that in the O19-H21 bond, the H atom behaves as a cation, whilst in the Fe3-H22 bond, it behaves as an anion.

The Fe3 atom which adsorbs H22 atom, lose a charge of 0.2100 e, 0.2104 e and 0.2126 e respectively for the molecular, dihydrogen and dihydride forms of H₂ after adsorption, making Fe³⁺ turn to Fe²⁺. This agrees with what Hoffmann et al., (2012) reported on change of valance states of B in perovskite ABO₃

Table 4.11 Löwdin Charge Population results for LaFeO₃ (0 1 0) surface before and after H₂ adsorption: *Fe3-O19* bridge Site

Layer	Atom	ID	Molecular Charges (Q) before adsorption	Charges (Q) after adsorption	Change /é	Dihydrogen Charges (Q) before adsorption	Charges (Q) after adsorption	Change /é	Dihydride Charges (Q) before adsorption	Charges (Q) after adsorption	Change /é
Adsorbate	H	21	0.0383	0.3838	-0.3455	0.0336	0.3837	-0.3501	0.0039	0.3842	-0.3803
	H	22	0.0383	-0.1397	0.1780	0.0336	-0.1395	0.1731	0.0039	-0.1380	0.1419
First	Fe	3	0.6639	0.4539	0.2100	0.6639	0.4535	0.2104	0.6639	0.4513	0.2126
	Fe	4	0.6636	0.6278	0.0358	0.6636	0.6278	0.0358	0.6636	0.6265	0.0371
	La	7	0.9526	0.9862	-0.0336	0.9526	0.9863	-0.0337	0.9526	0.9871	-0.0345
	La	8	0.9574	0.9795	-0.0221	0.9574	0.9796	-0.0222	0.9574	0.9770	-0.0196
	O	17	-0.5244	-0.5228	-0.0016	-0.5244	-0.5228	-0.0016	-0.5244	-0.5228	-0.0016
	O	18	-0.5243	-0.5387	0.0144	-0.5243	-0.5386	0.0143	-0.5243	-0.5376	0.0133
	O	19	-0.5266	-0.5808	0.0542	-0.5266	-0.5808	0.0542	-0.5266	-0.5811	0.0545
	O	20	-0.5329	-0.4733	-0.0596	-0.5329	-0.4732	-0.0597	-0.5329	-0.4724	-0.0605
Second	O	15	-0.5085	-0.5173	0.0088	-0.5085	-0.5174	0.0089	-0.5085	-0.5172	0.0087
	O	16	-0.5082	-0.5124	0.0042	-0.5082	-0.5124	0.0042	-0.5082	-0.5120	0.0038
Third	Fe	1	0.6159	0.6090	0.0069	0.6159	0.6088	0.0071	0.6159	0.6092	0.0067
	Fe	2	0.6179	0.6465	-0.0286	0.6179	0.6461	-0.0282	0.6179	0.6468	-0.0289
	O	13	-0.4960	-0.5038	0.0078	-0.4960	-0.5038	0.0078	-0.4960	-0.5035	0.0075
	O	14	-0.5098	-0.5113	0.0015	-0.5098	-0.5113	0.0015	-0.5098	-0.5109	0.0011
Fourth	La	5	1.0948	1.0961	-0.0013	1.0948	1.0962	-0.0014	1.0948	1.0954	-0.0006
	O	11	-0.523	-0.5236	0.0006	-0.5230	-0.5235	0.0005	-0.5230	-0.5233	0.0003
	O	12	-0.5231	-0.5218	-0.0013	-0.5231	-0.5217	-0.0014	-0.5231	-0.5218	-0.0013
Fifth	La	6	1.1753	1.1617	0.0136	1.1753	1.1614	0.0139	1.1753	1.1616	0.0137
	O	9	-0.5163	-0.5237	0.0074	-0.5163	-0.5235	0.0072	-0.5163	-0.5235	0.0072
	O	10	-0.5167	-0.5181	0.0014	-0.5167	-0.5181	0.0014	-0.5167	-0.5184	0.0017

4.3.9 Investigations into Lanthanum Hydride formation on LaFeO₃ (0 1 0) Surface

Virtually all metals will dissolve hydrogen, many rapidly and in large amounts to form true chemical compounds called hydrides. The science of hydrogen-metal systems is an old one. Since the early studies of H-Pd system by Graham in 1866 and 1868, the field of H-Metal systems has substantially grown and developed (Sandrock, 1995). Lanthanum and hydrogen are noted to exist as metallic hydrides with metallic properties such as metallic luster and high electrical conductivity (Sandrock, 1995).

From the earlier studies of hydrogen adsorption on LaFeO₃ (0 1 0) surface at molecular, dihydrogen and dihydride bond distances which is summarised in Table 4.6 and Table 4.7, only the hydride of iron (-FeH) was observed to form. To probe into whether -LaH will indeed form or not, one atom of H was placed on a La atom on the first atomic layer of LaFeO₃ (0 1 0).

After optimization, at the La atomic centre the hydrogen atom which was initially at a bond distance of 1.539 Å from the La8 atom moved away from La8 at a bond distance of 2.885 Å and got adsorbed onto Fe4 at a bond distance of 1.697 Å, forming -FeH (Figure 4.10) as observed in Table 4.6. No H atom was adsorbed on La atom in conformity to what Chen et al., (2014) observed when hydrogen was adsorbed on LaFeO₃ (1 1 0) surface.

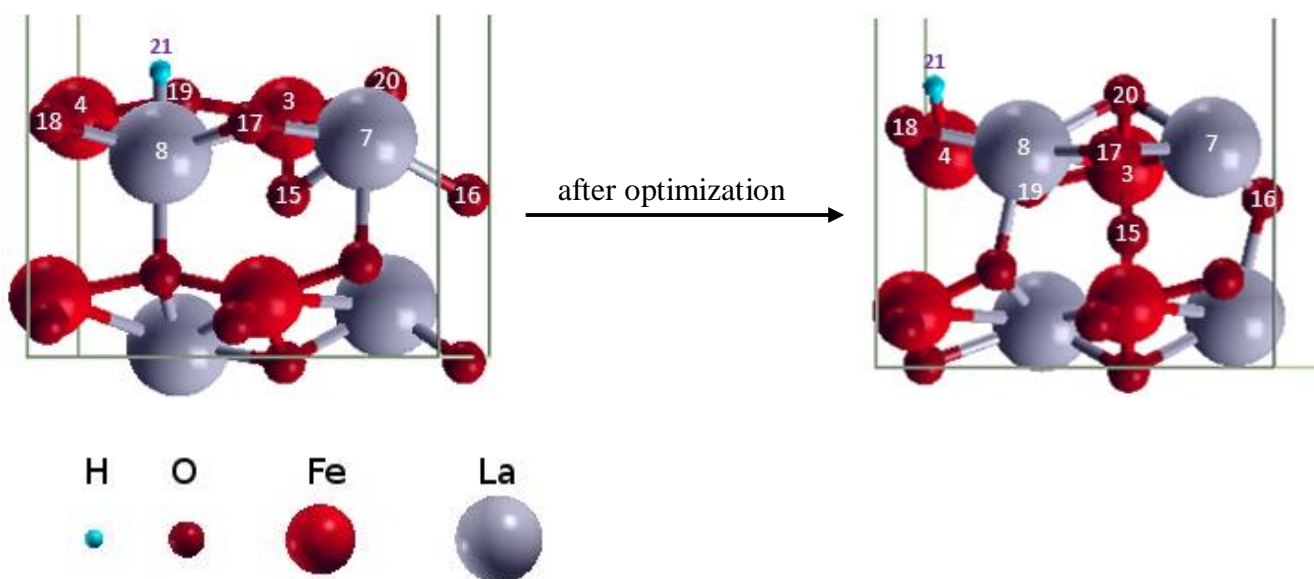


Figure 4.10 Geometries towards investigation into -LaH formation on LaFeO_3 (0 1 0) surface

4.3.10 The Adsorption Mechanism of another H_2 Molecule on LaFeO_3 (0 1 0)/ H_2

From the literature, only one molecule of H_2 is usually adsorbed onto the LaFeO_3 surface, as seen from the work of Chen et al., (2014). However, for a more realistic system, this study was carried out to study the adsorption of another hydrogen on an already adsorbed LaFeO_3 surface, which was the most stable adsorption site (*Fe3-O19 bridge*) when hydrogen was adsorbed at a molecular, dihydrogen and dihydride bond distance.

The *O-top end-on*, *Fe-top end-on*, *Fe-top side-on*, *La-top end-on*, *La-top side-on*, *Fe-O bridge* and *Fe-O bridge** adsorption configurations were chosen to simulate the new H_2 adsorption on the LaFeO_3 (0 1 0)/ H_2 surface. The *Fe-O bridge** is the adsorption site just as *Fe-O bridge* except that the new H_2 was adsorbed at a dihydride bond distance. The H_2 was attached at an initial H-H bond distance of 0.752 Å, 0.747 Å, 0.752 Å, 0.747 Å, 0.752 Å, 1.547 Å and 2.000 Å respectively for those sites considered. The initial and final adsorption configurations are depicted in Figure 4.11 with their calculated structural parameters after adsorption and energies also given in Table 4.12. The adsorption energies

were computed from equation (5), with the one H₂ molecule already adsorbed on the LaFeO₃ (0 1 0) surface at the *Fe3-O19 bridge* site representing the substrate, and the new H₂ molecule serving as the adsorbate.

All the adsorption studies except that at the *Fe-O bridge** site had a negative E_{ads} which corresponds to an exothermic process indicating a stable and spontaneous adsorption. That at the *Fe-O bridge** site corresponds to an endothermic process indicating an unstable adsorption. This very unstable nature of adsorption is as a result of the fact that H₂O which is a good leaving group that forms affords no assurance of leaving the LaFeO₃ (0 1 0)/H₂ surface.

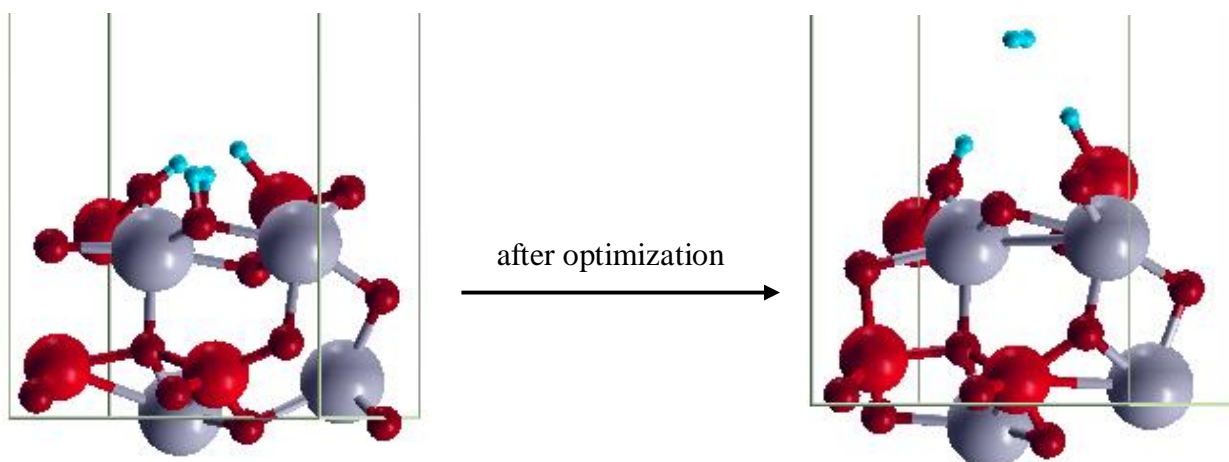
From Figure 4.11, the newly adsorbed H₂ molecule is detached from the surface after optimization for the *O-top end-on*, *Fe-top end-on*, *Fe-top side-on*, *La-top end-on* and *La-top side-on* configurations, indicating non-preferential sites for another H₂ adsorption. This is seen from the equilibrium distances from the adsorption site to the new H₂ adsorbate being much longer than should be the case for an adsorbed species. After adsorption, the H-H bond lengths of the *Fe-O bridge* and *Fe-O bridge** adsorption sites become elongated suggesting that the new H₂ molecule is activated at those sites.

The adsorbed H₂ molecule on the *Fe-O bridge* site gave a fascinating result. After optimization, the new H₂ molecule retained its adsorbed positions but at a bond distance greater than the typical H – H bond length (0.74 – 1.6 Å) as shown in Table 4.12. The already dissociatively adsorbed H₂ which served as the starting point, at the Fe and O sites diffused from the surface to form a normal H – H bond at a distance of 0.753 Å. This suggests that populating the LaFeO₃ surface with H₂ molecule at an already occupied site is not favourable. This is not that surprising as it reflected in its adsorption energy, being relatively exothermically low.

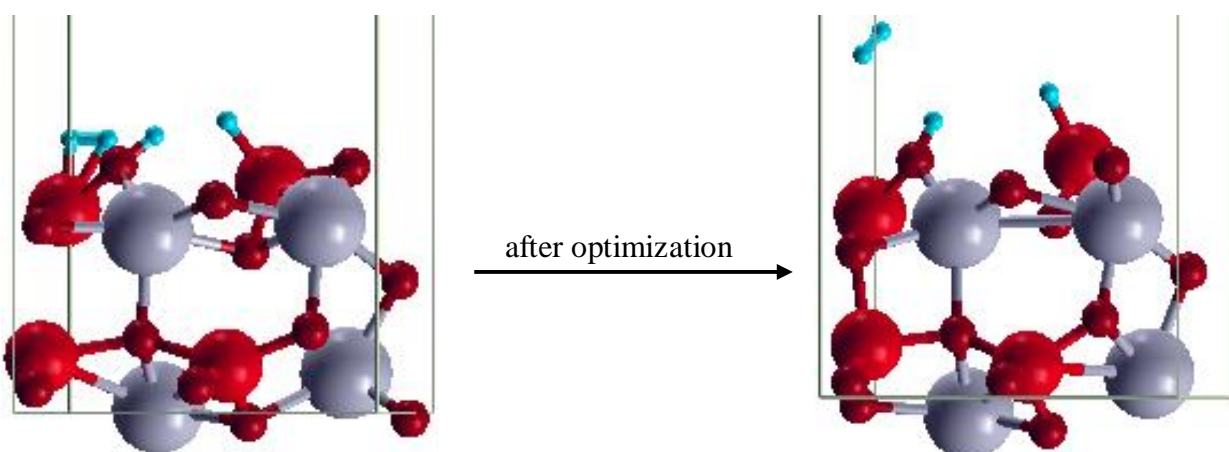
With the idea of the potential for H₂O formation on a LaFeO₃ surface as seen in Table 4.6 and from the work of Chen et al., (2014) where two H atoms form an H₂O molecule with an O atom of a LaFeO₃ (1 1 0) surface, two separate H atoms were adsorbed at the *Fe-O bridge** site (with the H – H bond length greater than the typical 0.74 – 1.6 Å). After optimization, one of the new H atoms which was attached to the O atom site combined with the existing H atom to form H₂O molecule at an H – H distance of 1.621 Å. This adsorption was however unstable and not favourable as shown by its E_{ads} in Table 4.12.

Overall, adsorption energy calculations for the additional molecule of H₂ predict that the *Fe-top end-on* adsorption site gives the most preferred adsorption configuration.

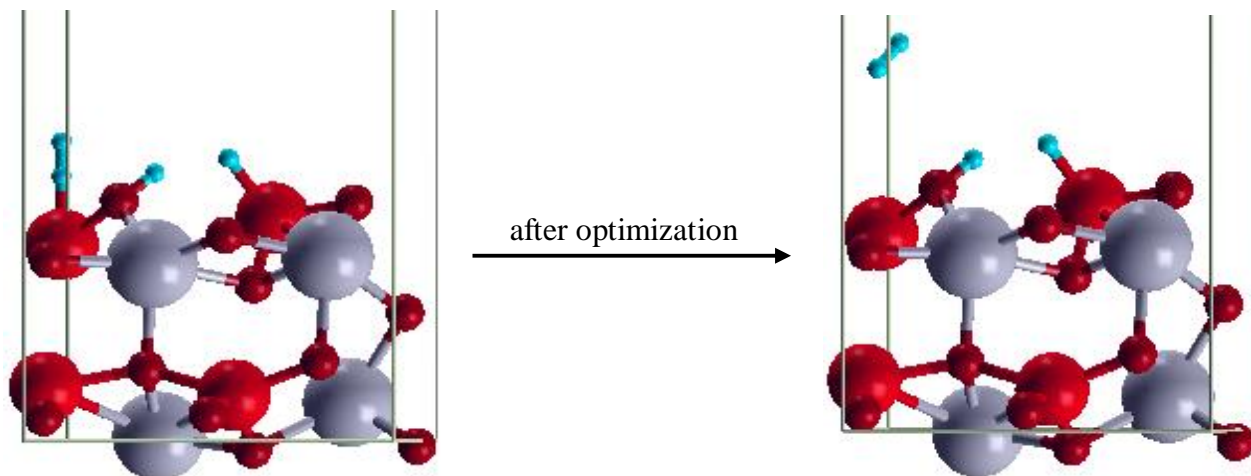
O-top end-on



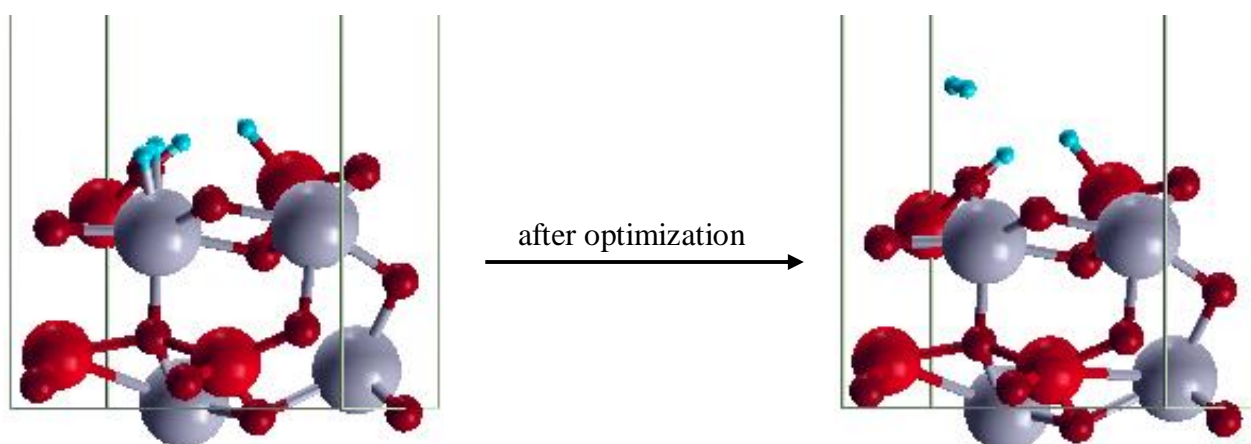
Fe-top end-on



Fe-top side-on



La-top end-on



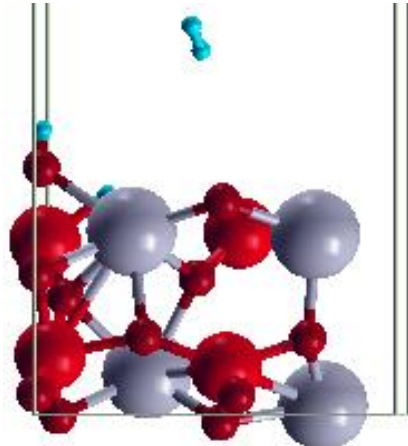
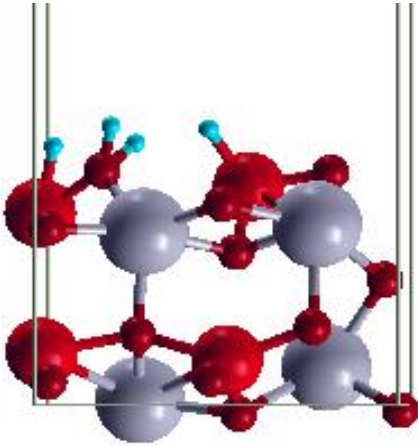
La-top side-on



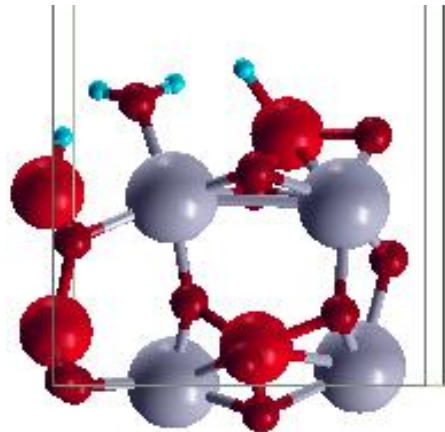
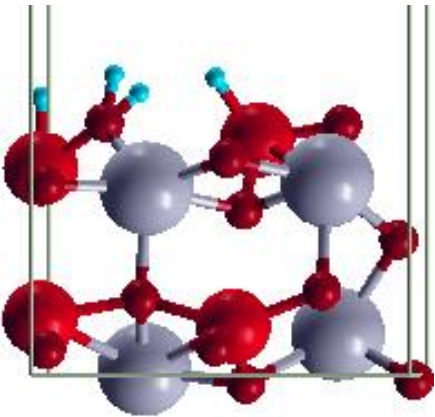
after optimization



Fe-O bridge



*Fe-O bridge**



(a) Initial guess structure

(b) Optimized structure

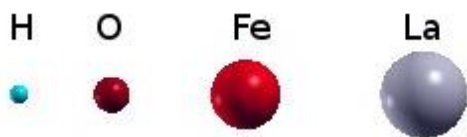


Figure 4.11 Side views of the initial and optimized structures of the possible adsorption sites on an already adsorbed *Fe-O bridge* site

Table 4.12 Calculated structural parameters and energies of the possible adsorption sites on an already adsorbed *Fe-O bridge* site (most stable adsorption configuration when one H₂ molecule was adsorbed)

Adsorption site	E _{ads} /eV	r _{H-H} /Å	r _{H-O} /Å	r _{H-La} /Å	r _{H-Fe} /Å
<i>O-top end-on</i>	- 0.273	0.754	3.831	-	-
<i>Fe-top end-on</i>	- 0.280	0.754	-	-	3.704
<i>Fe-top side-on</i>	- 0.028	0.753	-	-	3.515
<i>La-top end-on</i>	- 0.033	0.754	-	3.633	-
<i>La-top side-on</i>	- 0.016	0.752	-	4.929	-
<i>Fe-O bridge</i>	- 0.015	2.683	0.974	-	1.699
<i>Fe-O bridge*</i>	0.514	2.859	0.981	-	1.616

*Fe-O bridge** is the adsorption site when H – H bond length is greater than the typical 0.74 - 1.6 Å H – H bond length (dihydride). r_{H-H} , r_{H-O} , r_{H-La} and r_{H-Fe} are the shortest distances of H atoms, H atom and O atom, H atom and La atom, and H atom and Fe atom, respectively.

4.3.11 The Potential of H₂O as a Good Leaving Group on LaFeO₃ (0 1 0)/2H₂ at *Fe-O bridge** Site

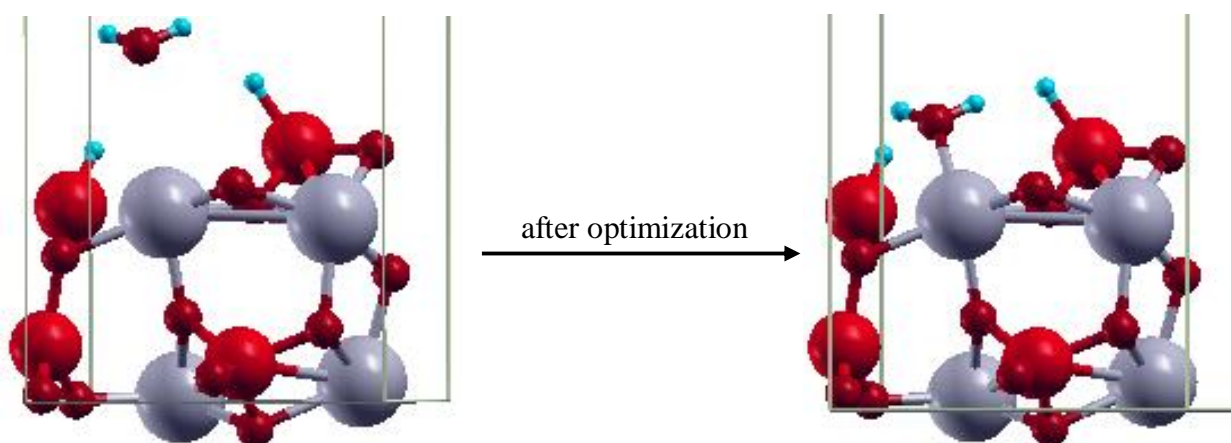
Water, a molecular fragment that departs with a pair of electrons in heterolytic bond cleavage, is known to be a good leaving group in many organic and inorganic reactions since it is the conjugate base of H₃O⁺, which is a strong acid. The potential of H₂O to leave the LaFeO₃ crystal surface as seen in this work and predicted by Chen et al., (2014) creates an oxygen vacancy which has the ability to alter a lot of its material properties. However, as to whether H₂O will indeed leave the LaFeO₃ (0 1 0)/2H₂ surface or not even though it has an adsorption energy which is unfavourable, it is not known, hence this studies.

The H₂O was physically detached from the LaFeO₃ /H₂ surface of the optimized structure at the *Fe-O bridge** site with a La – O and H – H bond distances of 3.882 Å and 1.620 Å respectively so as to find out whether it will return to its initial position or remain out of the

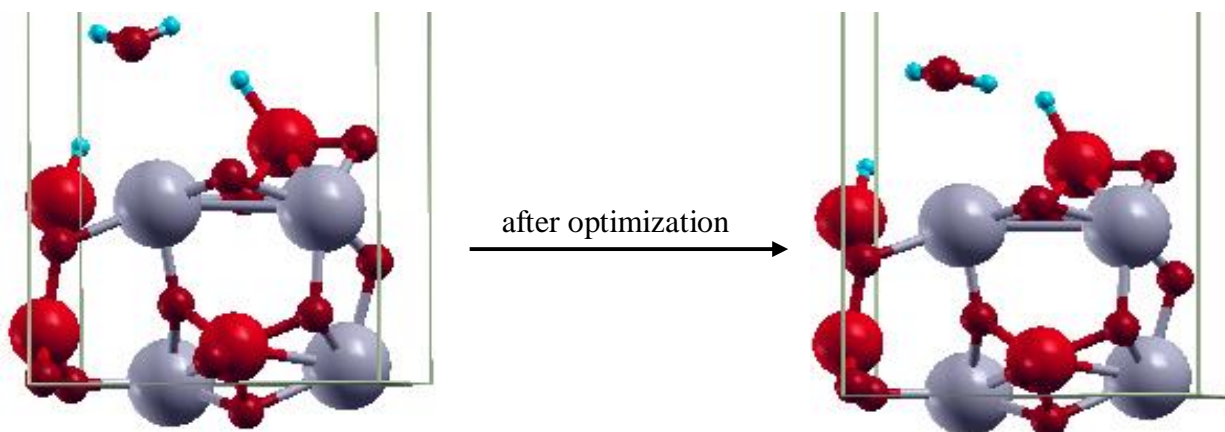
typical La – O bonding range. However, after optimization the H₂O molecule returned to its initial position with a La – O bond distance of 2.586 Å and an H – H distance of 1.621 Å.

To rule out any doubts, constrained optimization/ dynamics was adopted on the detached H₂O. The La – O bond (3.882 Å) connecting the two O – H bonds of the H₂O at an H – H bond distance of 1.620 Å were constrained and allowed to optimize, after which the constraints on the optimized structure were removed and again allowed to optimize giving La – O and H – H bond distances of 2.584 Å and 1.621 Å respectively. The H₂O returned to the surface after optimization with a La – O bond distance of 2.584 Å proving the fact that even though H₂O is a good leaving group on LaFeO₃ (0 1 0) surface, it is not so on a LaFeO₃ (0 1 0)/H₂ surface (as seen from the adsorption energy) and as such would not create an oxygen vacancy on the LaFeO₃ (0 1 0)/H₂ surface. The geometries of the initial and optimized structures are shown in Figure 4.12.

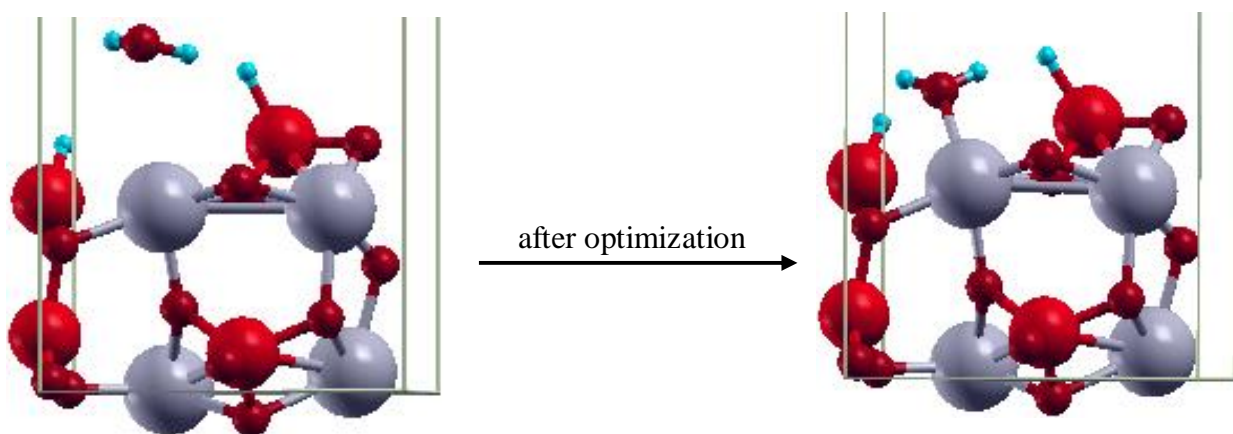
Detaching H₂O



Constrained



Constraints Removed



(a) Initial guess structure

(b) Optimized structure

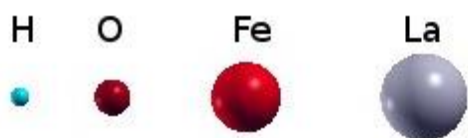


Figure 4.12 Geometries towards the potential of H₂O as a good leaving group in LaFeO₃ (0 1 0)/2H₂ at Fe-O bridge* site

4.3.12 Analysis of PDOS and TDOS Plots for two H₂ adsorption on LaFeO₃ (0 1 0) Surface

The nature of interaction between two hydrogen molecules and LaFeO₃ (0 1 0) surface is deduced from the projected density of states (PDOS) which analyses the change of valence states and energies. The total density of states (TDOS) also helps in describing the number of states per interval of energy at each energy level that are available to be occupied. Figure 4.14 lists the PDOS of hydrogen, oxygen, iron and lanthanum at the first surface layer, and the TDOS of H₂ molecule adsorption on LaFeO₃ (0 1 0)/H₂ substrate at the *Fe-top end-on* adsorption configuration before and after adsorption, respectively. The adsorption structures are labelled at the first and second surface layers to aid in this analysis, and is shown in Figure 4.13 below.

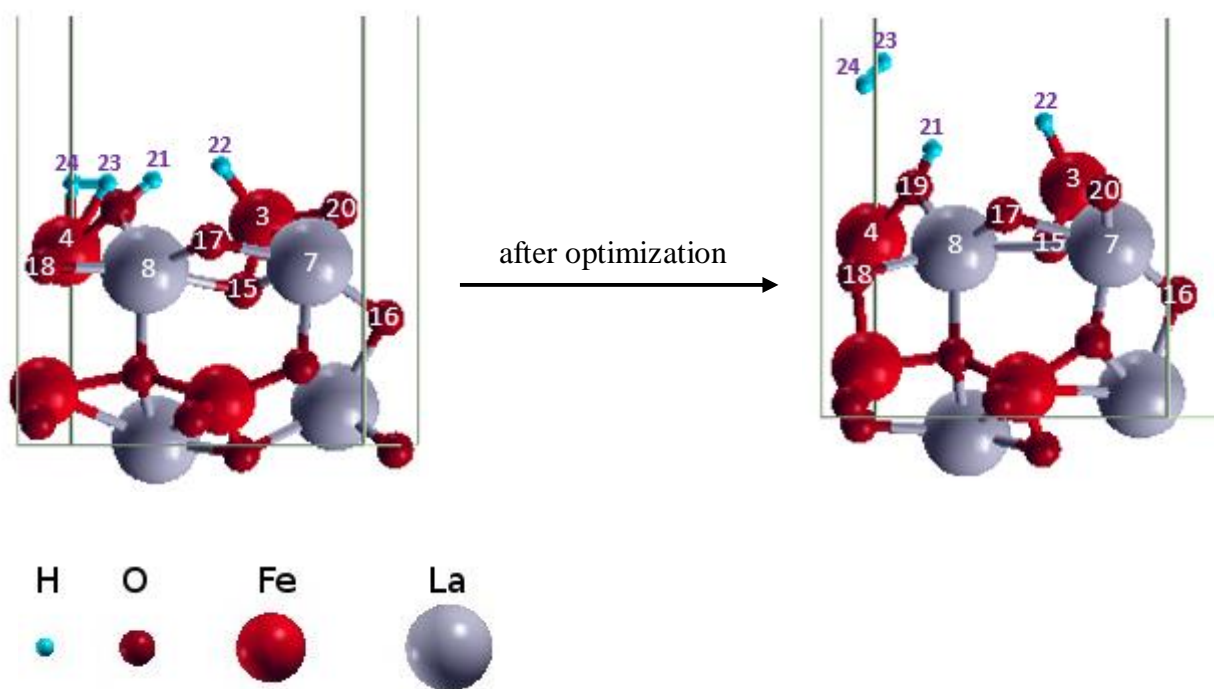
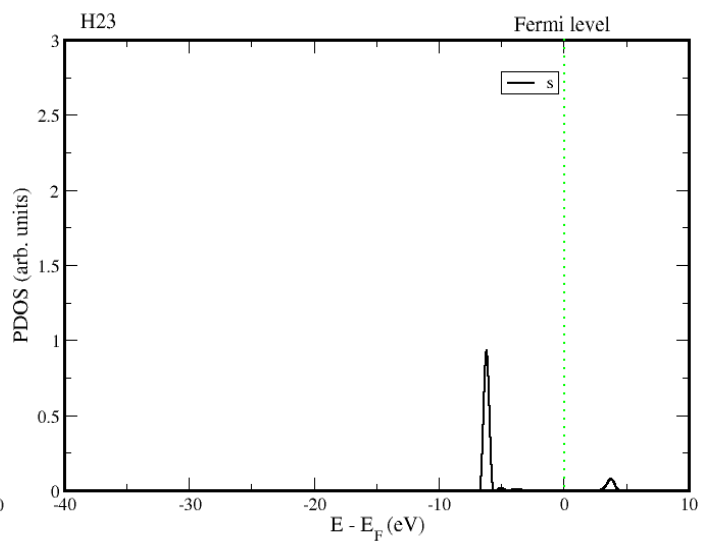
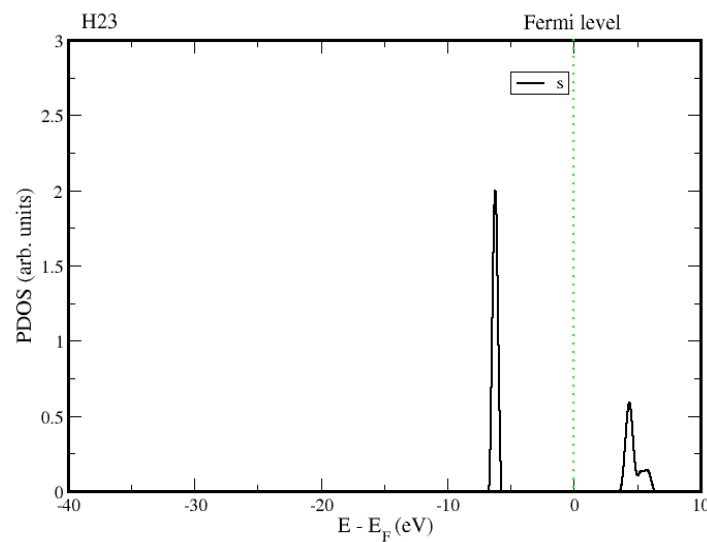
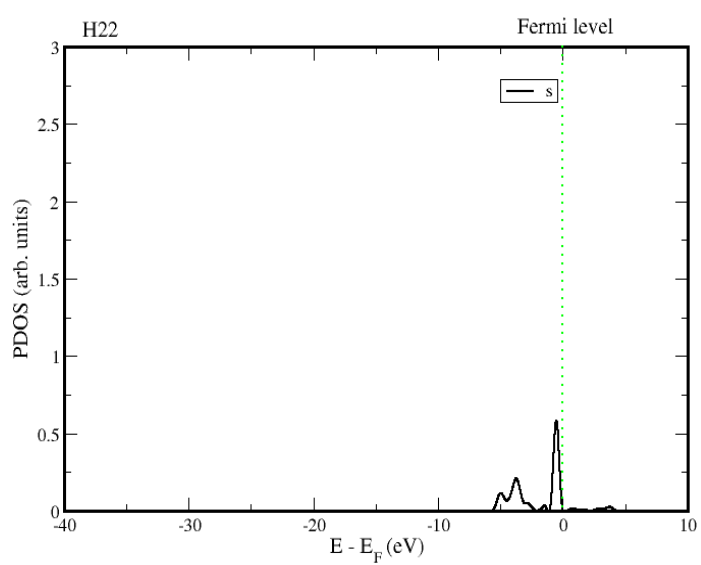
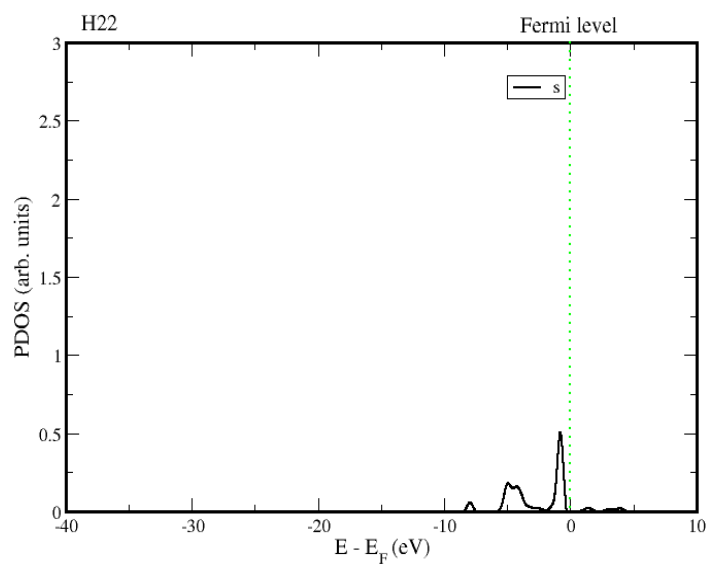
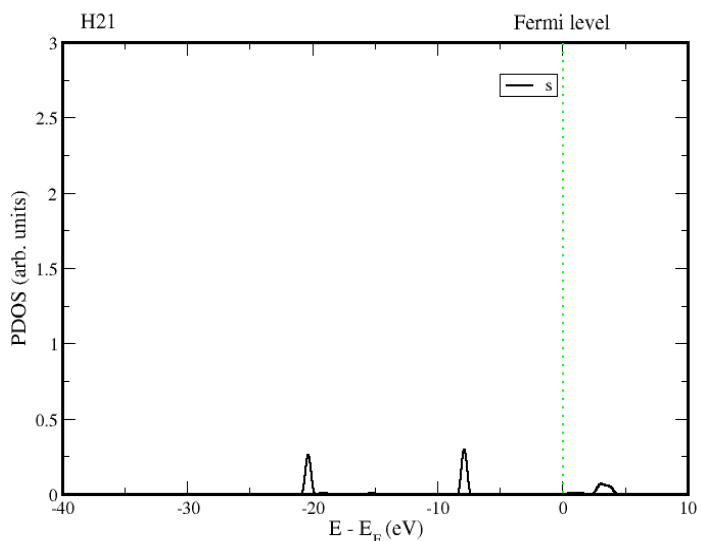
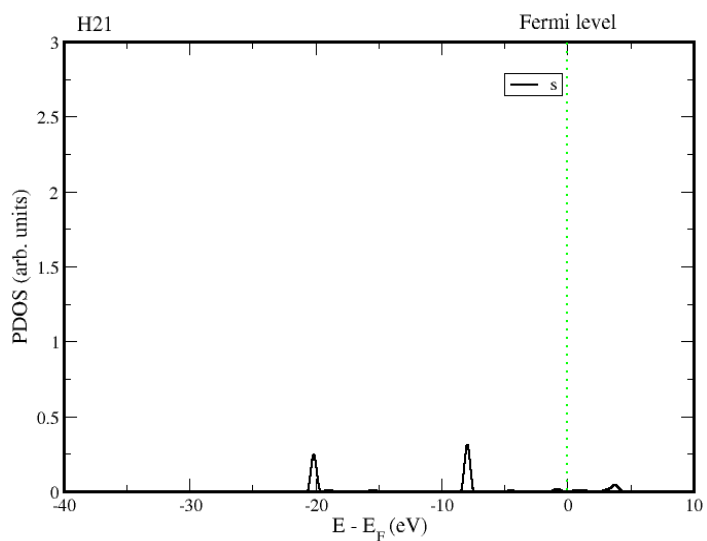


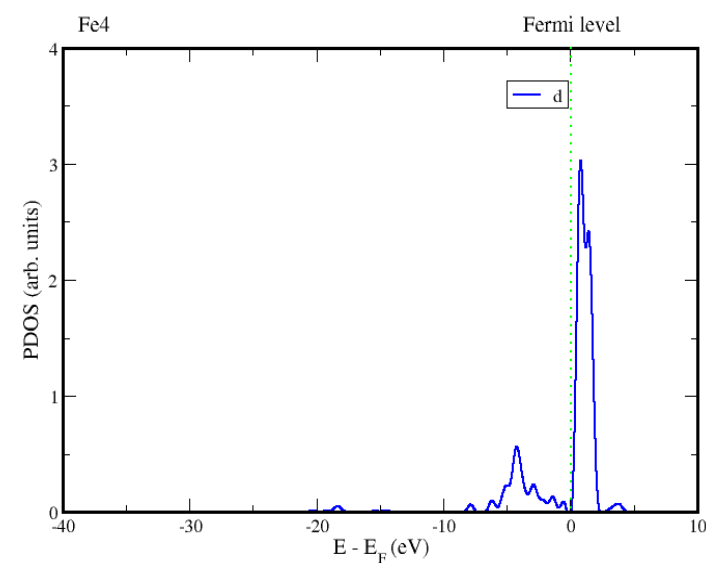
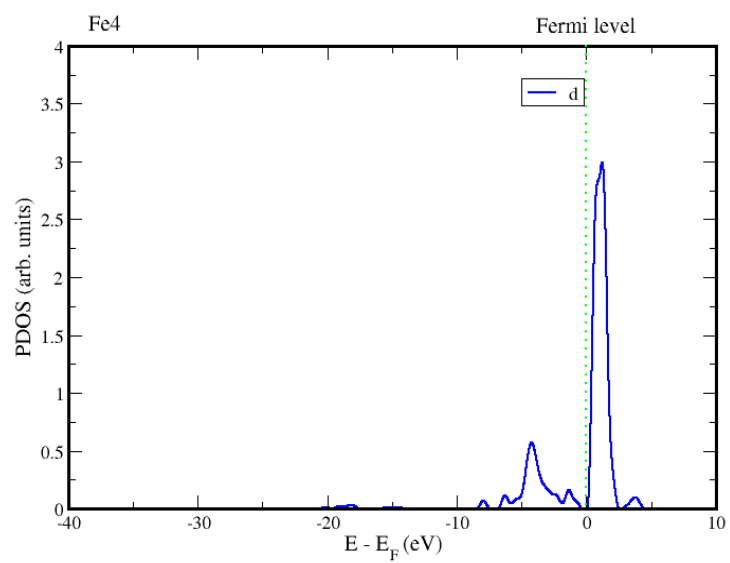
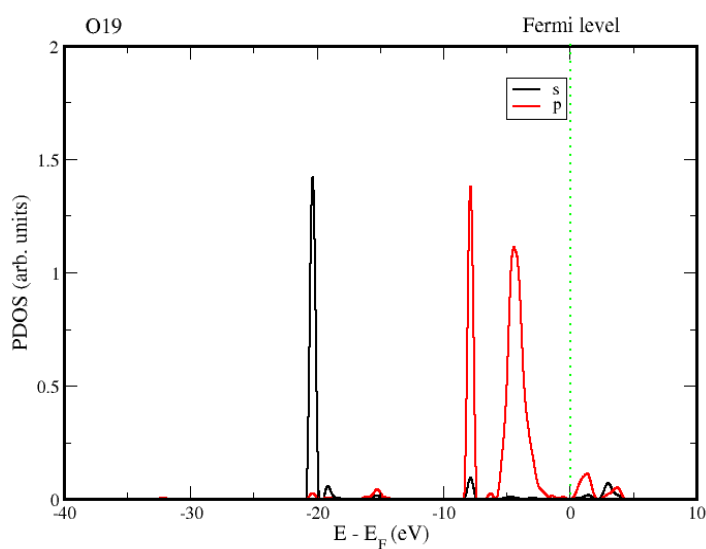
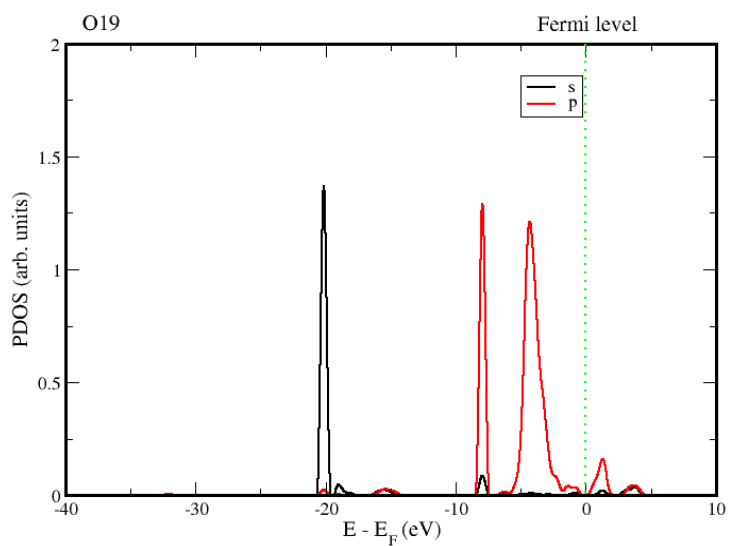
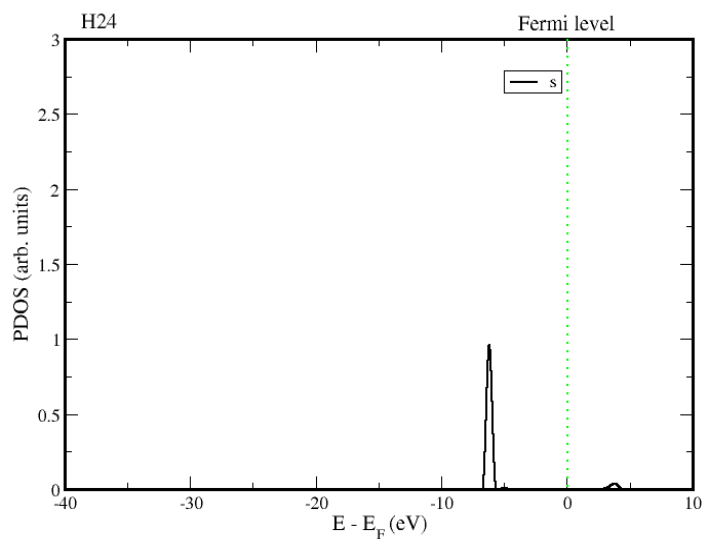
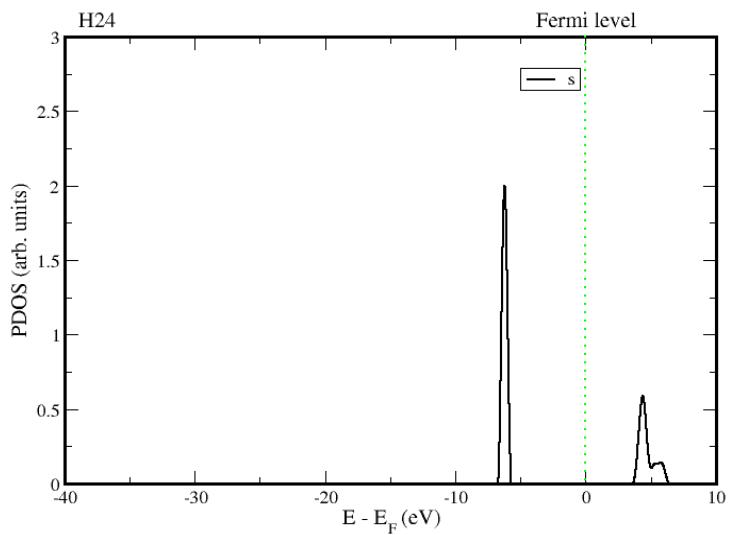
Figure 4.13 Side view of initial and optimized structures at *Fe-top end-on* site

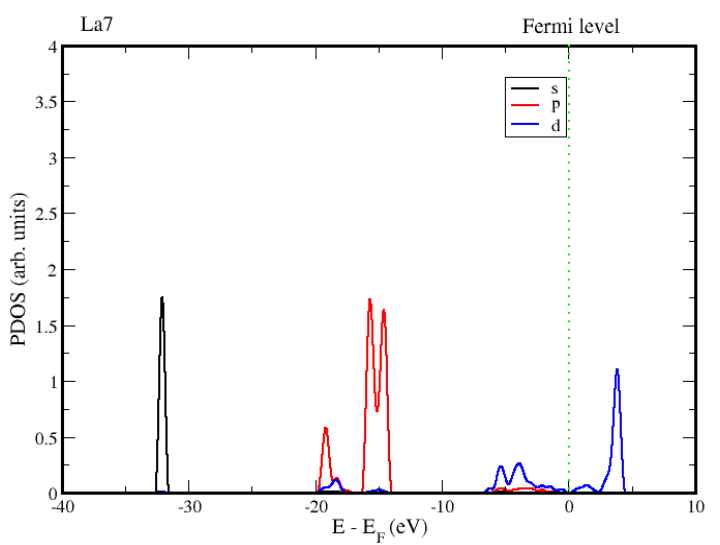
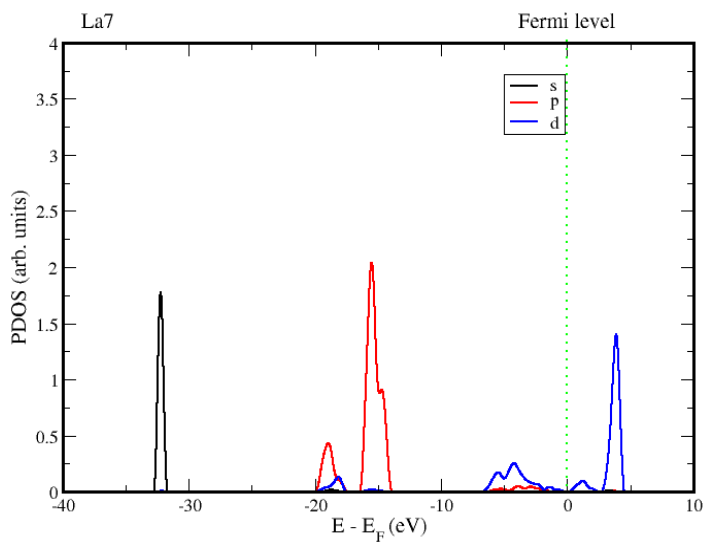
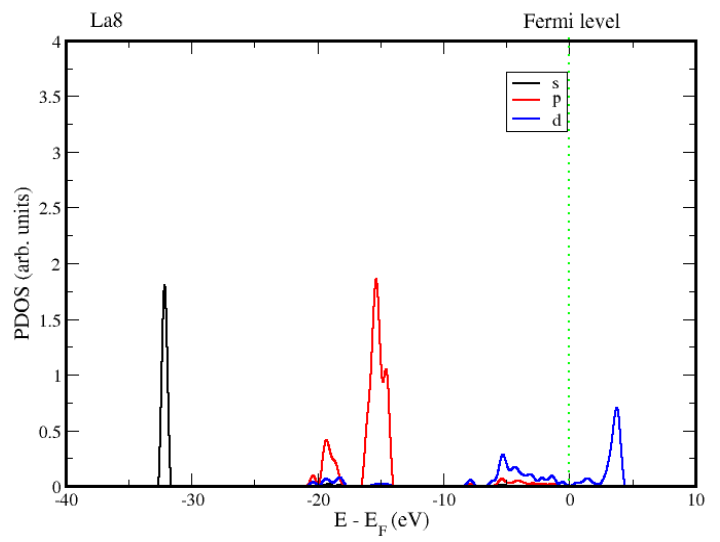
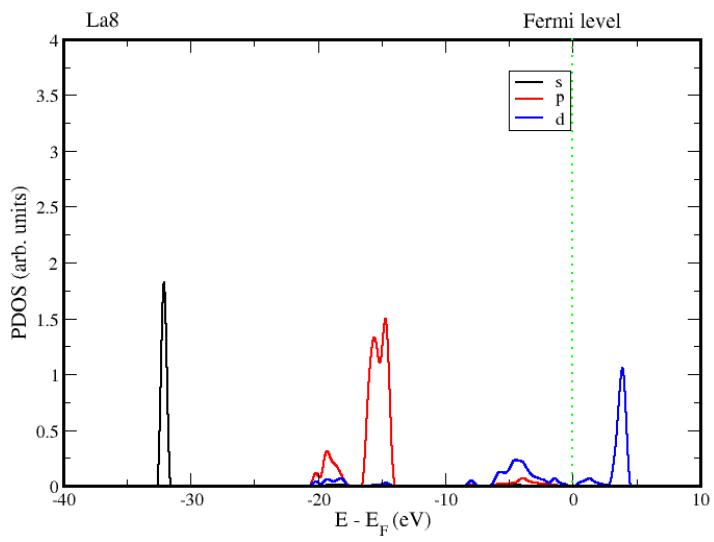
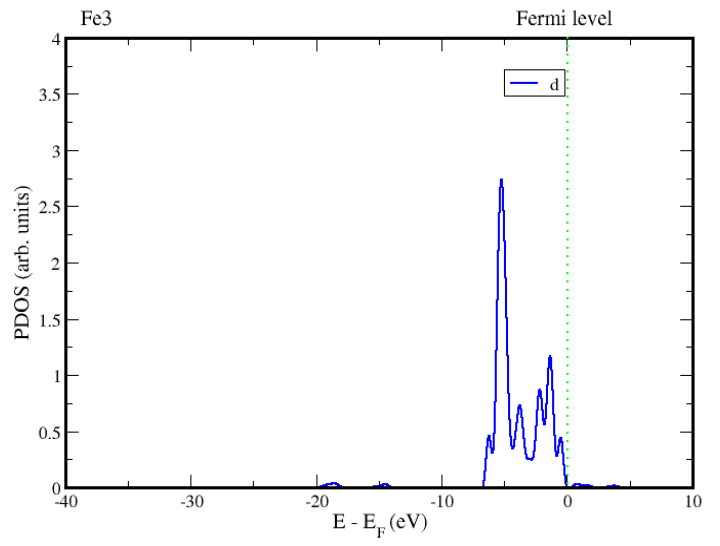
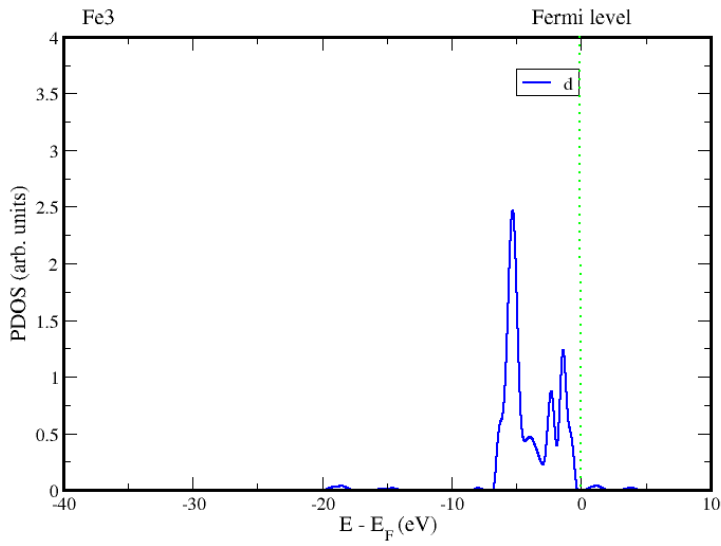
When the new H₂ molecule (H23 and H24 atoms) is far from LaFeO₃ (0 1 0) surface, there is a sharp and a bit of broad peak attributed to a bonding molecular orbital of H₂. After

adsorption, there was no dissociation into atomic H, and position of the s- orbital peaks remained at where they were initially only with a decrease in their intensity. This was because no hybridization occurred in the adsorption process. None of the atomic orbital peaks overlapped or coincided with each other, and it reflected in the optimized adsorption structure (Figure 4.13) as a weak chemical interaction. The peaks of projected density of states of H23 and H24 atoms that fell after adsorption was because the energy of the LaFeO₃ (0 1 0) surface got lowered and the structure became more stable after adsorption. All the PDOS of the atoms involved in the adsorption changed, meaning their charge populations changed, and is seen in Table 4.13.

The Total density of states (TDOS) profiles did not show any significant changes after adsorption. No new peak was observed to form and the energy gap between the highest occupied and lowest unoccupied eigenvalues decreased from 0.9882 eV to 0.9197 eV. The magnetic moments of the surface Fe atoms were found to slightly increase from 4.605 μ_B to 4.685 μ_B . These observations were as a result of the weak chemical interaction between the new H₂ molecule and the LaFeO₃ (0 1 0)/H₂ surface.







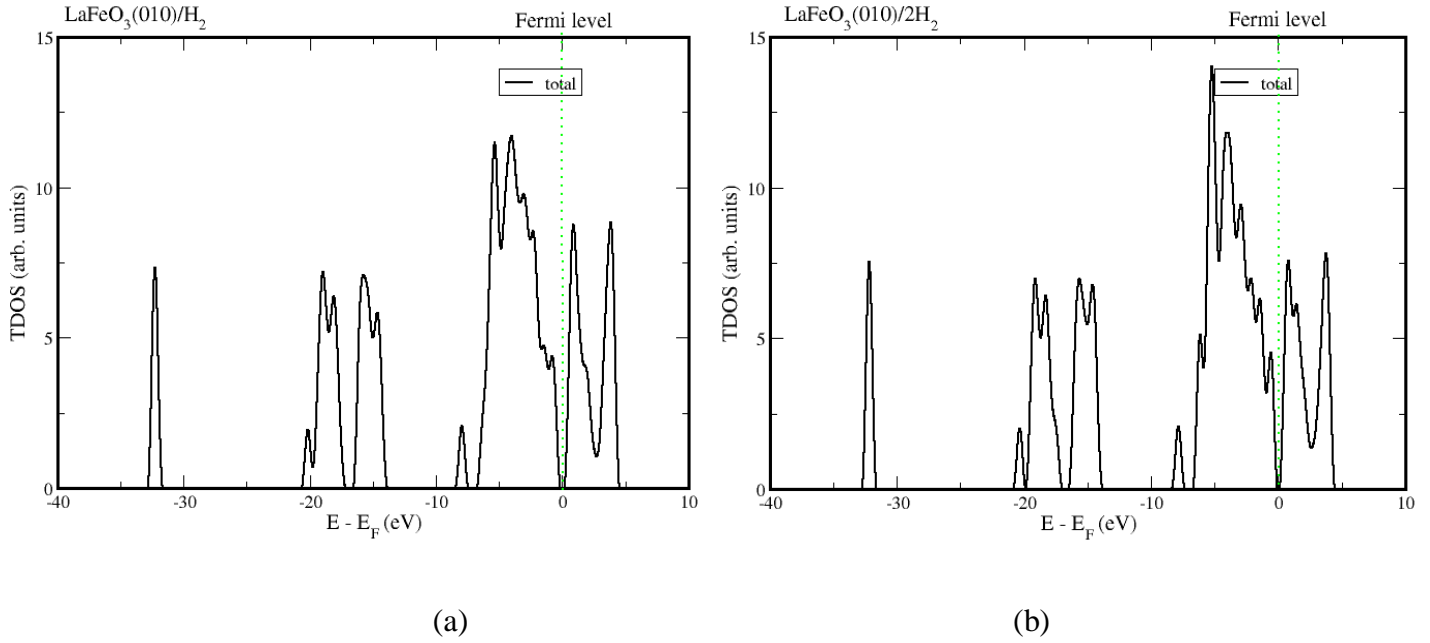


Figure 4.14 PDOS and TDOS for two H₂ molecule adsorption (a) before adsorption and (b) after adsorption on *Fe-top end-on* site

4.3.13 Analysis of the Löwdin Charge Population on LaFeO₃ (0 1 0)/2H₂ System: *Fe-top end-on* Adsorption Site

The Löwdin charge population analysis on LaFeO₃ (0 1 0)/2H₂ system at the *Fe-top end-on* adsorption site before and after adsorption, respectively is listed in Table 4.13. Gas phase H₂ molecule and an already H₂ adsorbed LaFeO₃ (0 1 0) surface are compared with the corresponding figures upon adsorption. Upon adsorption, the new hydrogen molecule lost a charge of 0.01 ϵ to the LaFeO₃ (0 1 0)/H₂ system that served as the surface, whilst the LaFeO₃ (0 1 0)/H₂ system (one H₂ molecule adsorbed on LaFeO₃ (0 1 0) surface) gained a charge of - 0.0365 ϵ . A decrease in Löwdin charge (negative) is a decrease in electron charge. The charge transfer from the new H₂ molecule resulted in hydrogen-hydrogen bond length elongation from 0.747 Å to 0.754 Å, making it activated. The Fe4 atom which served as the site for the new H₂ molecule (Figure 4.13) lost a charge of 0.0153 ϵ after adsorption. This made Fe³⁺ originally in LaFeO₃ turn to Fe²⁺, agreeing with Hoffmann et al., (2012) report on change of valance states of B atoms in perovskite ABO₃.

Table 4.13 Löwdin charge population results for LaFeO₃ (0 1 0) surface before and after two H₂ molecule adsorption

Layer	Atom	ID	Charges (Q) before adsorption / e	Charges (Q) after adsorption / e	Change / e
	H	23	0.0373	0.0363	0.001
	H	24	0.0373	0.0283	0.009
	H	21	0.3837	0.4058	-0.0221
	H	22	-0.1398	-0.1374	-0.0024
First	Fe	3	0.4539	0.4693	-0.0154
	Fe	4	0.6278	0.6125	0.0153
	La	7	0.9863	0.9813	0.005
	La	8	0.9799	1.0187	-0.0388
	O	17	-0.5229	-0.5046	-0.0183
	O	18	-0.5386	-0.5496	0.011
	O	19	-0.5809	-0.5949	0.014
	O	20	-0.4732	-0.4884	0.0152
Second	O	15	-0.5175	-0.5131	-0.0044
	O	16	-0.5125	-0.494	-0.0185
Third	Fe	1	0.6089	0.6175	-0.0086
	Fe	2	0.6464	0.6726	-0.0262
	O	13	-0.5038	-0.5041	0.0003
	O	14	-0.5113	-0.4879	-0.0234
Fourth	La	5	1.0963	1.0923	0.004
	O	11	-0.5236	-0.5454	0.0218
	O	12	-0.5218	-0.5332	0.0114
Fifth	La	6	1.1616	1.1078	0.0538
	O	9	-0.5237	-0.5449	0.0212
	O	10	-0.518	-0.5304	0.0124

CHAPTER FIVE

5. SUMMARY AND CONCLUSIONS

The results of the study show that:

1. For the use of LaFeO_3 as anodic material in Ni-MH batteries, the most preferred adsorption site for H_2 is the *Fe-O bridge* site where the O coordinates to another Fe atom and a La atom, and the Fe in the bridge coordinates to two other O atoms and two La atoms. When one molecule of the H_2 is adsorbed at H-H molecular, dihydrogen and dihydride bond distances on this *Fe-O bridge* site of the LaFeO_3 (0 1 0) surface, $-\text{Fe}(\mu\text{OH})\text{La}$ and $-\text{FeH}$ are formed with E_{ads} in the range -0.455 to -0.456 eV. Similar adsorption sites do not necessarily give the same products on addition of H_2 . Even though some *Fe-O bridge* sites give $-\text{Fe}(\mu\text{OH})\text{La}$ and $-\text{FeH}$ others give LaOH and FeH . At the O top end-on sites, while some give LaOH and FeH , others give H_2O or FeOH depending on the H-H distances. All the O-top sites with the exception of that which coordinates to only La at the terminal position form H_2O in at least one of the forms of H_2 in an end-on attachment to O atom, leaving the surface to create an oxygen vacancy. Nonetheless, it is only at the O site which connects just two La atoms and in the dihydride H-H bond distance end-on configuration that involves dislodgement of H_2O from the surface and vacancy hopping oxygen transport. Molecular hydrogen on the LaFeO_3 (0 1 0) surface can only form H_2O at the O top end-on site where the O coordinates to two Fe atoms and a La atom. Fe and La dihydrogen and dihydride bonds do not form on LaFeO_3 (0 1 0) surface and also no hydrogen is adsorbed on the La atom. O atom facilitates the addition of hydrogen on the surface.

For an additional molecule of H₂ adsorption on LaFeO₃ (0 1 0) surface where hydrogen has already been adsorbed on the most stable adsorption configuration (*Fe-O bridge* site), the *Fe-top end-on* adsorption site gives the most preferred adsorption configuration.

2. Hydrogen adsorption at the *Fe-O bridge** site where the second H₂ is at a dihydride bond distance corresponds to an endothermic process indicating an unstable adsorption. This very unstable nature of adsorption is as a result of the fact that the H₂O which forms on the LaFeO₃ (0 1 0)/2H₂ surface proceeds via an unfavourable adsorption process, making it impossible to form an oxygen vacancy on the surface. Finally, populating LaFeO₃ surface with H₂ molecule at an already occupied site is not favourable.
3. Fe changes oxidation state from +3 to +2 when one and two molecules of H₂ are adsorbed. This is consistent with Hoffmann et al., (2012) report on change of valence states of B atoms in perovskite ABO₃.
4. The interaction between H₂ and LaFeO₃ (0 1 0) surface at the *Fe-O bridge* site where Fe coordinates to three O atoms and two La atoms and the O also coordinates to two Fe atoms is mainly due to the overlapping of H 1s, O 2s and O 2p states, Fe 3d state, and La 5p and 5d states.
5. GGA+U provides the best model for LaFeO₃ which is a G-type antiferromagnetic material.

REFERENCES

- Armaroli, N.; Balzani, V. (2011) The Hydrogen Issue *ChemSusChem*. 4(1):21 - 36
- Atkins, P.W.; Overton, T.L.; Rourke, J.P.; Weller, M.T.; Armstrong, F.A, (2010) Shriver and Atkins' Inorganic Chemistry, Fifth Edition *Oxford University Press* ISBN 978-1-42-921820-7, p. 289
- Avdeev, M.; Caspi, E. N.; Yakovlev, S., (2007) On the polyhedral volume ratios V_A/V_B in perovskites ABX_3 *Acta Crystallogr. B* 63:363 - 372
- Beek, J. R. V.; Donkersloot, H. C.; Willems, J. J. G. (1985) Proc. 14th Power Source Symp., Brighton, in: L.J. Pearce (Ed.) *Power Sources*, Vol. 10, p. 317
- Benson, S. W., (1965) Bond energies *J. Chem. Educ.*, 42:502 - 18
- Berenov, A.; Angeles, E.; Rossiny, J.; Raj, E.; Kilner, J.; Atkinson, A., (2008) Structure and transport in rare-earth ferrates *Solid State Ionics* 179:1090 - 1093
- Bhalla, A. S.; Guo, R.; Roy, R., (2000) The perovskite structure – a review of its role in ceramic science and technology *Mat Res Innovat* 4:3 - 26
- Bliznakov, S.; Drenchev, N.; Drenchev, B.; Delchev, P.; Solsona, P.; Spassov, T. (2005) Electrochemical properties of nanocrystalline Mg_2Ni -type alloys prepared by mechanical alloying *J. Alloys Compd.* 682:404 - 406
- Bockris, J. O. M. (2002) The origin of ideas on a hydrogen economy and its solution to the decay of the environment *International Journal of Hydrogen Energy* 27(7-8):731 - 740
- Boekema, C.; Jonker, P. C.; Filoti, G.; Van Der Woude, F., (1979) Super Transfer in Doped $LaFeO_3$ *Hyperfine Interactions* 7:45 - 60
- BP Statistical Review of World Energy (2012) www.bp.com/statisticalreview. [Accessed on 12/09/2014]
- Catalli, K.; Shim, S-H.; Prakapenka, V. B.; Zhao, J.; Sturhahn, W.; Chow, P.; Xiao, Y.; Liu, H.; Cynn, H.; Evans, W. J.; (2010) Spin state of ferric iron in $MgSiO_3$ perovskite and its effect on elastic properties *Earth Planet. Sci. Lett.* 289:68 - 75
- Chen, Y-H.; Zhang, B-W.; Yang, L.; Zhang, M-L.; Zhang, C-R.; Kang, L.; Luo, Y-C., (2014) First-Principle Study of H_2 Adsorption on $LaFeO_3$ (110) Surface *Journal of Nanomaterials* Volume 2014, Article ID 758985, 8 pages
- Ciambelli, P.; Cimino, S.; Lisi, L.; Faticanti, M.; Minelli, G.; Pettiti, I.; Porta, P., (2001) La, Ca and Fe oxide perovskites: preparation, characterisation and catalytic properties for methane combustion *Appl. Catal. B Environ* 33:193 - 203
- Conte, M.; Prosini, P. P.; Passerini, S. (2004) Overview of energy/hydrogen storage: state-of-the-art of the technologies and prospects for nanomaterials *Mater. Sci. Eng., B* 108:2 – 8

- Cuevas, F.; Joubert, J. M.; Latroche, M.; Percheron-Guégan, A. (2001) Intermetallic compounds as negative electrodes of Ni/MH batteries *Appl. Phys. A: Mater. Sci. Process.*, 72(2):225 - 238
- Cuscueta, D. J.; Ghilarducci, A. A.; Salva, H. R. (2010) Design, elaboration and characterization of a Ni-MH battery prototype *International Journal of Hydrogen Energy* 35(20):11315 - 11323
- David, W. I. F. (2011) Effective hydrogen storage: a strategic chemistry challenge *Faraday Discuss.*, 151:399 - 414
- Dean, J. A. (Ed.) (1999) *Lange's Handbook of Chemistry*, 15th edition, McGraw-Hill, New York, NY, USA
- Deng, G.; Chen, Y.; Tao, M.; Wu, C.; Shen, X.; Yang, H.; Liu, M. (2010) Electrochemical properties and hydrogen storage mechanism of perovskite-type oxide LaFeO₃ as a negative electrode for Ni/MH batteries *Electrochim. Acta* 55:1120
- Deutsch, P. P.; Eisenberg, R., (1988) Stereochemistry of hydrogen oxidative addition and dihydride-transfer reactions involving iridium(I) complexes *Chem. Rev.* 88(7):1147 - 1161
- Dogra, R.; Junqueira, A. C.; Saxena, R. N.; Carbonari, A. W.; Mestnik-Filho, J.; Moralles, M., (2001) Hyperfine interaction measurements in LaCrO₃ and LaFeO₃ perovskites using perturbed angular correlation spectroscopy *Physical Review B*, 63:224104
- Dornheim, M.; Doppiu, S.; Barkhordarian, G.; Boesenberg, U.; Klassen, T.; Gutfleisch, O.; Bormann, R. (2007) Hydrogen Storage in Magnesium-Based Hydrides and Hydride Composites, Viewpoint Set on Mg-based hydrogen storage materials *Scr. Mater.*, 56, 841 - 846
- Eberle, U.; von Helmolt, R. (2010) Sustainable transportation based on electric vehicle concepts: a brief overview *Energy Environ. Sci.*, 3:689 - 699
- Esaka, T.; Sakaguchi, H.; Kobayashi, S. (2004) Hydrogen storage in proton conductive perovskite type oxides and their application to nickel-hydrogen batteries *Solid State Ionics* 166:351
- Feng, F.; Geng, M. M.; Northwood, D. O. (2001) Electrochemical behaviour of intermetallic-based metal hydrides used in Ni-MH batteries: a review *Int. J. Hydrogen Energy* 26:725 - 734
- Fossdal, A.; Menon, M.; Waernhus, I.; Wiik, K.; Einarsrud, M. A.; Grande, T., (2004) Crystal structure and thermal expansion of La_{1-x}Sr_xFeO_{3-δ} *J. Am. Ceram. Soc.* 87:1952 - 1958
- Gang, D.; Yungui, C.; Mingda, T.; Chaoling, W.; Xiangqian, S.; Heng, Y.; Ding, Z. (2009) Preparation and electrochemical property of LaFeO₃ electrode material *Acta Chim. Sin.* 67(17):2001 - 2004

- Geller, S.; Racah, P. M., (1970) Phase Transitions in Perovskite-like Compounds of the Rare Earths *Phys. Rev. B* 2:1167
- Giannozzi, P.; Baroni, S.; Bonini, N.; Calandra, M.; Car, R.; Cavazzoni, C.; Ceresoli, D.; Chiarotti, G. L.; Cococcioni, M.; Dabo, I.; Corso, A. D.; de Gironcoli, S.; Fabris, S.; Fratesi, G.; Gebauer, R.; Gerstmann, U.; Gougoussis, C.; Kokalj, A.; Lazzeri, M.; Martin-Samos, L.; Marzari, N.; Mauri, F.; Mazzarello, R.; Paolini, S.; Pasquarello, A.; Paulatto, L.; Sbraccia, C.; Scandolo, S.; Sclauzero, G.; Seitsonen, A. P.; Smogunov, A.; Umari, P.; Wentzcovitch, R. M., (2009) QUANTUM ESPRESSO: a modular and open-source software project for quantum simulations of materials *J. Phys.: Condens. Mater* 21(39):395502
- Glazer, A. M., (1972) The classification of tilted octahedral in perovskites *Acta Crystallogr. Section B*, 28(11):3384 - 3392
- Goldschmidt, V. M., (1926) Die Gesetze der Krystallochemie *Naturwissenschaften* 14(21):477 - 485
- Hadidi, K.; Hancke, R.; Norby, T.; Gunnæs, A. E.; Løvvik, O. M. (2012) Atomistic study of LaNbO₄; surface properties and hydrogen adsorption, *International Journal of Hydrogen Energy* 37:6674 - 6685
- Hamada, I.; Uozumi, A.; Morikawa, Y.; Yanase, A.; Katayama-Yoshida, H. (2011) A density functional theory study of self-regenerating catalysts LaFe_{1-x}M_xO_{3-y} (M = Pd, Rh, Pt) *J Am Chem Soc* 133:18506 - 18509
- Hashimoto, T.; Matsushita, N.; Murakami, Y.; Kojima, N.; Yoshida, K.; Tagawa, H.; Dokiya, M.; Kikegawa, T., (1998) Pressure-Induced Structural Phase Transition of LaCrO₃ *Solid State Commun.* 108:691 - 694
- Hoffmann, J.; Schnittger, S.; Norpoth, J.; Raabe, S.; Kramer, T.; Jooss, C. (2012) Nanocomposite stability in Fe-, Co-, and Mn-based perovskite/spinel systems *Journal of Materials Research* 27(11):1462 - 1470
- Howard, C. J.; Stokes, H. T., (1998) Group-Theoretical Analysis of Octahedral Tilting in Perovskites *Acta Crystallogr. B* 54:782 - 789
- Hsu, H.; Blaha, P.; Cococcioni, M.; Wentzcovitch, R. M., (2011) Spin-state crossover and hyperfine interactions of ferric iron in MgSiO₃ perovskite *Phys. Rev. Lett.* 106:118501
- Hung, M-H.; Rao, M. M. V.; Tsai, D-S., (2007) Microstructures and electrical properties of calcium substituted LaFeO₃ as SOFC cathode *Materials Chemistry and Physics* 101(2-3):297-302
- Javaid, S.; Akhtar, M. J., (2014) Pressure-induced magnetic, structural, and electronic phase transitions in LaFeO₃: A density functional theory (generalized gradient approximation) + U study *Journal of Applied Physics* 116:023704

- Kadir, K.; Sakai, T.; Uehara, I. (2000) Structural investigation and hydrogen storage capacity of LaMg_2Ni_9 and $(\text{La}_{0.65}\text{Ca}_{0.35})(\text{Mg}_{1.32}\text{Ca}_{0.68})\text{Ni}$ of the AB_2C_9 type structure *J. Alloys Compd.* 302:112
- King, R. B. (Ed.) (1994) *Encyclopedia of Inorganic Chemistry*, John Wiley & Sons, Chichester, UK
- Kizaki, H.; Kusakabe, K., (2012) DFT-GGA study of NO adsorption on the LaO (0 0 1) surface of LaFeO_3 *Surface Science* 606:337 - 343
- Kleperis, J.; Wójcik, G.; Czerwinski, A.; Skowronski, J.; Kopczyk, M.; Beltowska-Brzezinska, M. (2001) Electrochemical behaviour of metal hydrides *J. Solid State Electrochem.* 5:229 - 249
- Koehler, W. C.; Wollan, E. O., (1957) Neutron-diffraction study of the magnetic properties of perovskite-like compounds LaBO_3 *J. Phys. Chem. Solids* 2(2):100 - 106
- Kokalj, A., (1999) XCrySDen – a new program for displaying crystalline structures and electron densities *J. Mol. Graphics Modelling* 17:176 - 179
- Kokalj, A.; Causa, M., (2000) Proceedings of High Performance Graphics Systems and Applications European Workshop, Bologna, Italy 51 - 54
- Kubas, G. J., (2001) Metal Dihydrogen and σ -Bond Complexes: Structure, Theory, and Reactivity (1 edition) *Kluwer Academic/Plenum Publishers, New York, NY, Springer* ISBN 0-306-46465-9
- Kubas, G. J., (2007) Dihydrogen complexes as prototypes for the coordination chemistry of saturated molecules *Proceedings of the National Academy of Sciences of the United States of America* 104(17):6901 - 6907
- Kubas, G. J.; Ryan, R. R.; Swanson, B. I.; Vergamini, P. J.; Wasserman, H. J., (1984) Characterization of the first examples of isolable molecular hydrogen complexes, $\text{M}(\text{CO})_3(\text{PR}_3)_2(\text{H}_2)$ (M = molybdenum or tungsten; R = Cy or isopropyl). Evidence for a side-on bonded dihydrogen ligand *J. Am. Chem. Soc.* 106(2):451 - 452
- Lee, J. G., (2012) Computational Materials Science: An Introduction (1st edition) *CRC Press* pp. 77 - 193
- Li, L.; Brodholt, J. P.; Stackhouse, S.; Weidner, D. J.; Alfredsson, M.; Price, G. D.; (2005) Electronic spin state of ferric iron in Al-bearing perovskite in the lower mantle *Geophys. Res. Lett.* 32, L17307
- Linden, D.; Reddy, T. B. (Eds.) (2002) *Handbook of Batteries*, 3rd ed., McGraw-Hill, New York
- Liu, L.; Han, A.; Ye, M.; Zhao, M., (2015) Synthesis and characterization of Al^{3+} doped LaFeO_3 compounds: A novel inorganic pigments with high near-infrared reflectance *Solar Energy Materials & Solar Cells* 132:377 - 384

- Liu, X.; Hu, J.; Cheng, B.; Qin, H.; Zhao, M.; Yang, C., (2009) First-principles study of O₂ adsorption on the LaFeO₃ (0 1 0) surface *Sensors and Actuators B* 139:520 - 526
- Liu, Y. F.; Pan, H. G.; Gao, M. X.; Lei, Y. Q.; Wang, Q. D. (2005) Degradation mechanism of the La-Mg-Ni-based metal hydride electrode LaMgNiMnJ *J. Electrochem. Soc.* 152:A1089
- Marezio, M.; Dernier, P. D., (1971) The bond lengths in LaFeO₃ *Mat. Res. Bull.* 6:23 - 30
- Martinelli, G.; Carotta, M. C.; Ferroni, M.; Sadaoka, Y.; Traversa, E., (1999) Screen-printed perovskite-type thick films as gas sensors for environmental monitoring *Sensor Actuator B-Chem.* 55:99 - 110
- McCash, E. M., (2002) Surface Chemistry *Oxford University Press*
- Mojet, B. L.; Eckert, J.; van Santen, R. A.; Albinati, A.; Lechner, R. E., (2001) Evidence for Chemisorbed Molecular Hydrogen in Fe-ZSM5 from Inelastic Neutron Scattering *J Am Chem Soc* 23:8147 - 8148
- Momirlan, M.; Veziroglu, T. N. (2005) The properties of hydrogen as fuel tomorrow in sustainable energy system for a cleaner planet *Int. J. Hydrogen Energy*, 30(7):795 - 802
- Monkhorst, H. J.; Pack, J. D., (1976) Special points for Brillouin-zone integrations *Physical Review B* 13(12):5188 - 5192
- Mosey, N. J.; Liao, P.; Carter, E. A., (2008) Rotationally Invariant ab initio Evaluation of Coulomb and Exchange Parameters for DFT + U Calculations *J. Chem. Phys.*, 129(1):014103 - 014115
- Mueller, M. W., (1968) Chapter 9-The Rare-Earth Hydrides *Metal Hydrides (1st edition)* edited by William M. Mueller, James P. Blackledge, George G. Libowitz ISBN: 9781483272931 pp. 384 - 440
- Nagarajan, G. S.; Van Zee, J. W. (1998) Characterization of the performance of commercial Ni/MH batteries *J. Power Sources* 70:173 - 180
- Nishihara, H.; Hou, P. X.; Li, L. X.; Ito, M.; Uchiyama, M.; Kaburagi, T.; Ikura, A.; Katamura, J.; Kawarada, T.; Mizuuchi, K.; Kyotani, T. (2009) High-pressure hydrogen storage in zeolite-templated carbon *J. Phys. Chem. C*, 113:3189 - 3196
- Nishihata, Y.; Mizuki, J.; Akao, T.; Tanaka, H.; Uenishi, M.; Kimura, M.; Okamoto, T.; Hamada, N., (2002) Self-regeneration of a Pd-perovskite catalyst for automotive emissions control *Nature* 418:164 - 167
- Ovshinsky, S. R.; Dhar, S. K.; Fetcenko, M. A.; Young, K.; Reichman, B.; Fierro, C.; Koch, J.; Martin, F.; Mays, W.; Sommers, B.; Ouchi, T.; Zallen, A.; Young, R. (2000) 17th International Seminar & Exhibit on Primary and Secondary Batteries, vols. 6 - 9, Ft. Lauderdale, Florida

- Ozin, G. A.; McCaffrey, J. G., (1984) The Photoreversible Oxidative-Addition, Reductive-Elimination Reactions $\text{Fe} + \text{H}_2 \rightleftharpoons \text{FeH}_2$ in Low-Temperature Matrices *J. Phys. Chem.* 88:645 - 648
- Palacin, M. R. (2009) Recent advances in rechargeable battery materials: A chemist's perspective *Chem. Soc. Rev.* 38:2565
- Patnaik, P. (2002) *Handbook of Inorganic Chemicals*, McGraw-Hill, New York, NY, USA
- Perdew, J. P.; Burke, K.; Ernzerhof, M., (1996) Generalized Gradient Approximation Made Simple *Phys. Rev. Lett.* 77:3865 - 3868
- Ritzmann, A. M.; Munoz-Garcia, A. B.; Pavone, M.; Keith, J. A.; Carter, E. A., (2013) Ab Initio DFT+U Analysis of Oxygen Vacancy Formation and Migration in $\text{La}_{1-x}\text{Sr}_x\text{FeO}_{3-\delta}$ ($x = 0, 0.25, 0.50$) *Chem. Mater.* 25:3011 - 3019
- Sakintuna, B.; Lamari-Darkrim, F.; Hirscher, M. (2007) Metal hydride materials for solid hydrogen storage: A review *Int. J. Hydrogen Energy* 32:1121 - 1140
- Samara, G. A. (2003) The relaxational properties of compositionally disordered ABO_3 perovskites *Journal of Physics Condensed Matter* 15(9):R367 - R411
- Sandrock, G.; Yiriim, Y. (ed.), (1995) Hydrogen Energy System *Kluwer Academic Publishers* 135 - 166
- Schlaphach, L. (1988) Hydrogen in Intermetallic Compounds I, *Topic in Applied Physics*, Springer-Verlag, Berlin
- Schlapbach, L.; Züttel, A. (2001) Hydrogen-storage materials for mobile applications *Nature* 414(6861):353 - 358
- Selbach, S. M.; Tolchard, J. R.; Fossdal, A.; Grande, T., (2012) Non-linear thermal evolution of the crystal structure and phase transitions of LaFeO_3 investigated by high temperature X-ray diffraction *Journal of Solid State Chemistry* 196:249 - 254
- Solovyev, I.; Hamada, N.; Terakura, K., (1996) t_{2g} versus all 3d localization in LaMO_3 perovskites ($M = \text{Ti} - \text{Cu}$): First-principles study *Phys. Rev. B* 53:7158
- Stackhouse, S.; Brodholt, J. P.; Price, G. D., (2007) Electronic spin transitions in iron bearing MgSiO_3 perovskite *Earth Planet. Sci. Lett.* 253(1-2):282 - 290
- Thomas, C. E. (Ford Motor Company) (1997) Direct-hydrogen-fueled proton-exchange-membrane fuel cell system for transportation applications - hydrogen vehicle safety report, Tech. Rep., U.S. Department of Energy, Washington, DC, USA, Contract no. DE-AC02-94CE50389
- Thomas, K. M. (2007) Hydrogen adsorption and storage on porous materials, *Catalysis Today* 120:389 - 398

- Tzimas, E.; Filiou, C.; Peteves, S. D.; Vryret, J. B. (2003) Hydrogen storage: state-of-the-art and future perspective, *Technical Report EUR 20995 EN*, European Commission, Joint Research Centre (JRC)
- U. S Department of Energy (2011)
www1.eere.energy.gov/hydrogenandfuelcells/mypp/pdfs/storage.pdf
- Venkaiah, G.; Venkateswara Rao K.; Sessa Sai Kumar, V.; Shilpa Chakra, C. H., (2013) Solution Combustion Synthesis and Characterization of Nano crystalline Lanthanum Ferrite using Glycine as a fuel *International Journal of Materials, Methods and Technologies*, 1(1):01 - 07
- von Helmolt, R.; Eberle, U. (2007) Fuel cell vehicles: status 2007 *Journal of Power Sources*, 165(2):833 – 843
- Wang, L.; Maxisch, T.; Ceder, G. (2006) Oxidation energies of transition metal oxides within the GGA+U framework *Phys. Rev. B* 73: 195107
- Wang, Q.; Deng, G.; Chen, Z.; Chen, Y.; Cheng, N. (2013) Electrochemical hydrogen property improved in nano-structured perovskite oxide LaFeO₃ for Ni/MH battery *Journal of Applied Physics* 113:053305
- Wang, Z. L.; Kang, Z. C., (1998) Functional and Smart Materials – Structural Evolution and Structure Analysis *Plenum Press*, New York
- Watson, R. T.; Zinyowera, M. C.; Moss, R. H.; Dokken, D. J., eds. (1996) Climate Change 1995 - Impacts, Adaptations and Mitigation of Climate Change: Scientific-Technical Analyses *Contribution of Working Group II to the Second Assessment Report of the Intergovernmental Panel on Climate Change* Cambridge: Cambridge University Press
- Weber, R. (1991) Wasserstoff – Wie Aus Ideen Chancen Werden, *IZEAk-tuell, Informationszentrale der Elektrizitätswirtschaft (IZE)*, 2nd edition, Frankfurt, Germany
- Woodward, P. M., (1997) Octahedral Tilting in Perovskites. I. Geometrical Considerations *Acta Crystallogr. Section B*, 53:32 - 43
- Wronski, Z. S. (2001) Materials for rechargeable batteries and clean hydrogen energy sources *Int. Mater. Rev.* 46:1 - 49
- Xu, W.; Naaman, O.; Rozenberg, G.; Pasternak, M.; Taylor, R., (2001) Pressure-induced breakdown of a correlated system: the progressive collapse of the Mott–Hubbard state of RFeO₃. *Phys. Rev. B* 64:094411
- Yang, Z.; Xia, Y.; Mokaya, R. (2007) Enhanced hydrogen storage capacity of high surface area zeolite-like carbon materials *J Am Chem Soc*, 129(6):1673 - 1679
- Zhang, H.; Li, N.; Li, K.; Xue, D. (2007) Structural stability and formability of ABO₃-type perovskite compounds *Acta Crystallographica B: Structural Science* 63(6):812 - 818

Zumerchik, J. Ed., (2001) *Macmillan Encyclopedia of Energy*, Macmillan, New York, NY,
USA

APPENDIX

A. 1 Nature of bond connectivity in LaFeO₃ (0 1 0) surface when hydrogen atoms at a molecular bond distance apart interact at the sites:

- **O17-top end-on:** At this site, O17 is bonds to only La8 and La7 before adsorption.

The key structural changes at the reaction site and surrounding environment are that the La7-O17, La7-Fe3, Fe3-O20, O17-H21 and H21-H22 bonds break after optimization and the H21 attaches to Fe3, and La8-O17H22 bond also forms. The La7-O20 bond subsequently changes direction from the +x to -x after the optimization with a decreased O20-O17 bond length from 3.971 Å to 2.864 Å as shown in Table 4.8. Other bonds such as La8-Fe4, Fe3-O19 and La8-Fe3 break whilst La8-O15, La5-O16 and Fe2-O18 form after optimization.

- **O18-top end-on:** At this site, O18 bonds to only La8 at the terminal position before adsorption.

At the reaction site, Fe4-O19, La8-Fe4, O18-H21 and H21-H22 bonds break and the new product Fe4-H21 forms together with the La8-O18H22 that existed. Fe3-O20 bond breaks and the O20 increases in its x-component from 0.308 Å to 4.661 Å whilst at the same time it bonds to La7. O16 increases in its z-component from 3.054 Å to 4.087 Å but still bonds to La7. Fe1-O14 and La5-Fe1 bonds elongate and break off after optimization.

The O17 atom decreases in z-component from 4.433 Å to 3.124 Å and becomes bonded to Fe1. This Fe1-O17 bond which was originally broken at a distance of 3.387 Å now forms at a distance of 2.037 Å.

- ***O19-top end-on:*** At this site, O19 bonds to Fe3, La8 and Fe4. The Fe4 also bonds to La8 and the La8 bonds to Fe3 before adsorption.

At the reaction site, La8-Fe4, Fe4-O19, La8-O19, La8-Fe3, Fe3-O19 and H21-H22 bonds break and H₂O (H21-O19-H22) is formed at a bond angle of 104.61 ° which is similar to that in H₂O (109.5 °). This H21-O19-H22 bond angle was initially 40.62 °. The H21-H22 bond increased in distance from 0.740 Å to 1.554 Å and, O19-H21 and O19-H22 bond lengths also slightly decreased. No O atom moved/ hopped in an attempt to fill the O19 gap.

- ***O19-Fe3 bridge:*** At this site, O19 bonds to Fe3, Fe4 and La8 whilst Fe3 bonds to O20, La7, O15, O19 and La8. Prior to adsorption, H21 and H22 attach to O19 and Fe3 respectively.

After optimization at the reaction site, La8-Fe4, La8-Fe3, Fe3-O19 and H21-H22 bonds break whilst La8-O15 bond forms leading to the products Fe(μO19H21)La8- and -Fe3H22. Subsequently, La5-Fe1 bond breaks whilst La5-O16 bond forms. La-Fe bonds are broken at the topmost layer whilst La-O bonds are formed beneath the topmost layer.

- ***O19-Fe4 bridge:*** At this site, O19 bonds to Fe4, La8 and Fe3 whilst Fe4 bonds to O19 and La8. Prior to adsorption, H21 and H22 attach to O19 and Fe4 respectively.

La8-Fe4, Fe4-O19 and H21-H22 bonds break after optimization at the reaction site and the products Fe4H22 and -La8(μO19H21)Fe3- are formed. In the process, La8-Fe3 and Fe4-O19 bonds break whilst La5-O15 bond forms. The O19-H21 and Fe4-H22 bonds slightly decrease after optimization.

- ***O20-Fe3 bridge:*** At this site, O20 bonds to La7 and Fe3 whilst Fe3 bonds to O20, La7, O19, La8 and O15. Prior to adsorption, H21 and H22 attach to O20 and Fe3 respectively.

After adsorption, La8-Fe3, La7-Fe3, Fe3-O20 and H21-H22 bonds break at the reaction site leading to the products –Fe3H22- and –La7-O20H21. Subsequently, La8-O19 and Fe2-O13 bonds break whilst La5-O14, La6-Fe4 and La5-O15 bonds form. The O20-H21 bond slightly decreases whilst Fe3-H22 bond slightly increases.

A. 2 Nature of bond connectivity in LaFeO₃ (0 1 0) surface when hydrogen atoms at a dihydrogen bond distance apart interact at the sites:

- ***O17-top end-on:*** At this site, O17 bonds to La7 and La8 before adsorption.

After optimization at the reaction site, La7-O17, O17-H21 and H21-H22 bonds break, and the H21 attaches to Fe3 which breaks off from La7, whilst the H22 remains on the La8-O17 bond in the products -La8-O17H22 and –FeH21. Other bonds such as La8-Fe4, Fe3-O19, Fe3-O20, La8-Fe3 and La5-Fe1 break whilst La8-O15, La5-O16 and Fe2-O18 form. O17-H21 bond increases whilst O17-H22 bond decreases.

- ***O18-top end-on:*** At this site, O18 bonds to only La8 before adsorption

After optimization, H21-H22, La8-Fe4 and Fe3-O19 bonds break around the reaction site and the H21 attaches itself to Fe4 to form Fe4H21 and the remaining H22 forms bond with the La8-O18 bond. Other bonds break and form in the process as shown in Table 4.9.

The La7-O20 bond twists (reverses) in direction with the x component of O20 increasing from 0.308 Å to 4.694 Å, and O17 decreases in z component to bond with Fe1.

- ***O19-top end-on:*** At this site, O19 bonds to Fe4, La8 and Fe3 before adsorption.

After optimization, Fe4-O19, La8-Fe4, La8-O19, Fe3-O19, La8-Fe3 and H21-H22 bonds break and the H21-O19-H22 leaves the surface in the form of H₂O to create a hole. No O atom hops to fill in the created gap. The H21-O19-H22 bond angle in the formed H₂O is 106.76 ° but was 43.18 ° initially. The O19 increases in height (z component) from its initial position of 4.853 Å to 6.051 Å. O19-H21 and O19-H22 bonds decrease slightly after optimization.

- ***O19-Fe3 bridg:*** At this site, O19 bonds to Fe3, La8 and Fe4 whilst Fe3 bonds to O20, La7, O15, La8 and O19. Prior to adsorption, H21 attaches to O19 whilst H22 attaches to Fe3.

After adsorption, La8-Fe4, La8-Fe3, Fe3-O19 and H21-H22 bonds break leading to the products Fe4-(μO19H21)La8- and Fe3H22. La8-O15 and La5-O16 bonds form in the process. O19-H21 and Fe3-H22 bonds slightly decrease after optimization.

- ***O19-Fe4 bridge:*** At this site, O19 bonds to Fe4, La8 and Fe3 whilst Fe4 bonds to La8 and O19. Prior to adsorption, H21 attaches to O19 whilst H22 attaches to Fe4 in a bridged configuration.

After adsorption, La8-Fe4, Fe4-O19, La8-Fe3 and H21-H22 bonds break, and the H21 remains on the O19 whilst H22 remains on Fe4. The O19-H21 bond bridges La8

and Fe3 to form $-\text{La8}(\mu\text{O19H21})\text{Fe3}-$. In the process, La7-O20 bond breaks and La5-O15 forms. The O19-H21 and Fe4-H22 bonds decrease slightly after optimization.

- **O20-Fe3 bridge:** At this site, O20 bonds to Fe3 and La7, whilst Fe3 bonds to O19, La8, La7, O20 and O15. Prior to adsorption, H21 attaches to O20 whilst H22 attaches to Fe3 in a bridged configuration.

After adsorption, H21-H22, Fe3-O20, La7-Fe3 and La8-Fe3 bonds break to form the products $-\text{Fe3H22}$ and $-\text{La7-O20H21}$ around the reaction site. In the process, bonds like La6-Fe4, La5-O15 and La5-O14 are formed whilst Fe2-O13 and La8-O19 are broken.

A. 3 Nature of bond connectivity in LaFeO_3 (0 1 0) surface when hydrogen atoms at a dihydride bond distance apart interact at the sites:

- **O17-top end-on:** At this site, O17 bonds to La7 and La8 before adsorption.

At the reaction site, La7-O17 and La8-O17 bonds break and H21-O17-H22 leaves the surface to create a hole in the form of H_2O with an H-O-H bond angle of 105.72° . This angle was initially 110.26° in H21-O17-H22.

In the process, Fe3-O20 and La7-Fe3 bonds break and the O20 which was initially 0.308 \AA in the x direction reverses (increase to 4.772 \AA) in an attempt to fill the created hole even though it does not bond to the La8. The La5-O10 bond also breaks and the O10 now goes to bridge Fe2 and La6. Fe1-O13 bond breaks and Fe1-O15, La8-O15, La6-O10, Fe2-O10 and La5-O14 bonds form.

- **O18-top end-on:** At this site, O18 bonds to only La8 before adsorption.

After adsorption, La8-O18 and O18-H21 bonds break at the reaction site and the H21 detaches from the surface atoms. O18-H22 bond attaches to Fe4 to form -Fe4-O18H22.

In the process, La8-Fe4, Fe3-O20, La8-O19, La8-Fe3, La7-Fe3, La7-O20 and Fe2-O13 bonds break whilst La8-O15, Fe4-O18, La5-O14, Fe2-O16, La8-O16 and Fe4-O16 bonds form. The La8-Fe4 bond which breaks is what leaves H21 detached from the surface as the atomic coordinates of H21 remain essentially the same.

The La7-O20 bond reverses direction from 0.308 Å to 5.322 Å in the x-direction and the La7-O16 bond breaks. O16 moves all the way from its position in the y-direction from 7.661 Å to 0.024 Å, and comes to bond with Fe2, La8 and Fe4. In so doing, the Fe2-O13 bond breaks and La5-O14 bond forms.

- ***O19-top end-on:*** At this site, O19 bonds to La8, Fe3 and Fe4 before adsorption.

After adsorption, all the bond breaking and forming occur at the reaction site. The Fe4-O19, La8-O19 and Fe3-O19 bonds break and H21-O19-H22 leave the surface in the form of H₂O with an H-O-H bond angle of 103.84 ° (initially 97.16 ° for H21-O19-H22). The z axis of O19 increases from 4.853 Å to 5.989 Å in the process. Here, there is no hopping/relocation of O atom in an attempt to fill in the gap.

- ***O20-top end-on:*** At this site, O20 bonds to Fe3 and La7 before adsorption.

After optimization, the Fe3-O20 and La7-O20 bonds break and H21-O20-H22 leaves the surface in the form of H₂O with a bond angle of 106.34 °, an angle which was initially 96.67 ° in H21-O20-H22. There is no hopping of O atom into filling the

created hole. The O20 stays essentially at the same position only with an increase in x direction (0.308 Å to 0.930 Å).

In the process, La8-Fe4, La8-Fe3, La7-Fe3, La6-Fe2, La6-Fe1 and La5-Fe1 bonds break whilst La5-O15 and La5-O16 bonds form.

- **La8-Fe4 bridge:** At this site, Fe4 bonds to La8 and O19 whilst La8 bonds to Fe4, O19, Fe3, O18, O17 and O13. Prior to adsorption, H21 attaches to Fe4 whilst H22 attaches to La8 in a bridged configuration.

After adsorption; at the reaction site, La8-Fe4 and Fe4-O19 bonds break and Fe4-H21 bond forms. The La8-H22 bond also breaks and the H22 now bonds to O19. La8-Fe3 bond also breaks and the O19-H22 bond bridges La8 and Fe3 in the product – La8(μ O19H22)Fe3-.

In the course of the above, La7-O17, Fe3-O20, La7-Fe3, La6-Fe1, La5-Fe1, Fe1-O14 and La5-O10 bonds break, and La5-O14, Fe1-O17 and La5-O15 bonds form. H21-H22 and La8-H22 bonds increase whilst Fe-H21 bond decreases after optimization.

- **La8-O19 bridge:** At this site, O19 bonds to Fe4, La8 and Fe3 whilst La8 bonds to Fe4, O19, Fe3, O18, O17 and O13. Prior to adsorption, H21 attaches to O19 whilst H22 attaches to La8 in a bridged configuration.

After adsorption; at the reaction site, Fe4-O19, La8-Fe4, La8-Fe3 and La8-H22 bonds break and the H22 forms a bond with Fe4. The O19-H21 then bridges La8 and Fe3 in

the products Fe_4H_{22} and $-\text{La}_8(\mu\text{O}_{19}\text{H}_{21})\text{Fe}_3-$. Other bonds such as $\text{La}_7\text{-O}_{20}$ breaks whilst $\text{La}_5\text{-O}_{15}$ forms. The $\text{H}_{21}\text{-H}_{22}$ and $\text{O}_{19}\text{-H}_{21}$ bonds increase after optimization.

- ***Fe3-O19 bridge:*** At this site, O_{19} bonds to Fe_4 , La_8 and Fe_3 whilst Fe_3 bonds to O_{19} , La_8 , O_{15} , La_7 and O_{20} . Prior to adsorption, H_{21} attaches to O_{19} whilst H_{22} attaches to Fe_3 in a bridged configuration.

After adsorption, $\text{Fe}_3\text{-O}_{19}$ and $\text{La}_8\text{-Fe}_3$ bonds break and the products, $\text{Fe}_4(\mu\text{O}_{19}\text{H}_{21})\text{La}_8-$ and $-\text{Fe}_3\text{H}_{22}$ are formed. $\text{La}_8\text{-Fe}_4$ and $\text{La}_5\text{-Fe}_1$ bonds break in the process, and $\text{La}_8\text{-O}_{15}$, $\text{La}_5\text{-O}_{16}$ bonds form. The $\text{H}_{21}\text{-H}_{22}$ and $\text{O}_{19}\text{-H}_{21}$ bond lengths decrease after optimization whilst $\text{Fe}_3\text{-H}_{22}$ bond length increase.

- ***Fe3-O20 bridge:*** At this site, O_{20} bonds to La_7 and Fe_3 whilst Fe_3 bonds to O_{19} , La_8 , O_{15} , La_7 and O_{20} . Prior to adsorption, H_{21} attaches to O_{20} whilst H_{22} attaches to Fe_3 in a bridged configuration.

After adsorption; at the reaction site, $\text{Fe}_3\text{-O}_{20}$, $\text{La}_8\text{-Fe}_3$ and $\text{La}_7\text{-Fe}_3$ bonds break and the products $-\text{Fe}_3\text{H}_{22}$ and $-\text{La}_7\text{-O}_{20}\text{H}_{21}$ are formed.

In the process, the $\text{H}_{21}\text{-H}_{22}$ bond increases marginally from 1.721 Å to 4.069 Å. $\text{La}_8\text{-O}_{19}$ and $\text{Fe}_2\text{-O}_{13}$ bonds break and $\text{La}_5\text{-O}_{14}$, $\text{La}_6\text{-Fe}_4$ and $\text{La}_5\text{-O}_{15}$ bonds form. The $\text{O}_{20}\text{-H}_{21}$ bond decreases whilst $\text{Fe}_3\text{-H}_{22}$ bond increases after optimization.

- ***Fe4-O19 bridge:*** At this site, O_{19} bonds to Fe_4 , La_8 and Fe_3 whilst Fe_4 bonds to La_8 and O_{19} . Prior to adsorption, H_{21} attaches to O_{19} whilst H_{22} attaches to Fe_4 in a bridged configuration.

After adsorption; at the reaction site, La8-Fe4 and Fe4-O19 bonds break and Fe4H22 forms. La8-Fe3 bond also breaks and the O19H21 bridges La8 and Fe3 in the product $-\text{La8}(\mu\text{O19H21})\text{Fe3}-$. Aside these changes in bonds, La5-O15 bond also forms. O19-H21 bond decreases whilst Fe4-H22 bond increases after optimization.